A combined observational and theoretical study of gravitationally lensed quasars

Timo Anguita

Astronomisches Rechen-Institut
Zentrum für Astronomie der Universität Heidelberg

Heidelberg 2009

Dissertation

submitted to the
Combined Faculties for the Natural Sciences and for Mathematics
of the Ruperto-Carola University of Heidelberg, Germany
for the degree of
Doctor of Natural Sciences

presented by

Timo Anguita
Born in Santiago, Chile

Oral examination: April 15^{th} 2009

A combined observational and theoretical study of gravitationally lensed quasars

Referees: Prof. Dr. Joachim Wambsganss
Prof. Dr. Stefan Wagner

Abstract.
In this thesis we study gravitational lensing of quasars, from strong lensing to microlensing. We investigate one strong lens candidate recently discovered in the COSMOS field: COSMOS 5921+0638. Our analysis of the nature of the lens reveals that the system is composed of an early type foreground galaxy at redshift z_l=0.551±0.001 lensing a background low luminosity AGN and its host galaxy at a candidate redshift of z_s=3.14±0.05. We show that flux anomalies observed in the lensed images are likely due to substructure or microlensing by stars in the lensing galaxy. Extending the analysis of the optical emission of lensed quasars, we have used integral field spectroscopy to study four gravitationally lensed quasar systems: HE 0230-2130, RX J0911+0551, H 1413+117 and B 1359+154, as well as objects in their line-of-sight. The first three systems show anomalous flux ratios consistent with microlensing by stars in their lensing galaxies. In the final part of this work, we probe the structure of the accretion disk of the lensed quasar Q 2237+0305 by the analysis of a high magnification microlensing event seen in the so-called "image C" of the system in the year 1999. Using multi-band observations and microlensing simulations, we measure an accretion disk size of Gaussian width $\sigma_{g'}=4.6^{+3.4}_{-3.4} \times 10^{15}\sqrt{M/0.1M_\odot}$ cm and a ratio $\sigma_{r'}/\sigma_{g'}=1.3^{+0.5}_{-0.2}$, without the use of any prior, and of Gaussian width $\sigma_{g'}=1.3^{+0.2}_{-0.7} \times 10^{15}\sqrt{M/0.1M_\odot}$ cm and a ratio $\sigma_{r'}/\sigma_{g'}=1.5^{+0.9}_{-0.3}$ with a prior on the relative velocity between source and microlenses. Both results are in agreement with the predictions of a standard Shakura-Sunyaev disk model. The use of multi-band observations revealed that the magnification event seen in image C of Q 2237+0305 was produced by a caustic crossing with a confidence greater than 74%.

Zusammenfassung.
Die vorliegende Arbeit beschäftigt sich mit durch den Gravitationslinseneffekt abgebildeten Quasaren, vom starken Linseneffekt bis zum Mikrolinseneffekt. Die Analyse des kürzlich im COSMOS-Feld entdeckten Linsenkandidaten COSMOS 5921+0638 zeigt, dass es sich hierbei um eine Vordergrundgalaxie frühen Typs bei einer Rotverschiebung von z_l=0.551±0.001 handelt, welche als Linse auf einen leuchtschwachen AGN bei einer Rotverschiebung von z_s=3.14±0.05 und dessen Muttergalaxie wirkt. Die beobachteten Flussanomalien der gelinsten Bilder werden wahrscheinlich durch Substrukturen oder durch als Mikrolinsen wirkende Sterne in der Vordergrundgalaxie verursacht. Wir benutzen Integrale-Feld-Spektroskopie, um die vier gravitationsgelinsten Quasare HE 0230-2130, RX J0911+0551, H 1413+117, B 1359+154 sowie Objekte entlang der Sichtlinie zu untersuchen. Dabei zeigen die ersten drei Systeme Anomalien in den Flussverhältnissen zwischen den Bildern, welche konsistent mit dem Mikrolinseneffekt aufgrund von Sternen in den Linsengalaxien sind. Im letzten Teil dieser Arbeit erforschen wir das im Jahre 1999 beobachtete Mikrolinsenereignis im sogenannten „Bild C" des gravitationsgelinsten Quasars Q 2237+0305, um die Struktur seiner Akkretionsscheibe zu bestimmen. Mit Beobachtungen in mehreren Filtern und Mikrolinsensimulationen des Systems messen wir eine Gaußbreite von $\sigma_{g'}=4.6^{+3.4}_{-3.4} \times 10^{15}\sqrt{M/0.1M_\odot}$ cm und ein Verhältnis von $\sigma_{r'}/\sigma_{g'}=1.3^{+0.5}_{-0.2}$ ohne die Verwendung irgendeiner A-priori-Annahme bzw. $\sigma_{g'}=1.3^{+0.2}_{-0.7} \times 10^{15}\sqrt{M/0.1M_\odot}$ cm und $\sigma_{r'}/\sigma_{g'}=1.5^{+0.9}_{-0.3}$ mit einer A-priori-Annahme der Relativgeschwindigkeit zwischen Quelle und Mikrolinsen. Beide Ergebnisse sind in Übereinstimmung mit Vorhersagen des Shakura-Sunyaev-Scheibenmodells. Weitere Einschränkungen durch Mehr-Filter-Aufnahmen ergeben, dass das beobachtete Mikrolinsenereignis mit mehr als 74% Wahrscheinlichkeit durch einen Kaustikübergang erzeugt wurde.

para mis padres y Paola

Contents

Acronyms used in this work

2dF	Two Degree Field
2QZ	2dF QSO Survey
ACS	Advanced Camera for Surveys
AGN	Active Galactic Nuclei
APO	Apache Point Observatory
BAL	Broad Absorption Line
BH	Black Hole
BLR	Broad Line Region
CASTLES	CfA-Arizona Space Telescope LEns Survey
CFHT	Canada France Hawaii Telescope
CLASS	Cosmic Lens All-Sky Survey
CMB	Cosmic Microwave Background
COSMOS	Cosmic Evolution Survey
DOF	Degrees Of Freedom
EMS	Electro-Magnetic Spectrum
EROS	Expérience pour la Recherche d'Objets Sombres
ESA	European Space Agency
ESO	European Organisation for Astronomical Research in the Southern Hemisphere
FWHM	Full Width at Half Maximum
FORS	FOcal Reducer and low dispersion Spectrograph (ESO-VLT)
GEMS	Galaxy Evolution from Morphology and SEDs
HST	Hubble Space Telescope
HUDF	Hubble Ultra Deep Field
IFU	Integral Field Unit (ESO-VLT)
ISAAC	Infrared Spectrometer And Array Camera
JPL	Jet Propulsion Lab
LINER	Low-Ionization Nuclear Emission Line Region
LLAGN	Low Luminosity AGN
MACHO	MAssive Compact Halo Object
MCMC	Markov Chain Monte Carlo
ML	Maximum Likelihood
MOS	Multi Object Spectro(graph/scopy)
NASA	National Aeronautics and Space Administration
NLR	Narrow Line Region

OGLE	Optical Gravitational Lensing Experiment
PSF	Point Spread Function
QLF	Quasar Luminosity Function
QSO	Quasi Stellar Object
RASS	ROSAT All Sky Survey
ROSAT	ROentgen SATellite
RMS	Root Mean Square
SDSS	Sloan Digital Sky Survey
SED	Spectral Energy Distribution
SIE	Singular Isothermal Ellipsoid
SIS	Singular Isothermal Sphere
SL2S	Strong Lensing Legacy Survey
SPIcam	Seaver Prototype Imaging camera
VIMOS	VIsible Multi Object Spectrograph
VIPGI	Vimos Interactive Pipeline Graphical Interface
VLT	Very Large Telescope (ESO)
WFPC2	Wide Field Planetary Camera II

1 Introduction

The first documented notion of light being affected by objects in its path was by Sir Issac Newton. In 1704, Issac Newton published his second major book on physical sciences (after *Principia*), *Opticks*. This book included different experiments observed by Newton regarding light and light related phenomena. In the first of his "queries"[1], Newton states: "Do not Bodies act upon Light at a distance, and by their action bend its Rays; and is not this action (*cæteris paribus*) strongest at the least distance?" (Newton 1704). In 1801, Johann Soldner, German mathematician and astronomer, explored light deflection by massive bodies with a Newtonian physics background. He derived that the Sun would produce a deflection of 0.84 arcseconds to a background star in its limb. Einstein in 1911, still without a complete formulation of general relativity and not knowing about Soldner's work, obtained the same result. However, this result was not correct. In 1915, after the formulation of the theory of general relativity, Einstein realized that this value was too small by a factor of 2, as he found that the deflection should be of 1.68 arcseconds.

Einstein encouraged astronomers to measure this deflection as a test of his theory of general relativity. In 1919, Arthur Eddington confirmed Einstein's calculations during a solar eclipse by measuring a deflection of 1.6 arcseconds of the light from a background star during the event. Based on the fact that stars can deflect the light from other stars, Einstein already considered the possibility of strong distortions that would create multiple images (strong lensing). In 1937, Fritz Zwicky extended these ideas and was the first to consider extragalactic objects as source and deflector: this would not only provide larger scale tests for general relativity, but would also allow to measure the masses of bodies exerting the deflection. More than 40 years later, in 1979, the first gravitational lens was discovered using the 2.1m telescope at the Kitt Peak National Observatory in Arizona, USA (Walsh et al. 1979). This was the doubly lensed quasar Q 0957+561.

Interestingly, that same year, Chang & Refsdal (1979) suggested that individual stars in lensing galaxies could affect the brightness of lensed quasar images, now commonly described as microlensing. During the 80s, Paczynski, Kayser and Refsdal, explored this possibility with different simulations, until Irwin et al. (1989) showed the first observational evidence

[1] In the book "Opticks", Newton formulates his hypothesis in question form.

for quasar microlensing. They interpreted a brightness variation in one of the multiple images of Q 2237+0305 as a result of this phenomenon. Until now, hundreds of gravitationally lensed quasars have been observed and many of them show evidence for microlensing activity.

The combination of the physically small region producing the emission in quasars, their high luminosity and their presence in the high redshift universe, makes them ideal candidates for gravitational lensing. Strong quasar lensing allows to probe the cosmological scales of the universe, providing a window into the properties of lensing galaxies and the line-of-sight potential. On the other hand, the increased resolution power of quasar microlensing allows to probe the inner structure of the high redshift source quasars. These reasons have motivated the work presented in this thesis, where we show some of the different studies that can be done using observations of gravitationally lensed quasars coupled with theoretical concepts.

In the next chapter, we review the phenomenological and theoretical background required to perform the studies presented in this dissertation. We introduce the main light source of our study: the quasars. The current knowledge about these objects, their optical properties and their emission, are briefly summarized. We present some of the cosmological concepts, such as distance measures, which are a fundamental requirement for the the work described thereafter. Finally, we review the gravitational lensing phenomenon. Besides describing the rigorous mathematical formalism, we give a description of the different lensing regimes, the observation of gravitational lensing and its analysis techniques. Towards the third chapter we venture into "observational territory", where some of the concepts explained in the former chapter are tested against a candidate strongly lensed system. In the fourth chapter, we analyze the emission of four gravitationally lensed quasars using advanced spectroscopic techniques. This analysis includes: the absorption in the line-of-sight to the system, the intrinsic emission of the quasars and flux anomalies observed in the lensed images. In the fifth chapter, we show how the use of strong gravitational lensing and extragalactic microlensing provides a tool to study the "small" central regions of a high redshift quasar. Using the power of microlensing, we measure the size of the accretion disk around the massive central black hole. The final chapter shows a recapitulation of the work presented in this manuscript as well as a scientific outlook.

2

Phenomenological and Theoretical Background

The main light sources that have been the observational targets for our studies are quasars. Quasars have high luminosities and an increased abundance in the early universe. These properties, coupled with their physical structure, make them ideal candidates to be affected by gravitational lensing. In this chapter, we summarize the current knowledge about these objects and their structure. We also describe some of the fundamental cosmological concepts that are used throughout this manuscript, in particular, those concepts that allow us to define the different distance and time measurements; fundamental requirements to describe the gravitational lensing phenomenon. Finally, we present a review of gravitational lensing: its theoretical formulations and an overview of the different regimes, their properties and uses as tools to probe for underlying astronomical topics.

2.1 Quasars

As shown in the rest of this dissertation, we have used the optical emission of quasars in combination with gravitational lensing to understand properties of objects in the line-of-sight to them as well as the internal properties of quasars themselves. For this reason, in this section we briefly describe their detection history, their nature and their emission.

2.1.1 Quasars through history

Quasars were already observed during the first half of the twentieth century in the radio regime, without much understanding of what kind of objects they were. During the late 50s, radio observations revealed that they had very small angular sizes and were thus considered "star-like" sources. For this reason, these objects were referred to as "quasi stellar radio sources", which was later contracted to "quasars" by Chiu (1964). During the 1960s, the optical counterparts of some of these radio emissions were observed. In particular, spectroscopic analyzes revealed that they were at high redshift (z$\sim$0.1), until that time, the most distant objects ever detected (Schmidt 1963). Later on, many more of these sources were

observed throughout the whole electromagnetic spectrum, and it was realized that only about 10 percent of them show strong radio emission. As a result the "radio" part of the name was eliminated, coining a new name: "Quasi Stellar Object" or QSO. Currently, both names (quasar and QSO) are often used indifferently.

2.1.2 What and where are the quasars?

Quasars are the brightest continuous light sources in the universe. They emit between 10 to 100,000 times more energy than the Milky Way or more than a trillion (10^{12}) times the energy of the Sun, making them visible up to very high redshifts. Quasars show intrinsic brightness variations on time scales of months, weeks and even within a day (Gaskell et al. 1987; Wagner et al. 1990). Variability in such short time scales implies that the emission must originate from a region smaller than the distance covered by a light ray in that particular time lapse (i.e., sizes of light-months, light-weeks and light-days, respectively). Such high luminosities originating from a small region, can only be explained by a violent and unusual phenomenon. The dominant interpretation for the nature of these objects is that they are galaxies with Active Galactic Nuclei (AGN): massive central black holes (BH) in distant galaxies accreting matter around them at very high rates (Rees 1984). Such a process can produce the high luminosities observed.

The number of known quasars has increased significantly in the last decade due to large field surveys, allowing in depth statistical studies of density, luminosity and emission properties. Figure 2.1 shows the integrated quasar i-band luminosity function up to M_i(z=2)=-27.6 (extracted from Richards et al. 2006). From this luminosity function we can see that there is a clear peak in the number of quasars at redshift ∼2.4, this implies that they were much more common when the universe had ∼20% of its current age. The exact reason for this distribution is still under speculation. A common interpretation is that a quasar is a stage in the lifetime of a galaxy, in which there is massive accretion into the central black hole. It is suggested that the higher density of galaxies in the early universe, which leads to higher probability of galaxy interactions, is responsible for igniting the accretion in the galactic nuclei (Webster & Hewett 1990). Theoretical models state that accretion becomes more inefficient as the mass of the black hole increases, which makes quasars finally "turn off" (Boyle et al. 1987), thus, explaining the lack of quasars now. Within this interpretation, the Milky Way's central black hole could well have had active accretion at an earlier epoch. However, even though we know that a massive black hole is present in the center of our galaxy (Melia & Falcke 2001), there is no diagnostic mechanism regarding its accretion history. The cut-off towards higher redshifts seen in Figure 2.1, is usually explained by selection effects and dust extinction. It is important to remark that these explanations are widely discussed and not unique.

2.1.3 Active Galactic Nuclei emission

AGNs can emit in the whole electromagnetic spectrum (EMS). Their optical spectrum is characterized by a continuum that can be described by two power-laws (e.g., Vanden Berk et al. 2001), very broad emission lines (σ∼4000 km/s) and narrow emission lines (σ∼400 km/s). Based on their luminosity, prominent spectral features and temporal variation, AGNs have received different classifications, such as: LINERS (weak nuclear emission lines), Seyferts (low luminosity AGNs; type 1 and type 2 depending on the narrow and broad line emission) and blazars (OVV; BL Lac; fast variations, no optical emission lines) to name a few. Since a

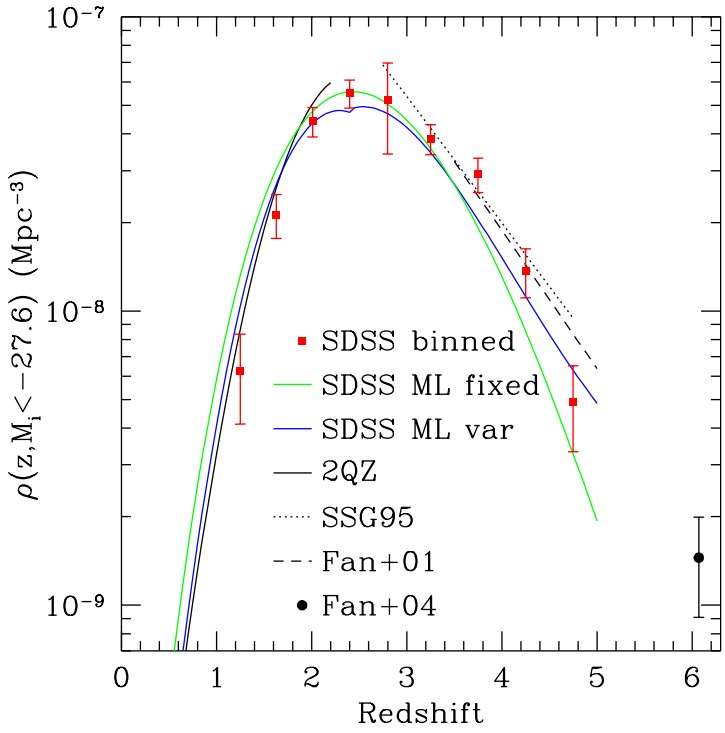

Figure 2.1: *Integrated quasar i-band luminosity function to $M_i(z=2)$=-27.6. The solid black line is from 2QZ. The squares are from the binned SDSS DR3 Quasar Luminosity Function (QLF). The green and blue lines are from the fixed slope and variable high-redshift slope ML (maximum likelihood) parametrization of the SDSS DR3 QLF, respectively. The dashed and dotted lines are from Fan et al. (2001; Fan+01) and Schmidt et al. (1995; SSG95). The z∼6 point from Fan et al. (2004; Fan+04), is shown by the circle. Figure and caption extracted from Richards et al. (2006).*

large enough number of objects have been assigned one of these classifications, a unification theory has been elaborated (Antonucci 1993): All the different descriptions can be due to a single kind of object coupled with a line-of-sight effect. Current AGN models include an obscuring dust torus (Krolik & Lepp 1989) that surrounds it and, as the emission features of AGNs are believed to come from different regions, the blockage of light by this torus can hide certain features depending on the point of view (see Figure 2.2).

The location where the different emission features are generated and the physical sizes of these regions are of particular interest for this work (see Table 2.1 for a summary). The different structural regions in the standard AGN model (which in general scale with the luminosity) are:

- Accretion disk: The accretion disk is formed by rapidly rotating hot material around the massive central black hole. It produces thermal emission responsible for the continuum emission in the optical, UV and soft X-ray range. Variability studies tell us that the estimated size of this accretion disk is of the order of milli-parsecs (limit imposed by the path that light can travel in the variability time scale). Thermal models of the accretion disk state that: the more energetic (blue) emission comes from regions of the accretion disk closer to the central black hole whereas the less energetic (red) emission comes from regions of the accretion disk further away from the black hole (e.g., Shakura & Sunyaev 1973).

- Broad Line Region (BLR): As the name states, this region is responsible for the (permitted and semi-permitted) broad emission lines in the optical spectrum. These emission lines are produced by cold material near the accretion disk. Their broadness is mainly due to the Doppler shift produced by the high rotation speed of this material around the black hole. Not much is known about the geometry and kinematics of the Broad Line Region, but it is subject of current study (e.g., Laor 2004). The most accurate measure of its size comes from reverberation mapping (e.g., Peterson et al. 2004), which tells us that this region is a couple of orders of magnitude larger than the accretion disk.

- Dusty "Torus": According to the standard AGN model, the accretion disk is surrounded by a hot and warm dust torus. This torus is heated by photons coming from the continuum emitting region and are then re-emitted. This is observed as thermal infrared emission. As mentioned before, the dust torus has a key role in unification theories.

- Narrow Line Region (NLR): The emission lines produced by this region come from a much larger (1 to 1000 pc) region of the quasar. This makes the cold material to rotate at considerably lower speeds making the emission lines narrower. These emission lines can be permitted or forbidden.

- Jet: Jets are highly collimated outflows coming from a region close to the disc. It is observed as synchrotron emission due to charged particles which, at the time being, are not known. They emit in the whole electromagnetic spectrum, but their most evident emission is in the radio regime. These jets can reach sizes orders of magnitude larger than the quasars' host galaxies: up to 1 Mpc.

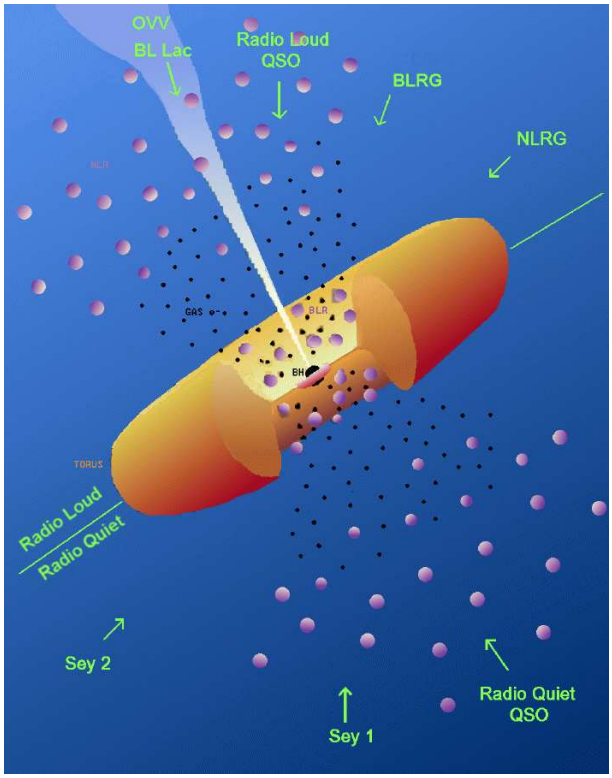

Figure 2.2: *Depiction of an AGN. The continuum emitting region is produced on the accretion disk around the central black hole, and the broad and narrow line emission regions from clouds around this disk. Different perspectives result in different prominent features. Courtesy of BeepoSAX calendar (http://www.asdc.asi.it/bepposax/calendar/).*

Table 2.1: *Prominent Emission Components of an AGN.*

Region	Size	EM emission
Accretion Disk	$\sim 5 \times 10^{-3}$ pc	Thermal: Optical, UV, Soft X-ray
Broad Line Region (BLR)	0.01...0.1 pc	Broad emission lines (permitted & semi-permitted)
Inner Radio Jet	$\sim$1 pc	Radio
Nuclear Dust "Torus"	1...10 pc	Thermal IR
Narrow Line Region (NLR)	1...1000 pc	Narrow emission lines (forbidden & permitted)
Large-scale Radio Jet	10^3...10^6 pc	Synchrotron: Radio

2.2 Cosmology

As quasars are located at very large distances, we need to understand how space and time behaves between us and them. In this section, we show some of the fundamental cosmological concepts that are used throughout this manuscript. They are an important requirement to describe the gravitational lensing phenomenon discussed in the next section (Section 2.3). The

concepts shown in this section are mostly based upon the work presented by Schneider et al. (1992), Peebles (1994) and Hogg (1999).

2.2.1 The standard cosmological model

The currently accepted cosmological model states that the universe has been expanding since the "Big Bang", about 13.7 billion years ago. The history of the universe since this "starting point" can be briefly summarized as follows: From this initial point in time, a plasma composed of elementary particles appeared. Due to the high temperature of this plasma, particles and anti-particles were constantly being created and annihilated. With the cooling produced by the expansion, it is believed some of them were "frozen out" (dark matter particles decoupled from the plasma due to the drop in temperature). Further cooling merged particles in the plasma, forming larger particles, until baryonic matter was composed by Hydrogen, Helium and Lithium nuclei, and free electrons. These nuclei and free electrons formed atoms, eliminating the possibility of Compton scattering of photons in the plasma. The free photons escaped as the light we see redshifted in the Cosmic Microwave Background (CMB). At this point, the universe became neutral and entered a period of time called "the Dark Ages": no photon-emission process existed. Self gravity between the baryonic atoms and the pre-existing dark matter halos, produced a merging of them into larger structures. Eventually, the first stars and galaxies were formed, re-ionizing the universe and rendering it bright as it is now.

With the large amount of matter (baryonic and dark) in the universe, one would expect the initial expansion to stop, or at least to slow down. However, studies of the light from distant supernovae, have shown that the expansion of the universe is actually accelerating (Knop et al. 2003). This fact reveals that there is an unknown energy, which opposes gravity, responsible for driving this acceleration; this force is currently denominated Dark Energy. Dark Energy makes up for about ∼70% of the composition of the current universe, whereas dark and baryonic matter constitute the remaining ∼30% (∼25% and ∼5%, respectively).

The cosmological principle states that on a sufficiently large scale, the universe is homogeneous and isotropic. It implies that a mathematical description of space-time or a simple metric exists. This is the Robertson-Walker metric (1933), created by two mathematicians with the same names. It has the explicit form:

$$ds^2 = c^2dt^2 - R^2(t)\left(\frac{dr^2}{1-kr^2} + r^2(d\theta^2 + sin^2\theta d\phi^2)\right) \tag{2.1}$$

where ds is the line element, $[t, r, \theta, \phi]$ are the co-moving coordinates of an object, k is the curvature of the universe, $R(t)$ is a cosmological scale factor and c is the speed of light. Negative curvature k values describe a closed universe, while positive k values describe an open universe. The critical value k=0 denotes a flat euclidean universe. The cosmological scale parameter $R(t)$ describes how the spatial (r, θ, ϕ) part of the universe expands or contracts.

If we consider a light ray which travels in null geodesics (i.e., ds=0) and we take a radial path (motivated by the radial expansion of the universe), Equation 2.1 turns to:

$$\frac{c\ dt}{R(t)} = \frac{dr}{\sqrt{1-kr^2}}. \tag{2.2}$$

Integrating the first part of Equation 2.2 between an emission time t_e and an observed

time t_o and equating to the same integral between t_e+δt_e and t_o+δt_o we obtain:

$$\int_{t_e}^{t_o} \frac{dt}{R(t)} = \int_{t_e+\delta t_e}^{t_o+\delta t_o} \frac{dt}{R(t)}. \tag{2.3}$$

Assuming the variation $\delta t \ll R/\dot{R}$ yields:

$$\frac{R(t_o)}{R(t_e)} = \frac{\delta t_o}{\delta t_e} = \frac{\nu_e}{\nu_o} \tag{2.4}$$

where we replaced $1/\delta t$ by the frequency ν. If we replace ν by the wavelength λ=c/ν we obtain:

$$\frac{R(t_o)}{R(t_e)} = \frac{\lambda_o}{\lambda_e} = 1 + z \tag{2.5}$$

that directly relates the scale factor $R(t)$ with the cosmological redshift z.

The temporal (cosmological time) derivative of the cosmological scale parameter $R(t)$ divided by itself, gives a measure of the expansion rate. It is called the Hubble parameter:

$$H(t) = \frac{\dot{R}(t)}{R(t)} \tag{2.6}$$

which has units of [time^{-1}]. It reflects how fast the universe is expanding at a certain time towards the beginning of the expansion, compared to how much it expanded until then. For the present cosmological time (z=0), this parameter is called the Hubble constant H_0 and it is generally expressed in units of $km\ s^{-1}\ Mpc^{-1}$. The inversion of the Hubble constant (i.e., $1/H_0$) is an expression for the age of the universe, known as the Hubble time.

Einstein's general theory of relativity uses 10 field equations to describe gravitational force through descriptions of the curvature of space-time caused by matter and energy. They have the form:

$$R_{\mu\nu} - \frac{1}{2} g_{\mu\nu} R + \Lambda g_{\mu\nu} = \frac{8\pi G}{c^4} T_{\mu\nu}. \tag{2.7}$$

where the field curvature (composed by the Ricci tensor: $R_{\mu\nu}$, and Ricci curvature: R=$R_{\mu\nu}R^{\mu\nu}$) is related to the flux and density of energy and momentum (stress-energy tensor: $T_{\mu\nu}$). $g_{\mu\nu}$ is the metric and Λ is the cosmological constant.

By inserting the Robertson-Walker metric (Equation 2.1) into Einstein's fields equations a set of solutions is obtained. These solutions are known as the Friedmann-Lemaître equations that have the form:

$$\left(\frac{\dot{R}}{R}\right)^2 = \frac{\Lambda c^2}{3} - \frac{kc^2}{R^2} + \frac{8\pi G}{3}\rho \tag{2.8}$$

$$\frac{\ddot{R}}{R} = -\frac{4\pi G}{3}\left(\rho + \frac{3p}{c^2}\right) + \frac{\Lambda c^2}{3}. \tag{2.9}$$

These equations of state of the universe, relate pressure (p) and density (ρ) through the scale parameter R(t). Multiplying Equation 2.8 with $(R/\dot{R})^2{=}1/H^2$ and moving to the frame of t=0 we can rewrite:

$$\underbrace{\left(\frac{\Lambda c^2}{3H_0^2}\right)}_{\Omega_\Lambda} + \underbrace{\left(-\frac{kc^2}{R_0^2 H_0^2}\right)}_{\Omega_k} + \underbrace{\left(\frac{8\pi G}{3H_0^2}\rho_0\right)}_{\Omega_M} = 1 \tag{2.10}$$

where we have identified the cosmological constant (Ω_Λ), curvature (Ω_k) and matter (Ω_M) parameters.

The Friedmann-Lemaître equations together with the expression for redshift shown in Equation 2.5, can provide a parametrization of the Hubble parameter $H(t){=}\dot{R}(t)/R(t)$ in terms of the redshift z, with a form: $H(z){=}H_0E(z)$ (Peebles 1994) where:

$$E(z) = \sqrt{\Omega_M(1+z)^3 + \Omega_k(1+z)^2 + \Omega_\Lambda}. \tag{2.11}$$

Using this function we can parametrize, besides the Hubble parameter, the Friedmann-Lemaître equations and the metric as a function of the cosmological redshift z; a directly observable parameter.

2.2.2 Cosmography

Cosmography refers to the different distance measures in cosmology. In the following, aided with some of the definitions shown previously, we describe some of the measurements useful within the framework of gravitational lensing.

Look-back time

Look-back time is defined as the lapse of time between the emission of a photon at redshift z and the current cosmological time ($z{=}0$) as:

$$t_l = \int_0^z \frac{dz}{H(z)(1+z)}. \tag{2.12}$$

It tells us how long it took for the photons to travel from redshift z to redshift $z{=}0$.

Co-moving distance

Co-moving distance (D_C) defines the distance traveled by a radial light ray between a redshift z and the present cosmological time. The fact that it is measured in co-moving coordinates, implies that the distance traveled by the light ray needs to be scaled by the cosmological scale parameter R(t). Eliminating the angular part (θ, ϕ) of the metric (as shown in Equation 2.2) and using the redshift parametrization shown in Equation 2.11 we obtain:

$$D_C(z) = \int_0^t \frac{c\ dt}{R(t)} = \int_0^r \frac{dr}{\sqrt{1-kr^2}} = \int_0^z \frac{c\ dz}{H(z)}. \tag{2.13}$$

This integral has an analytical solution for the special case when $\Omega_\Lambda{=}0$ and $\Omega_M{<}1$ with the form (Peebles 1994):

$$D_C(z) = \frac{2c[2 - \Omega_M(1-z) - (2-\Omega_M)\sqrt{1+\Omega_M z}]}{H_0\Omega_M^2(1+z)}. \tag{2.14}$$

Proper distance

This distance measures the path covered by a light ray between a redshift z and the actual cosmological time. Similarly to the co-moving distance, this is measured for radial rays in null geodesics, with the difference that it is not scaled by the cosmological scale parameter R(t), since it is defined at a constant cosmological time:

$$D_P(z) \int_0^t c\ dt = \int_0^r \frac{R(t)\ dr}{\sqrt{1-kr^2}} = \int_0^z \frac{c\ dz}{H(z)(1+z)} \tag{2.15}$$

Angular diameter distance

This distance is defined as the ratio between the physical size of an object at redshift z and the angular size it displays at the current cosmological time:

$$D_A(z) = \frac{D_C(z)}{1+z} \tag{2.16}$$

where $D_C(z)$ is the co-moving distance (see Equation 2.13). The dividing factor (1+z) present in the angular diameter distance makes it the only cosmological distance that does not grow indefinitely with redshift, but peaks around redshift z≈1 (depending on the choice of cosmological parameters). This means that an identical object at redshift z≈1 would actually display a smaller angular size than, for example, at z≈4 (see Figure 2.3).

Angular diameter distances, deal with the apparent geometry, and thus, are the main cosmological distances used when studying light deflection. As shown in the next section, in gravitational lensing, not only the distance between the current cosmological time (z=0) and a redshift z is required, but also a measure of the angular distance between two objects at arbitrary redshifts z_1 and z_2. This is not simply $D_A(z_2)$-$D_A(z_1)$ but:

$$D_A(z_1, z_2) = \frac{1}{1+z_2}\left(D_C(z_2)\sqrt{1+\Omega_k\frac{D_C^2(z_1)H_0^2}{c^2}} - D_C(z_1)\sqrt{1+\Omega_k\frac{D_C^2(z_2)H_0^2}{c^2}}\right) \tag{2.17}$$

where D_C is the co-moving distance (Equation 2.13). This expression is only valid for $\Omega_k \geq 0$ (Hogg 1999).

Luminosity distance

This distance relates the intrinsic luminosity of an object with its observed flux. It is defined as:

$$D_L = \sqrt{\frac{L}{4\pi F}} \tag{2.18}$$

where L is the bolometric luminosity and F is the observed flux of an object. Luminosity distance thus is used in photometric measurements of high redshift sources, such as absolute magnitude. It is related to the co-moving and angular diameter distances in the following way:

$$D_L = D_C(1+z) = D_A(1+z)^2. \tag{2.19}$$

For a comparison between the different distances see Figure 2.3. All the work presented here-after makes use of this cosmological concepts and distance measures using cosmological parameters fixed to:

- $\Omega_\Lambda = 0.7$
- $\Omega_M = 0.3$
- $\Omega_k = 0.0$
- $H_0 = 70\ km\ s^{-1}\ Mpc^{-1}$

following the concordance model (e.g., Komatsu et al. 2008)

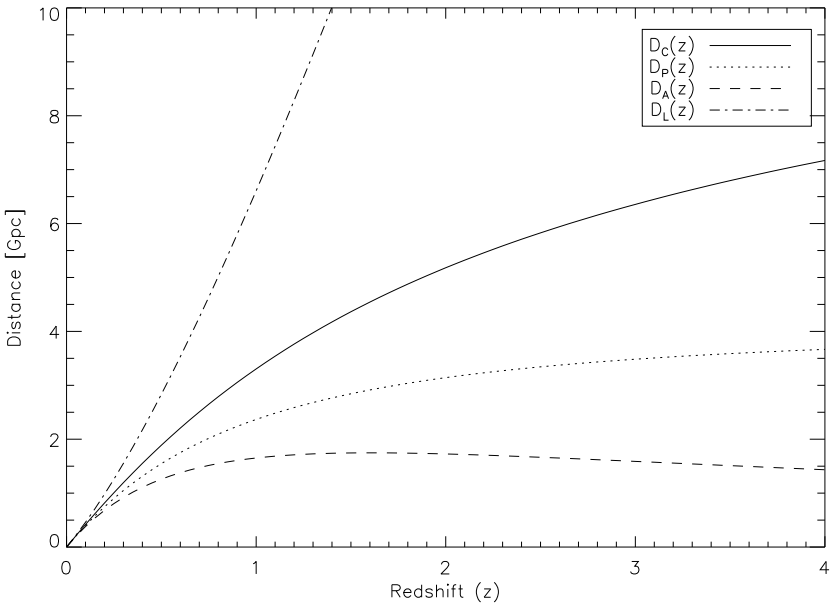

Figure 2.3: *Comparison between the different cosmological distances. All measures shown are formulated using the cosmological parameters displayed in the text.*

2.3 Gravitational lensing

This section is aimed at giving a brief review of the gravitational lensing phenomenon, from the theoretical concepts, to its observations and its uses as an astrophysical tool. Most of the concepts described on this section are based on the work presented in Schneider et al. (1992); Narayan & Bartelmann (1996); Schneider et al. (2006).

2.3.1 Theory

The lens equation

The fundamental equation of gravitational lensing is the lens equation. There are many approaches to derive it. Here, we present a geometrical approach, based on the formulation first shown by Refsdal (1964b).

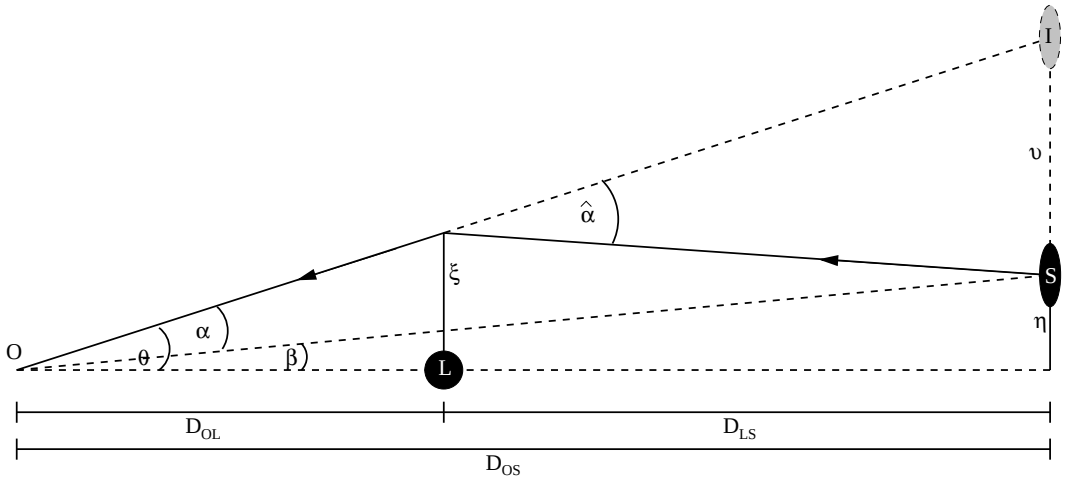

Figure 2.4: *Typical geometric scenario of a gravitational lens. The light emitted from a source (S) is deflected by an angle $\hat{\alpha}$ due to the gravitational potential produced by the massive lens (L) before reaching the observer (O). θ shows the angle between the lens (L) and the "apparent" position of the source (the image I), whereas β is the angle between the lens (L) and the "real" position of source (S). ξ denotes the impact parameter of the light ray with respect to the lens, η is the projected distance between the lens (L) and the source (S) and υ is the projected distance between the source (S) and the image (I). D_{OL}, D_{OS} and D_{LS} are the angular diameter distances (see Equations 2.16 and 2.17) between the observer and the lens, the observer and the source and the lens and the source, respectively.*

In the geometrical scheme shown in Figure 2.4, the assumptions that all the angles involved are very small and the lens is very thin when compared to the line-of-sight distances imply that:

$$\overrightarrow{\theta}\, D_{OS} = \overbrace{\overrightarrow{\beta}\, D_{OS}}^{\overrightarrow{\eta}} + \overbrace{\overrightarrow{\hat{\alpha}}\, D_{LS}}^{\overrightarrow{\upsilon}}. \tag{2.20}$$

Replacing with $\overrightarrow{\theta} = \overrightarrow{\xi}\,/D_{OL}$ we obtain, in terms of the impact parameter $\overrightarrow{\xi}$:

$$\overrightarrow{\eta} = \frac{D_{OS}}{D_{OL}}\overrightarrow{\xi} - D_{LS}\overrightarrow{\hat{\alpha}}(\xi) \tag{2.21}$$

or in terms of the angle $\overrightarrow{\theta}$:

$$\overrightarrow{\beta} = \overrightarrow{\theta} - \frac{D_{LS}}{D_{OS}}\overrightarrow{\hat{\alpha}}(\theta) = \overrightarrow{\theta} - \overrightarrow{\alpha}(\theta) \tag{2.22}$$

where we have used the fact that $D_{OS}\overrightarrow{\alpha}$=$D_{LS}\overrightarrow{\hat{\alpha}}$. Equation 2.22 is the lens equation. It relates the observed positions of a source with its actual position. As this is a non-linear equation, it can have multiple solutions. The amount of solutions possible for each particular case reveals the amount of images of the background source created in the lens plane.

Lens mapping

The lens equation 2.22 can be understood as a mapping from the source plane (angle β) to the image or lens plane (angle α). Thus, for small deflections, and to first order the lens equation (Equation 2.22) can be described by the Jacobian matrix A:

$$A = \frac{\partial \overrightarrow{\beta}}{\partial \overrightarrow{\theta}} = \left(\delta_{ij} - \frac{\partial \alpha_i(\overrightarrow{\theta})}{\partial \theta_j} \right). \tag{2.23}$$

The angle $\overrightarrow{\alpha}$ can be expressed as the gradient of a bi-dimensional scalar potential:

$$\overrightarrow{\alpha} = \overrightarrow{\nabla} \psi \tag{2.24}$$

where:

$$\psi = \frac{D_{LS}}{D_{OL} D_{OS}} \frac{2}{c^2} \int \Phi(\overrightarrow{r}) dz \tag{2.25}$$

is the bi-dimensional deflection potential, which is a function of the Newtonian potential $\Phi(\overrightarrow{r})$ of the lens.

Inputting Equation 2.24 into Equation 2.23 we obtain:

$$A = \begin{pmatrix} 1 - \partial_{xx}\psi & -\partial_{xy}\psi \\ -\partial_{yx}\psi & 1 - \partial_{yy}\psi \end{pmatrix} = \begin{pmatrix} 1 - \kappa - \gamma_1 & -\gamma_2 \\ -\gamma_2 & 1 - \kappa + \gamma_1 \end{pmatrix} \tag{2.26}$$

where we have defined the convergence κ and the shear vector γ=(γ_1, γ_2) as:

$$\kappa = \frac{1}{2}(\partial_{xx}\psi + \partial_{yy}\psi) \tag{2.27}$$

$$\gamma_1 = \frac{1}{2}(\partial_{xx}\psi - \partial_{yy}\psi) \tag{2.28}$$

$$\gamma_2 = \partial_{xy}\psi = \partial_{yx}\psi. \tag{2.29}$$

The Jacobian matrix A (Equation 2.26), can be written also as a rotation matrix:

$$A = (1 - \kappa) \begin{pmatrix} 1 & 0 \\ 0 & 1 \end{pmatrix} - \gamma \begin{pmatrix} cos(2\varphi) & sin(2\varphi) \\ sin(2\varphi) & -cos(2\varphi) \end{pmatrix}. \tag{2.30}$$

With this form, we can see that the convergence κ accounts for the isotropic deformation of the source from the source plane to the lens plane, whereas the shear γ accounts for the tidal (anisotropic) deformations. An example of this effect is shown in Figure 2.5: if the source is circular, when mapping it via a lensing potential, κ is responsible for enlarging it, keeping its shape, and γ is responsible for introducing an ellipticity.

The convergence κ can also be defined as:

$$\kappa(\overrightarrow{\theta}) = \frac{\Sigma(\overrightarrow{\theta})}{\Sigma_{crit}} \tag{2.31}$$

where $\Sigma(\overrightarrow{\theta})$ is the surface mass density at a given distance from the lens and Σ_{crit} is the lensing critical density, defined as:

$$\Sigma_{crit} = \frac{c^2 D_{OS}}{4\pi G D_{OL} D_{LS}} \tag{2.32}$$

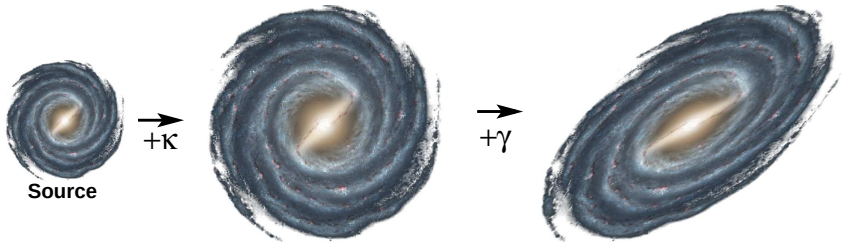

Figure 2.5: *Illustration of the deformation of a circular source. The convergence κ accounts for the isotropic deformation and the shear γ accounts for the tidal deformation of the source galaxy.*

The critical density is the minimum density required to create multiple images, thus, sources located at projected regions with convergence (or scaled surface density) values $\kappa \geq 1$ map into multiple images to the lens plane.

Magnification, critical and caustic lines

Liouville's theorem dictates that a Hamiltonian transformation such as the one induced by lensing (Equation 2.23), conserves surface brightness. Nevertheless, lensing changes the apparent surface area of an object, thus, magnifying the light of a source by the ratio between the surface areas of the lensed and original source. As the Jacobian matrix A contains all the information on the shape distortions, the magnification μ is given by:

$$\mu = \frac{1}{det(A)} = \frac{1}{(1-\kappa-\gamma)(1-\kappa+\gamma)} = \frac{1}{(1-\kappa)^2 - |\gamma|^2}. \tag{2.33}$$

Note that there is a singularity when the determinant of A is zero, which happens when either $(1-\kappa-\gamma)$ or $(1-\kappa+\gamma)$ are equal to zero. These singularities define the tangential and radial critical curves, respectively. They are non-intersecting closed curves (external and internal, respectively) that define the location of maximum (i.e., "infinite") magnification due to the lens potential in the lens plane. When mapped to the source plane, these curves are called "caustic" lines or simply "caustics". Caustics can show more complicated patterns that intersect, but remain closed curves.

Figure 2.6 shows critical (a: lens plane) and caustic (b: source plane) lines for an elliptical gravitational lens. A source at different positions with respect to the caustic lines maps to different image configurations in the lens plane. When the source is inside the area between the two caustic lines (e.g, blue spots in Figure 2.6), two images are mapped to the lens plane: one outside both critical curves and one between them. When the source is enclosed by both caustic curves, four images of the source are mapped (e.g., red spots in Figure 2.6): two outside the critical curves and two between them. If the source lies outside both caustic curves, there is no image splitting (e.g., pink spot in Figure 2.6).

Time-delays

As images from a background source can be located at different impact parameter distances from the lens, the light from each one of them travels different paths. Additionally, at different locations of the potential, space-time becomes stretched/compressed, thus, producing

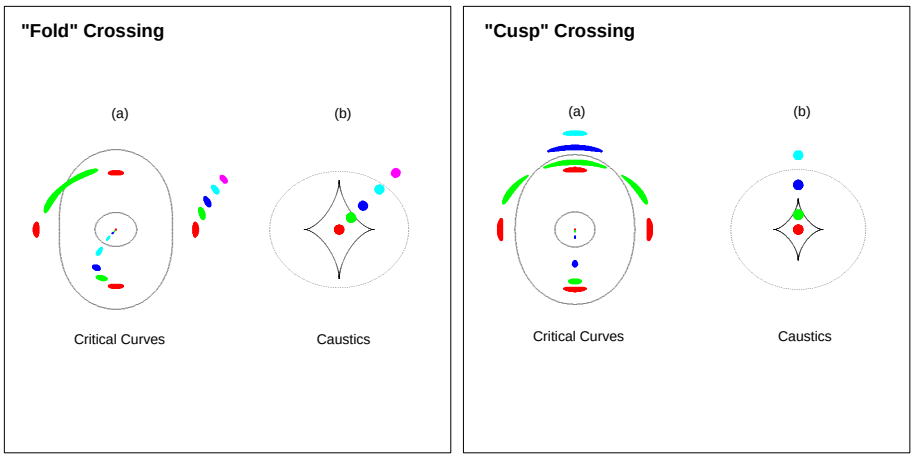

Figure 2.6: *Image (a) and source (b) positions with respect to critical curves (a) and caustics (b) curves. The left panel shows a fold caustic crossing and the right panel a cusp crossing. The colored circles in panels (b) display the different source positions with respect to the caustics. These map to the distorted colored shapes in panels (a) shown with respect to the critical curves. Figure taken from Narayan & Bartelmann (1996).*

retardations in time (Shapiro 1964). This leads to a difference in the arrival time of the light from lensed images emitted at equal times from the source.

From Equations 2.22 and 2.24 we have already seen that the lens equation can be written as:

$$\overrightarrow{\beta} = \overrightarrow{\theta} - \overrightarrow{\alpha}(\theta) = \overrightarrow{\theta} - \overrightarrow{\nabla}\psi. \tag{2.34}$$

Equating to zero and rewriting leads to:

$$\overrightarrow{\nabla}\left(\frac{1}{2}(\overrightarrow{\theta} - \overrightarrow{\beta})^2 - \psi\right) = 0 \tag{2.35}$$

which measures the extrema of the *time-delay surface* that is generally defined by:

$$t(\overrightarrow{\theta}, \overrightarrow{\beta}) = \frac{1+z_l}{c}\frac{D_{OL}D_{OS}}{D_{LS}}\left(\frac{1}{2}\underbrace{(\overrightarrow{\theta} - \overrightarrow{\beta})^2}_{Geometrical} \overbrace{-\psi}^{Gravitational}\right) \tag{2.36}$$

where we have identified the terms responsible for the geometrical (path difference) and gravitational (Shapiro-delay) time-delays. The difference in arrival times between lensed images is thus the subtraction of the arrival time values at the positions of each image in the time-delay surface.

As the trace of the time-delay surface (Equation 2.36) is proportional to the Jacobian matrix A, the extrema of this surface (Equation 2.35) measure the location of the multiple images. The extrema can be: minima, maxima or saddle points. If det(A)>0 and tr(A)>0 the points are minima of the time-delay surface, if det(A)>0 and tr(A)<0 the points are maxima and if det(A)<0 the points are saddle points. When an image is located at a saddle point, it has negative magnification $\mu = det(A)^{-1}$. This means that it has a magnification $|\mu|$ but it is mirror inverted with respect to the source.

2.3.2 Lens potentials

In order to illustrate the previously defined formalism, it is of interest to analyze some of the most used lens potentials. Besides serving as simple examples, the process of analyzing them, yields different parameters widely used in gravitational lensing as intrinsic scales.

The Schwarzschild lens

The case of a spherically symmetric lens whose Schwarzschild radius is much smaller than the impact parameter (i.e., $\frac{2GM}{c^2} \ll \xi$) is called the Schwarzschild lens (or point mass lens).

Spherical symmetry simplifies much of the previous formalism, as the deflection angle $\hat{\alpha}(\xi)$ (where ξ is the impact parameter as shown in Figure 2.4) reduces to:

$$\hat{\alpha}(\xi) = \frac{4GM}{c^2 \xi}. \tag{2.37}$$

Inserting this deflection angle into Equation 2.22 and using $\xi = \theta D_{OL}$ we obtain:

$$\beta(\theta) = \theta - \frac{4GM}{c^2 \theta} \frac{D_{LS}}{D_{OS} D_{OL}}. \tag{2.38}$$

When the angle β vanishes (observer, lens and source perfectly aligned) we obtain a critical angle $\theta = \theta_E$ which is called the Einstein angle (or angular Einstein radius):

$$\theta_E = \sqrt{\frac{4GM}{c^2} \frac{D_{LS}}{D_{OS} D_{OL}}}. \tag{2.39}$$

The ring this angle subtends in the lens plane has a characteristic radius called the lens plane Einstein radius (R_E) with the form:

$$R_E = \theta_E D_{OL} = \sqrt{\frac{4GM}{c^2} \frac{D_{LS} D_{OL}}{D_{OS}}}. \tag{2.40}$$

This characteristic length in the source plane has the form:

$$R_{E_S} = \theta_E D_{OS} = \sqrt{\frac{4GM}{c^2} \frac{D_{LS} D_{OS}}{D_{OL}}}. \tag{2.41}$$

Using the Einstein angle θ_E we can re-write Equation 2.38 as:

$$\theta^2 - \theta \beta(\theta) - \theta_E^2 = 0 \tag{2.42}$$

which has the solution:

$$\theta_\pm = \frac{1}{2} \left(\beta \pm \sqrt{\beta^2 + 4\theta_E^2} \right). \tag{2.43}$$

This solution reveals the positions of two mirrored images of the source as seen by the observer in the lens plane with separations:

$$\theta_+ - \theta_- = \sqrt{\beta^2 + 4\theta_E^2}. \tag{2.44}$$

In the limit where $\beta \gg \theta_E$, there is no deflection as the position of the image coincides with the position of the source. In the limit when $\beta = 0$, we have a single solution θ_E. The source is distorted into a ring around the lens in the image plane.

As in this case we are dealing with a compact spherically symmetric mass distribution, the determinant of the Jacobian matrix A (see Equation 2.23) is simply:

$$det(A) = \frac{\beta}{\theta}\frac{\partial\beta}{\partial\theta}. \tag{2.45}$$

Replacing β in terms of θ and θ_E from Equation 2.42 we obtain:

$$det(A) = 1 - \left(\frac{\theta_E}{\theta}\right)^4 = \mu^{-1} \tag{2.46}$$

which is the inverse magnification of the images. This leads to magnifications:

$$\mu_\pm = \frac{\theta_\pm^4}{(\theta_\pm^2 + \theta_E^2)(\theta_\pm^2 - \theta_E^2)} = \frac{1}{2} \pm \frac{2+u^2}{2u\sqrt{u^2+4}} \tag{2.47}$$

for the two images, where we have introduced the scaled angle $u{=}\theta/\theta_E$. The total magnification is given by:

$$\mu = \mu_+ - \mu_- = \frac{2+u^2}{u\sqrt{u^2+4}}. \tag{2.48}$$

The magnification of the second image is subtracted from the magnification of the first image. Indeed, formally, it has negative magnification due to the fact that it is mirror inverted (negative parity) when compared to the first (positive parity). Being a spherically symmetric potential, the folding of the critical curves to the source plane does not produce diamond caustics (as the ones shown in Figure 2.6).

The Singular Isothermal Sphere (SIS)

The Singular Isothermal Sphere, as the name suggests, is also a spherical potential. However, contrary to the Schwarzschild lens, it does not necessarily imply a compact profile. The SIS has a three dimensional mass density distribution:

$$\rho(r) = \frac{\sigma_v^2}{2\pi G}\frac{1}{r^2} \tag{2.49}$$

where σ_v is the one dimensional velocity dispersion matter in the profile. This density implies a total radial mass of:

$$M_{tot}(R) = \int_0^R 4\pi r'^2 \Sigma(r') = \frac{2\sigma_v^2 r}{G}. \tag{2.50}$$

In lensing, however, we assume that the distances between observer, lens and source are much larger than the extent of the SIS (thin lens approximation). Thus, the mass producing the deflection is the projected mass profile. It is therefore of interest to project the three dimensional density distribution and define the surface mass density:

$$\Sigma(r) = \frac{\sigma_v^2}{2Gr}. \tag{2.51}$$

Scaling by the critical density (Equations 2.31 and 2.32) we obtain a convergence (or scaled surface mass density) κ:

$$\kappa(r) = \frac{2\pi\sigma_v^2}{c^2 r}\frac{D_{LS}}{D_{OS}} = \frac{\theta_{E,SIS}}{2\theta} = \kappa(\theta) \tag{2.52}$$

where we have identified the angular Einstein radius $\theta_{E,SIS}$ as:

$$\theta_{E,SIS} = \frac{4\pi\sigma_v^2}{c^2 G}\frac{D_{LS}}{D_{OS}}. \tag{2.53}$$

By integrating the surface mass density we obtain the (projected) enclosed line-of-sight mass:

$$M(r) = \int_0^r 2\pi r'\Sigma(r') = \frac{\pi\sigma_v^2 r}{G}. \tag{2.54}$$

Using this enclosed mass, the deflection angle (as in Equation 2.37) becomes:

$$\hat{\alpha}(r) = \frac{4GM(r)}{c^2 r} = 4\pi\frac{\sigma_v^2}{c^2}. \tag{2.55}$$

Solving Equation 2.24 with this deflection angle, we obtain the two dimensional lens potential:

$$\psi(\theta) = \frac{4\pi\sigma_v^2\theta}{c^2 G}\frac{D_{LS}}{D_{OS}} = \theta_{E,SIS}\theta. \tag{2.56}$$

Using Equations 2.26 and 2.33 the magnification μ is

$$\mu(\theta) = \frac{1}{1 - \frac{4\pi\sigma_v^2}{c^2 G r}\frac{D_{LS}}{D_{OS}}} = \frac{1}{1 - \frac{\theta_{E,SIS}}{\theta}}. \tag{2.57}$$

The Singular Isothermal Ellipsoid (SIE)

Realistic lenses, however, are in general not perfectly spherical, but have a an ellipticity. In this case we can break the spherical symmetry of the SIS to obtain a SIE potential:

$$\psi(\varsigma) = \theta_{E,SIE}\varsigma \tag{2.58}$$

with convergence:

$$k(\xi) = \frac{\theta_{E,SIE}}{2}\frac{1}{\varsigma} \tag{2.59}$$

where the angular Einstein radius is:

$$\theta_{E,SIE} = \theta_{E,SIS}\frac{\sqrt{1-q^2}}{arcsin(\sqrt{1-q^2})}. \tag{2.60}$$

q is the projected axis ratio and $\varsigma^2 = x^2 + y^2/q^2$ is the elliptical radial coordinate. When $q \to 1$ the SIE profile corresponds to a SIS profile.

There is no general analytic solution of the lens equation with elliptical profiles such as the SIE. When solved numerically, a SIE lens, produces diamond shaped caustics due to the tidal perturbation induced by its ellipticity. As shown in Figure 2.6, this configuration can map a single source to four images in the lens plane.

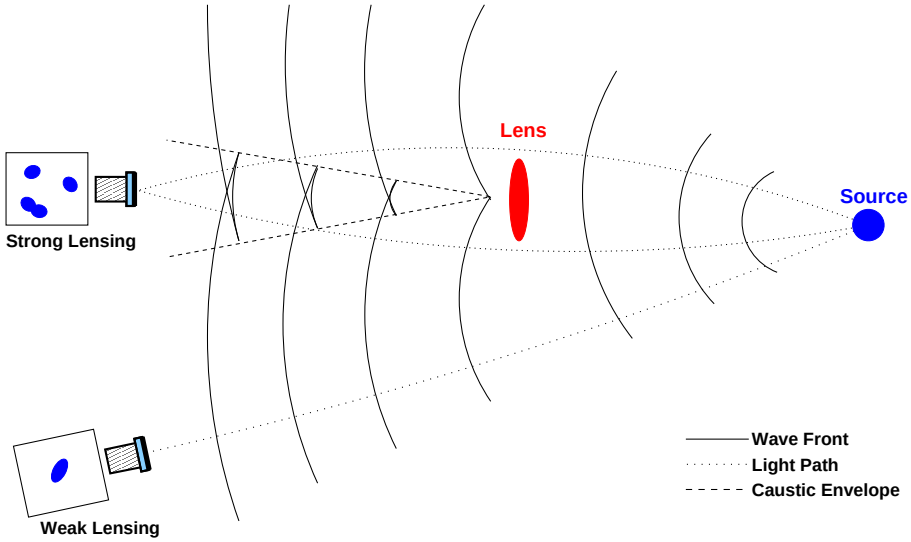

Figure 2.7: *Strong and weak lensing regimes. The source wavefront is distorted by a massive intervening object. The caustic envelope indicates the region where image splitting can be seen (strong lensing).*

2.3.3 Gravitational lensing regimes

Within the scope of gravitational lensing we can distinguish two different regimes: strong and weak. To interpret the difference between these two, it is useful to imagine different line-of-sight paths in a wavefront distorted by an interveining massive body, as shown in Figure 2.7. In the following, we present a description of each regime.

Strong lensing

Strong lensing is the case when the observer, the lens and the source are close to alignment so that there is splitting of images from the source (i.e., the surface mass density is larger than the Σ_{crit} defined in Equation 2.32). In this case, the observer's line-of-sight is located inside the caustic envelope, where the wavefront is highly distorted (see Figure 2.7), producing multiplicity of images and mirror inversion of images located at saddle points. In general, strong lensing refers to lensing systems in which the lens is a galaxy or galaxy cluster, and the source is a background galaxy or quasar. Due to the (small) projected velocities of galaxies and galaxy clusters with respect to background sources, strong lensing is a static phenomenon in human time scales.

Strong lensing observables are the positions and brightnesses of the lensed images. Being a static phenomenon, the intrinsic brightness of the source is unobservable. Thus, individual brightnesses of lensed images do not give any information about the lensing system. However, the ratio between the brightnesses of multiple images does, as it corresponds the ratio between the magnifications produced by the lensing potential.

Even though galaxy-galaxy lensing is more common than quasar lensing, lensed quasars have been the most common detection for decades. This is mainly due to the high luminosities shown by these objects and historical reasons (dedicated surveys). Strong lensing of quasars is a powerful tool to measure the mass and mass density profiles of lensing galaxies. It is completely independent of the dynamical state or luminous property of matter in galax-

ies. As lensing magnification depends on the second derivatives of the lens potential, it is sensitive to anisotropies of the potential. Hence, through flux ratio anomalies (inconsistencies among measured and modeled flux ratios between quasar images; explored in Chapters 3 and 4), strong lensing also potentially allows to probe for dark matter substructure in lensing galaxies (e.g., Dalal & Kochanek 2002). Using the fact that lensing (or at least strong lensing by galaxies and galaxy clusters) is an achromatic phenomenon, multi-band photometric or spectroscopic data of quasar images allow to measure galactic dust extinction in lensing galaxies (e.g., Elíasdóttir et al. 2006). Using photometric light curves of lensed quasar images of an intrinsically varying source, the time-delay between them can be measured. Comparing these measured time-delays with the expectations from modeled lensing potentials, results in a value of the Hubble constant H_0 (Refsdal 1964a), independent from other methods. Additionally, through angular diameter distance ratios of multiple sources in a lensing system, the values of the geometric cosmological parameters Ω_M and Ω_Λ can be constrained (Golse et al. 2002). An extensive and detailed description of the applications of strong quasar lensing can be found, for example, in Claeskens & Surdej (2002).

The analysis of strong quasar lensing systems will be explored in the following chapters of this dissertation. In Chapter 3 the different checks performed in order to confirm the nature of a lensed quasar are shown, as well as detailed mass modeling and discussion on flux anomalies of lensed images. Further on, in Chapter 4, the study of flux anomalies in lensed quasars will be more intensively studied.

Weak lensing

Weak lensing refers to the case when the line-of-sight path from the source to the observer, is perturbed by a massive body, but is outside the caustic envelope, as shown in Figure 2.7 (surface mass density lower than Σ_{crit}). In this case, no multiple images are created, but the images of background sources are distorted and magnified (by the convergence κ and shear γ produced by the lens at the position of the images as shown in Figure 2.5). There is a rather smooth transition between weak and strong lensing, where these sheared images begin to form arcs around the lens. Nonetheless, in the general weak lensing case, the background sources are sheared only by a few percent.

If the original shape of a weakly lensed galaxy was known, the deformation induced by weak lensing could suffice to deduce the properties of the lens. However, the main problem weak lensing faces, is the fact that an exact knowledge of the intrinsic shape of distorted background galaxies does not exist. To get around this issue, astronomers look towards regions in space more likely to produce weak lensing distortions (i.e., around massive clusters which produce distortions of $\sim$10%) and assume that the distribution of the background galaxies is random. This fact compensates for the lack of knowledge of their exact shapes and can constrain the mass distribution of large scale structure in the line-of-sight to the sources.

Weak lensing is one of the most promising tools to understand and measure the dark nature of the universe and constrain the value of cosmological parameters (for a review of weak lensing and its applications see Bartelmann & Schneider 2001).

2.3.4 Microlensing

Even though microlensing is sometimes referred as a third lensing regime, it is, in principle, just a form or strong lensing. The term microlensing is used when the separations between

multiple lensed images of a background source are very small (micro to milli-acseconds), thus, unresolvable with any instrument or technique up to date. Fortunately, as the relative velocities between observer, microlens and source are high, microlensing is a dynamical phenomenon in human timescales (minutes to years). Without the possibility of resolving multiple images, the observational evidence for microlensing is the brightening and dimming of a background source induced by the total magnification μ and the relative movement of source and lens. Lenses within this scope are compact objects such as stars and planets.

Due to the dynamic property of microlensing, it is, in most cases, studied as an ensemble of individual events. It is useful, therefore, to define the microlensing optical depth. Microlensing optical depth is the ratio between the average microlensing surface mass density and the microlensing critical density (i.e., an averaged version of the convergence or scaled surface mass density κ defined in Equation 2.31). It can be written in its continuous form as (Paczynski 1986):

$$\tau = \int_0^{D_{OS}} \frac{4\pi G D'_{OL} D_{LS}}{c^2 D_{OS}} \rho(D'_{OL}) dD'_{OL} \tag{2.61}$$

where $\rho(D'_{OL})$ is the average lensing mass density at a distance D'_{OL} from the observer. Microlensing optical depth can be interpreted as the probability of a given source to be undergoing a microlensing induced brightness modification at a given time.

Within the framework of microlensing we can distinguish three major varieties depending on the line-of-sight distances between the observer, the lens and the source, with very different microlensing optical depths as described hereafter.

Galactic microlensing

In this variety, both source and lens are inside the Milky Way. Due to the dynamics of our galaxy, it can happen that a foreground star becomes aligned with the observer and a background star, producing a magnification of the latter. As stated before, the magnification time scales depend on the projected velocities of the observer, the lens and the source. For an observer looking towards the galactic bulge of the Milky Way, the time scale of microlensing events is of the order of hours to weeks. The size of the Einstein rings produced by stars in the Milky Way (scale for image splitting shown in Section 2.3.2) is of the order of a fraction of a milli-arcsecond.

For galactic microlensing, the optical depth towards the bulge of the Milky Way is $\tau \sim 10^{-6}$, meaning that a random star in direction to the bulge of the Milky Way has a $\sim 10^{-6}$ probability of being affected by microlensing magnification at a given time. However, the millions of stars that can be seen towards the galactic bulge, allow $\sim$500 galactic microlensing events to be detected per year by monitoring campaigns such as OGLE (Udalski 2003) or MOA (Bond et al. 2001).

Modeling the light curves' variation due to microlensing of stars towards the bulge, presents several uses. By studying the projected velocities and time scales of the microlensing events, the dynamics of the bulge and Milky Way can be probed (Sumi et al. 2006). Also, the shape of the light curves allows to obtain constraints on the stellar atmospheres of source stars (e.g., Heyrovský 2003; Zub et al 2009, in preparation). Perhaps the most impressive of all the applications of galactic microlensing is the search for extrasolar planets (e.g., Gould & Loeb 1992; Wambsganss 1997; Beaulieu et al. 2006). If the star acting as a lens has a companion (such as a planet), the lens potential diverges from that of a Schwarzschild lens (see Section 2.3.2) and produces more complicated caustic patterns. The relative movement between the

source and this caustic pattern can produce a characteristic light curve, which can be used to obtain constraints on the mass and separation of the binary system. The probability of such an event happening is fairly low, nevertheless, until now there have been several planets discovered this way (see Gould 2008). The main advantage of microlensing as a planet finding method when compared to others such as radial velocity measurements, direct imaging or transits, is its sensitivity to Earth-mass planets in the habitable zone (Wambsganss 1997; Park et al. 2006).

Local Group microlensing

Moving up in the microlensing distance ladder we can define an intermediate microlensing variety that is when the lensed sources are objects within the Local Group.

In this classification we find the microlensing of stars in nearby galaxies by Massive Compact Halo Objects (MACHOs) in the Milky Way. Several collaborations such as MACHO (Alcock et al. 2000), EROS (Tisserand et al. 2007) or OGLE (Zebrun et al. 2001) were dedicated to monitoring stars in galaxies in the Local Group to observe MACHO induced brightness variations. This has been done in order to study the number and distribution of MACHOs in the Milky Way. The studies have yielded an unexpectedly low occurrence of such events (Alcock et al. 2000, shows a resulting optical depth of $\tau \sim 10^{-7}$ from the 5.7 years of the MACHO project), proving the hypothesis that the dark halo surrounding the Milky Way is entirely due to dark matter MACHOs, wrong. Even more, it is still unclear if the observed microlensing events unveiled by these collaborations are due to MACHOs at all.

These monitoring programs have had as a by-product the observation of "self-lensing" in galaxies of the Local Group. Self-lensing refers to the case when both lens and source objects come from the same galaxy. These kind of events have proven to be more common than MACHO lensing events. They allow to probe for the dynamics of galaxies in the Local Group (see for example Kerins et al. 2006), and maybe someday, extragalactic planets (Baltz & Gondolo 2001).

Cosmological microlensing

Cosmological microlensing, refers to the case in which both source and lens objects are located at cosmological distances. The main observation of this phenomenon is quasar microlensing.

Quasar microlensing, is an additional magnification (or de-magnification) that occurs on images of strongly lensed quasars. The light from multiple images of lensed quasars can encounter the gravitational potential of individual stars in the lensing galaxy (see Figure 2.8) and be re-magnified. This is possible due to the geometrical dependence of gravitational lensing induced magnifications and the fact that quasar accretion disks sizes are comparable to the Einstein rings of stars in the lens galaxies: Assuming a lens redshift of z_l=0.5, a source redshift of z_s=1.0, a mean mass for a microlensing star of $0.1 M_\odot$ and using Equation 2.41, we obtain a typical value for the Einstein Radius:

$$R_E = \sqrt{\frac{4G\ 0.1M_\odot}{c^2}\frac{D_{z_l,z_s}D_{z_s}}{D_{z_l}}} \approx 0.004\ pc \tag{2.62}$$

which, as shown in Section 2.1.3, matches the scale of the size of the accretion disk of a quasar. As the Einstein radius is an intrinsic lensing scale, magnification or de-magnification of the multiple images of a background quasar can be seen.

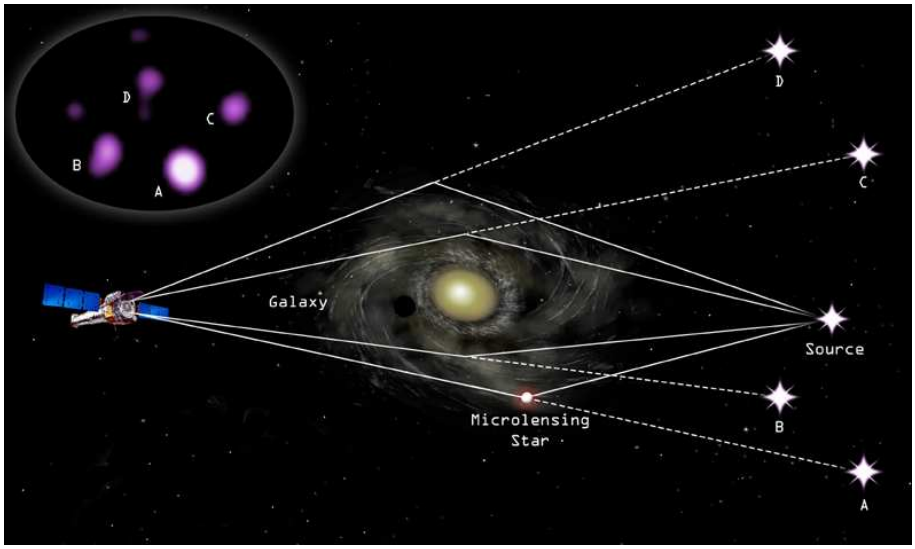

Figure 2.8: *Representation of quasar microlensing. The light from the lensed image A of the background quasar, gets re-magnified by a star in the lensing galaxy. Thus, image A appears brighter to the observer than what expected from the magnification induced solely by the galaxy lensing potential (top-left insert). Credit: X-ray: NASA/CXC/Penn State/G.Chartas et al; Illustration: NASA/CXC/M.Weiss.*

Quasar microlensing has a much higher optical depth ($\sim$1) than galactic microlensing, as the projected density of stars in the lensing galaxies on top of quasar images is larger. Thus, it has a much more complicated microlensing potential produced by numerous compact objects. The projected distances and velocities of the observer, microlenses, "macro" lens (galaxy) and source, set the time scale for quasar microlensing events between several weeks to a decade, making of quasar microlensing an observable phenomenon in human time scales. In fact, many lensed quasars have shown evidence for microlensing and have been monitored for years, showing microlensing induced brightness fluctuations (e.g., Corrigan et al. 1991; Borgeest & Schramm 1993; Woźniak et al. 2000; Udalski et al. 2006; Chartas et al. 2006). The study of these variations can be used to probe the dynamical properties of the lensing galaxies and the structural parameters of the background quasar (e.g., Wambsganss et al. 2000; Kochanek 2004; Gil-Merino et al. 2005; Anguita et al. 2008b; Eigenbrod et al. 2008).

Due to their complicated nature, the microlensing effect on quasars has to be simulated numerically (e.g., Wambsganss et al. 1990). The simulations are done by statistically studying the deflection induced by a distribution of microlenses. The output of such simulations are source plane two-dimensional magnification distributions which show complicated caustic patterns (see Figure 2.9). The path of a lensed quasar image in such a pattern, reveals the brightness fluctuations induced by microlensing.

Quasar microlensing is an important subject of this thesis, and hereafter is what we refer to as microlensing, unless specified. In Chapter 4 we will study the evidence for microlensing in four lensed quasar systems and in Chapter 5 we study microlensing induced brightness variations in the actively microlensed multiple quasar Q 2237+0305 (Huchra et al. 1985). Here, we will detail the use and manipulation of these magnification patterns, and how their coupling with astronomical observations allows to probe different properties of the system, including the internal structure of the background AGN.

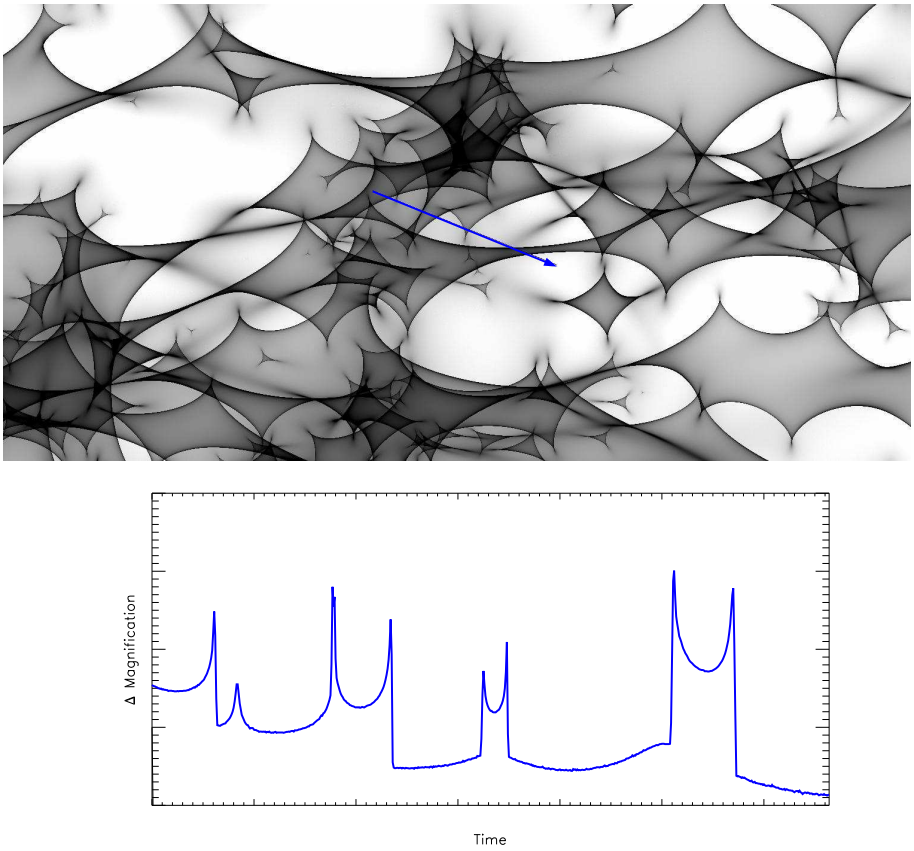

Figure 2.9: *$15R_E \times 7.5\ R_E$ cut of a source plane microlensing pattern. The pattern is the result of a simulation that follows light rays deflected by a distribution of microlenses. Dark areas show high magnification regions, and bright areas show low magnification regions. The bottom panel shows a one dimensional cut of the pattern in which the brightness variation experienced by a source moving through the blue path is displayed.*

2.3.5 Strong lens modeling

As explained previously in this chapter, strong gravitational lensing can be envisaged as a mapping of a bright background source to one or multiple images in the plane of the deflector. The process through which this is done is well understood (see in Section 2.3.1) and can be analytically described. This analytical description allows to study the inverse problem: using the observational signatures of gravitational lensing, we can obtain the otherwise unknown parameters that define this mapping. With "lens modeling" we refer to the modeling of the mass potential of the lens, required to produce such a configuration of observational signatures (image positions and brightnesses for given line-of-sight distances of lens and source).

There are two ways by which the modeling of a mass potential can be confronted: by performing a "parametric" or a "non-parametric" mass model.

Parametric lens modeling

As the name suggests, parametric mass modeling requires a parametric description of the potential. A specific, physically motivated, mass profile such as a de Vaucouleurs (de Vaucouleurs 1948), Singular Isothermal Sphere (SIS), Pseudo Isothermal Elliptical Mass Distribution (PIEMD: Kassiola & Kovner 1993) or Navarro, Frenk and White (NFW: Navarro et al. 1997) profile, to name a few, has to be chosen for the lens. The basic philosophy is to modify the parameters defining this profiles (and subsequently the lensing potential) and compare the resulting image (and flux) configurations to the observed data set. Iterating this procedure, the parameters that best define the mass profile are found.

Parametric minimization requires an educated guess on what the system is composed of and is therefore usually constrained by secondary observational signatures, that go from the ellipticity and position angle of the lensing galaxy to its effective light radius or stellar velocity dispersion. The fitting process generally consists of minimizing the square of the weighted distances (χ^2) between the observed and modeled image positions. In princile, in order to do this, a grid is created at the source plane and at the lens plane. By solving the lens equation (Equation 2.22) with a particular potential, a direct mapping between source and lens plane is obtained: for every cell in the lens plane grid a corresponding cell exists in the source plane grid. Naturally, a position on the source plane that implies the creation of multiple images ($\kappa(\theta)>\Sigma_{crit}$; see Equation 2.32), corresponds to multiple positions on the lens plane.

The minimization of the χ^2 can be done either in the source plane or in the lens plane. In the first case, each lens plane image maps itself to a source position on the source plane. Based on the fact that all multiple images in the lens plane come from a single source, the distance between the (at first instance) multiple (N) sources mapped to the source plane from the multiple (N) images in the lens plane are minimized. In the lens plane minimization, the process is inverted: one source plane position maps to, possibly, multiple image positions and the minimization is done on the χ^2 due the weighted difference between the modeled and observed image positions (on the lens plane). In both cases, this minimization can be complemented with constraints from the flux ratios between the images, as well as the time-delays. Image plane minimization provides a more precise result opposed to the approximate one from source plane minimization, but it is comparatively much more exhaustive computationally (for more information on parametric lens modeling see Kneib 1993; Keeton 2001b,a).

In the following chapter, we will show a parametric lens model obtained using the LENSTOOL

modeling code (Kneib 1993; Jullo et al. 2007). LENSTOOL does source plane χ^2 minimization, using a Bayesian algorithm (prior based minimization), and a Markov Chain Monte-Carlo (MCMC) process that samples the probability distribution by random variation of the parameters. The scanning of the parameter space avoids hitting local χ^2 minima and allows a very robust result with minor speed trade-off. The details of the algorithm and the underlying statistics are described in Jullo et al. (2007).

Non-parametric lens modeling

Contrary to the parametric approach, non-parametric lens modeling is not fixed to a specific chosen profile, but allows slight variations over a given mass profile, or even a completely independent one. The most successful non-parametric approaches to mass modeling are: the multipole expansion method (e.g., Kochanek 1991; Trotter et al. 2000) and the pixelization method (e.g., Abdelsalam et al. 1998; Saha & Williams 1997; Saha 2000; Diego et al. 2005).

The multipole expansion method, as the name suggests, is a Taylor expansion of the lens potential. In other words, perturbations are added to the mass density profile in order to reproduce the observed constraints. This kind of perturbative process is then a transition between parametric and non-parametric modeling, as the terms in the Taylor expansion are indeed parametrized. However, it allows to retrieve more complicated potentials.

The pixelization method, on the other hand, makes no strong assumption on the mass density profile. In this case, the mass producing the deflection is defined on a grid of pixels. PIXELENS (Saha & Williams 1997; Saha 2000; Saha & Williams 2004) is the most widely used code in this sub-class. Its minimization method is based on the time-delay surface (see Section 2.3.1). By using pixelated maps, the time-delay surface (see Equation 2.36) can be written as (Saha & Williams 1997):

$$t(\overrightarrow{\theta}, \overrightarrow{\beta}) = \frac{1}{2}|\overrightarrow{\theta}|^2 - \overrightarrow{\theta}\overrightarrow{\beta} - \sum_n \Sigma_n Q_n(\overrightarrow{\theta}) \tag{2.63}$$

where Σ_n is the surface mass density of the n-th pixel and Q_n is proportional to the integral form of the potential (see Equation 2.25) on the same pixel.

Based on the fact that the locations of the images are on the extrema of this time-delay surface, the mass density in each pixel of the grid is optimized. PIXELENS requires that the parity and arrival time order of the images, and the time-delays between them (or the Hubble time: age of the universe; see Section 2.2) are known. Even though the approach is non-parametric (above the pixel scale), PIXELENS uses some priors on the mass profiles:

- All the surface mass density per pixel $\Sigma_n \geq 0$.
- If the galaxy does not appear very asymmetric, the mass profile is required to have inversion symmetry about the lens center.
- The density gradient anywhere must point within $\leq 45°$ of the lens center.
- The Σ_n of any pixel must be $\leq 2\times$[average of neighbors], except for the central pixel, which is allowed to be arbitrarily dense.

Parametric versus non-parametric lens modeling

The most important difference between parametric (i.e., LENSTOOL) and non-parametric (i.e., PIXELENS) modeling is related to the number of constraints. In parametric modeling,

the number of fitted parameters needs to be lower than the number of constraints. Non-parametric modeling, on the other hand, is very under constrained. It has as many free "parameters" as pixels in the map, compared to the few observed image positions. This does not allow PIXELENS to retrieve individual accuracy measurements, but needs to obtain its uncertainties by studying the scatter of results from an ensemble of models.

In both parametric and non-parametric lens models, the use of a constant external shear γ to account for external perturbations of the potential by the environment is allowed. In the next chapter, besides LENSTOOL parametric modeling, we will show the use of the PIXELENS non-parametric approach to model the mass distribution of a lensing system. A working example of the advantages and disadvantages of each of them will then be presented.

3

Characterization of COSMOS 5921+0638: A Multiple Image Strong Lens Candidate

In this chapter, we explore the strong lensing phenomenon by showing a wide observational and theoretical analysis of the lensed quasar candidate COSMOS 5921+0638. We use different imaging and spectroscopic datasets to identify the observational characteristics of the lensing system as: the photometry, astrometry and redshift of the components. These parameters are later compared with theoretical concepts, revealing the mass of the lensing galaxy, the intrinsic luminosity of the source and flux anomalies in the lensed images. A condensed version of the work presented in this chapter will be submitted to A&A.

3.1 Strong lensing in the COSMOS field

The COSMOS survey[1] (Scoville et al. 2007) is a study of a 1.4°×1.4° "dust free" region in the equatorial plane (see Figure 3.1). It was selected like this to be probed deeply both with Northern and Southern hemisphere based telescopes. It has been extensively observed from both ground and space in most of the observable electromagnetic spectrum; from radio to X-ray, including: sub millimeter, infra-red: near, mid and far, optical: broad band, narrow band and spectroscopic, and UV: near and far. The survey is designed to probe the formation and evolution of galaxies as a function of redshift and the large scale structure environment.

Using the optical imaging data from the COSMOS survey, Faure et al. (2008) searched for strong gravitational lensing systems in the field. In order to maximize the lensing probability, they preselected massive ($M_V \leq$-20 [mag]), early type (according to the SED fitted for the photometric redshift) galaxies with photometric redshifts between z=0.2 and z=1.0. Within this sub-catalog (of ∼10,000 galaxies) they visually scanned the highest spatial resolution images available (HST/ACS F814W) of these galaxies, looking for arcs or multiple images. After a series of color checks and light profile fittings, a catalog of 67 strongly lensed candidate systems was created. Among these, 20 show multiple images of a single source or strongly elongated arcs, hence, very likely to be genuine lenses. With a similar scanning process,

[1] http://cosmos.astro.caltech.edu

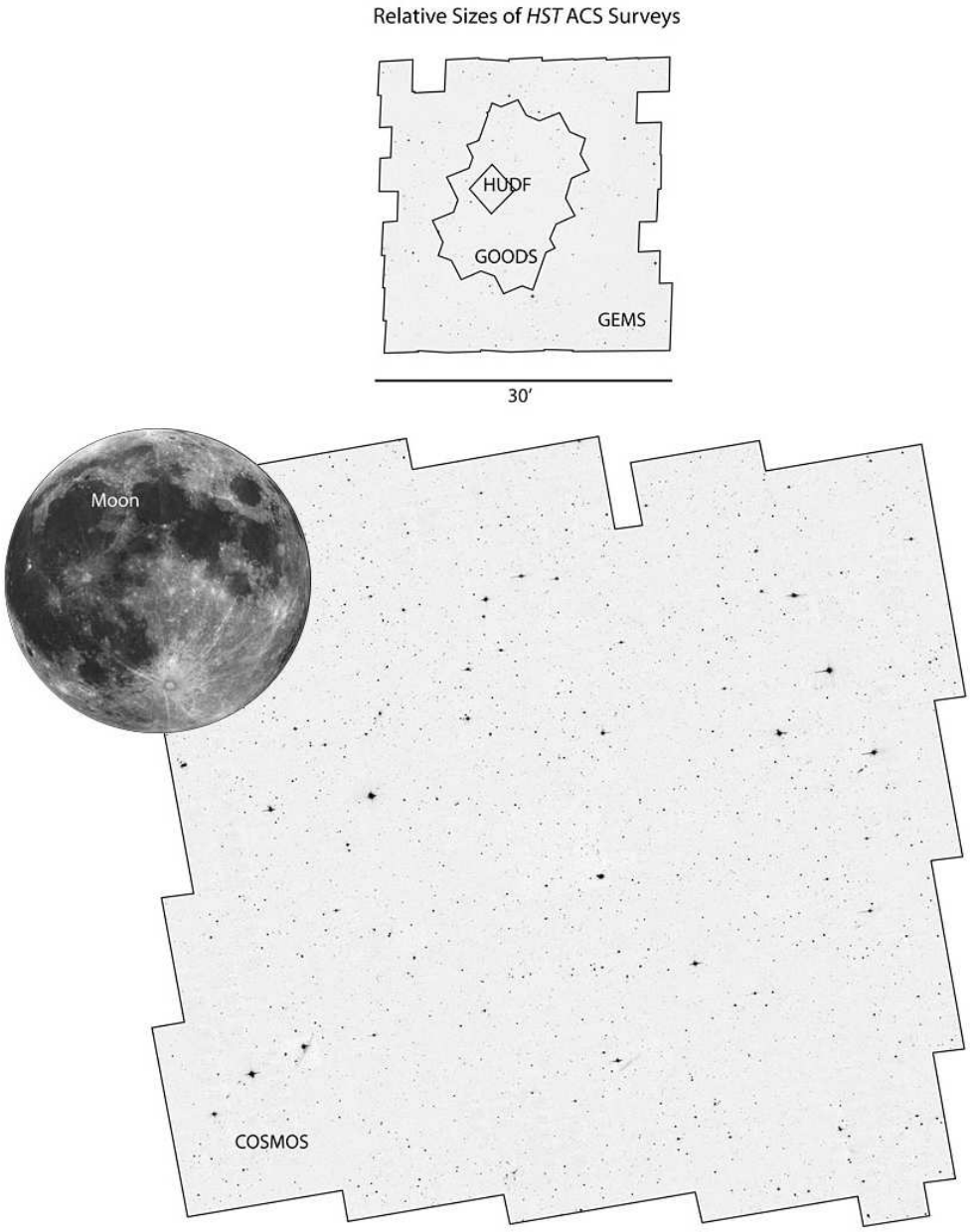

Figure 3.1: *Full view of ∼2 squared degrees of the COSMOS field (HST ACS mosaic). The relative sizes of the GOODS field (Dickinson et al. 2003), the Hubble Ultra Deep Field (HUDF; Beckwith et al. 2006), the GEMS field (Beckwith et al. 2002) and the Moon are shown for comparison. Credit: NASA, ESA and Z. Levay (STScI).*

Jackson (2008) mined the whole COSMOS catalog (ACS F814W magnitude<25: ∼280,000 galaxies) for strong lensing signatures. Three additional very likely strong lensing systems were presented among 115 candidates.

A large sample of lenses, provides an ideal laboratory for statistical lensing studies, including galaxy evolution and their dark matter content. In order to carry out these studies, the systems need to be confirmed as genuine strong lenses. Additionally, due to the selection method of the COSMOS lens candidates, the sample potentially contains systems with exceptional individual properties. For these reasons, these candidates and their environment are currently being followed up in order to accurately measure their characteristics.

The remainder of this chapter shows a detailed study of one of these lens candidate systems: COSMOS 5921+0638 (RA=$09^h59^{min}21.7^s$, DEC=$+02°06'38''$). The system is composed of four point-like objects that lie on top of a perfect ring around an early type galaxy (see Figure 3.2), with a photometric redshift of $z_l^{phot}=0.45\pm^{0.03}_{0.05}$ (Faure et al. 2008). The shape of the system suggests that it is a lensed AGN, with the ring being formed by the AGN's host galaxy, similar to RXSJ 1131-1231 (Sluse et al. 2003) or PG 1115+080 (Impey et al. 1998).

3.2 Imaging and spectroscopic dataset

3.2.1 Imaging dataset from ground and space

Due to the large wavelength coverage of the COSMOS field, we have access to extensive imaging of the system and its neighborhood. Among these, COSMOS 5921+0638 was covered from the ground based telescopes Subaru and CFHT in Hawaii using the B, V, r+, i+, z+ and $u^\star$ bands (data described in detail by Capak et al. 2007). From the Hubble Treasury programs (Scoville et al. 2007) we have HST/ACS observations in the F814W band (the data reduction process is detailed in Koekemoer et al. 2007). Additionally, we have used recent (January 2008) WFPC2 F606W exposures of the system (HST proposal id: 11289, PI: Kneib) that are part of the Strong Lensing Legacy Survey (SL2S, Cabanac et al. 2007) where the system was also serendipitously found. In Figure 3.2 we display the HST images of the system with the chosen naming scheme for the point-like images (A to D, clockwise from the east-most image), which will be used hereafter, and in Figure 3.3 we show the CFHT and Subaru images. Even though the COSMOS field has also been observed in the radio and X-ray regime, no signal has been measured for the system, as already mentioned in Faure et al. (2008). We have summarized the properties of the imaging dataset used in this study in Table 3.1.

3.2.2 Spectroscopic dataset

Galaxies in the COSMOS field have been spectroscopically observed as part of the zCOSMOS survey (Lilly et al. 2007). zCOSMOS is a large redshift survey within the COSMOS field using the VIMOS spectrograph installed at the VLT. It is divided into two surveys: zCOSMOS-bright and zCOSMOS-deep. zCOSMOS-bright aims to measure the spectroscopic redshift of 20,000 I-band selected galaxies at redshifts <1.2 in 1.7 square degrees within the COSMOS field. zCOSMOS-deep, on the other hand, is targeted at spectroscopically measuring the redshift of 10,000 galaxies at redshifts 1.5<z<3.0 in the central square degree of the COSMOS field. The second data release of the survey (zCOSMOS-bright DR2, released in October 2008; Lilly & Zcosmos Team 2008), contains 10,643 spectra with associated redshifts. The galaxy

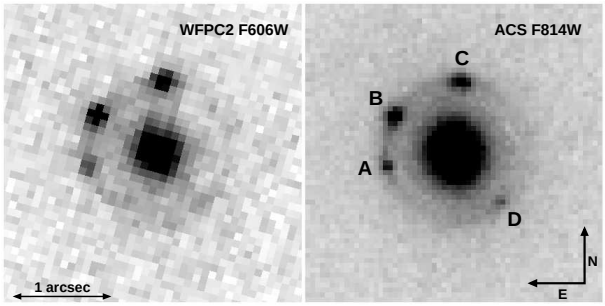

Figure 3.2: *HST 3 arcseconds side length cut-out images of COSMOS 5921+0638. The left panel shows the WFPC2 F606W exposure and the right panel shows the ACS F814W exposure with the naming scheme selected for the point-like objects.*

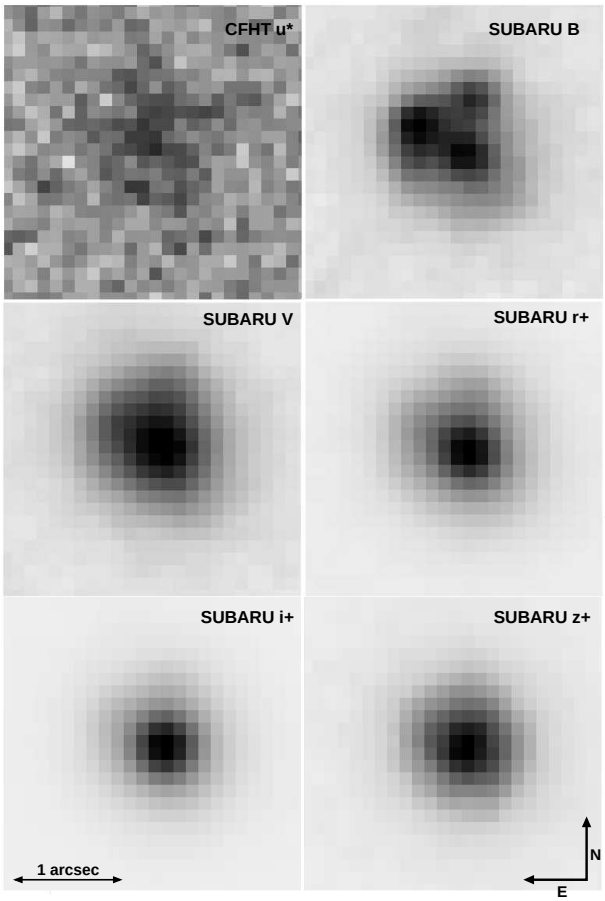

Figure 3.3: *CFHT/Megacam and SUBARU/Suprime images of COSMOS 5921+0638. The 3″ side length images are displayed from shorter (u^*) to longer ($z+$) wavelength from left to right, top to bottom.*

Table 3.1: *Summary of the different imaging data used for this analysis. The magnitude limits for the COSMOS observations are those shown in* Capak et al. *(2007) for the ground based observations and in* Koekemoer et al. *(2007) for the HST observations. (a) The u⋆ frame was created by combining observations taken between the years 2004 and 2005, thus, the total exposure time in this band for the COSMOS field varies. (b) 27.1 is the magnitude limit for a point-like object in the ACS exposure and it drops to 26.1 for a 1″-wide extended object.*

Camera	Band	Date	Exp. [s]	Limit [mag]
Suprime	B	2004-02-19	4320	27.3
	V	2004-02-18	3240	26.6
	r+	2004-01-19	2160	26.8
	i+	2004-01-22	2880	26.2
	z+	2004-01-21	4320	25.2
Megacam	u⋆	2004-2005$^{(a)}$	∼40000	26.4
ACS	F814w	2004-04-08	2028	27.1$^{(b)}$
WFPC2	F606W	2008-01-07	1200	26.5

redshifts in the field around COSMOS 5921+0638 from this data release are displayed in Figure 3.6.

Besides the zCOSMOS spectra and redshifts, the fields of 8 of the 67 strong lens candidates presented by Faure et al. (2008), including COSMOS 5921+0638, have been observed with the FORS1 instrument at the VLT in Multi Object Spectroscopy mode as part of a follow up program (PI: Faure, Proposal ID: 077.A-0473(A)). The FORS observations around the field of COSMOS 5921+0638 were obtained in April 2006 and presented in this chapter. They comprised a $7' \times 7'$ field centered on the system with the GRISM 150I (wavelength coverage: [3300 - 6500]Å, resolution: 5.54Å/pixel) with a total exposure time of 1800s. The standard CCD reduction and the spectra extraction was done using the pipeline recipes from ESO[2] while the flux calibration was done using the long slit spectrum of the LTT7379 standard star and IRAF routines[3]. In Figure 3.4 we display the position of the central slit, placed on top of the system: the goal of it was to measure the redshift of the central galaxy, as well as to obtain spectroscopic signal from the close north-east point-like objects.

3.3 The nature of the system

The lens nature of an object is confirmed with the fulfillment of different steps, such as the number, relative brightness and configuration of the candidate lensed images. The first step is the confirmation of the line-of-sight alignment of the foreground "lens" and the background "source" with the observer through redshift measurements. However, in some cases, these can be difficult to confirm. For instance, the lens or the multiple images of a source can be too faint, making it hard to acquire proper spectroscopy to measure their redshifts and corroborate that in fact the candidate lens and source are foreground and background objects,

[2]http://www.eso.org/sci/data-processing/software/pipelines/fors/fors-pipe-recipes.html

[3]IRAF is distributed by the National Optical Astronomy Observatory, which is operated by the Association of Universities for Research in Astronomy (AURA) under cooperative agreement with the National Science Foundation.

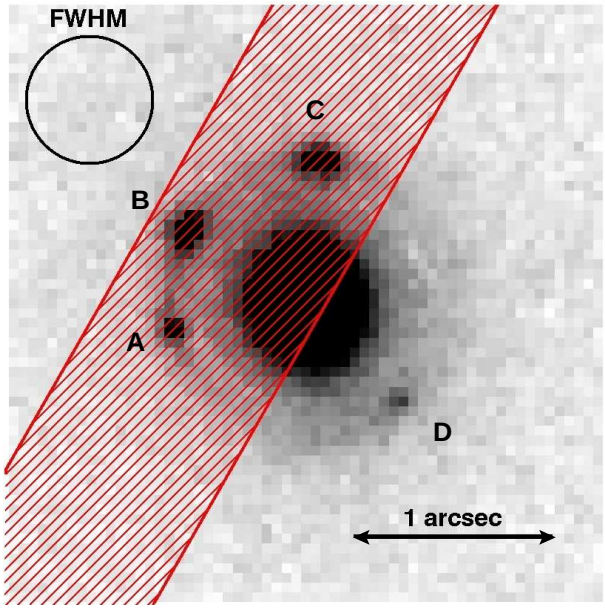

Figure 3.4: *Placement of the slit containing the three (brightest) images and the lensing galaxy towards COSMOS 5921+0638 shown over the high resolution 3″ side length ACS image cut-out. The FWHM of the VLT FORS observations is shown on the top left corner of the image. The coarser FWHM plus the dispersion direction (perpendicular to the orientation of the slit) makes the spectrum highly contaminated by the brighter galaxy.*

respectively. This is precisely the case in COSMOS 5921+0638: the point-like images are very faint (see Section 3.4). Nevertheless, we can gather an ensemble of clues that allow to conclude on the gravitational lens nature of the system.

3.3.1 Multi-band images

The distribution of the point-like images around the central galaxy shows a typical strong lens configuration: a pair of close images (A and B) and two images spread north (C) and south-west (D), similar to the configuration of lensed quasar PG1115+080 (Schechter et al. 1997), MG0414+0534 (Hewitt et al. 1992) or WFI J2033-4723 (Morgan et al. 2004). Moreover, the point-like shape of the images suggests that the background source is an AGN. This hypothesis is also supported by the fact that we can see in the HST images that a smooth structure forms a perfect Einstein ring under the point-like images that can be interpreted as emission from the host galaxy of the AGN. If so, we would expect the point-like images to have typical AGN emission lines such as Lyα(λ=1215Å) or CIV (λ=1539Å).

As shown in Figure 3.3 the point-like structures have a very similar wavelength dependence. In the CFHT/Megacam u* band images (limiting magnitude=26.4 mag, central wavelength=3797Å), where there should be very low contamination by the galaxy (based on the photometric redshift z$\sim$0.5, the 4000Å break should be at $\sim$6000Å), we cannot see emission from the point-like images either. The multiple images start to become visible in the Subaru/Suprime cam B band frames (limiting magnitude=27.4, central wavelength=4459Å), where their brightness is comparable to the galaxy. Moving to longer wavelengths, they get rapidly contaminated by the galaxy. This behavior suggests that the point-like images are

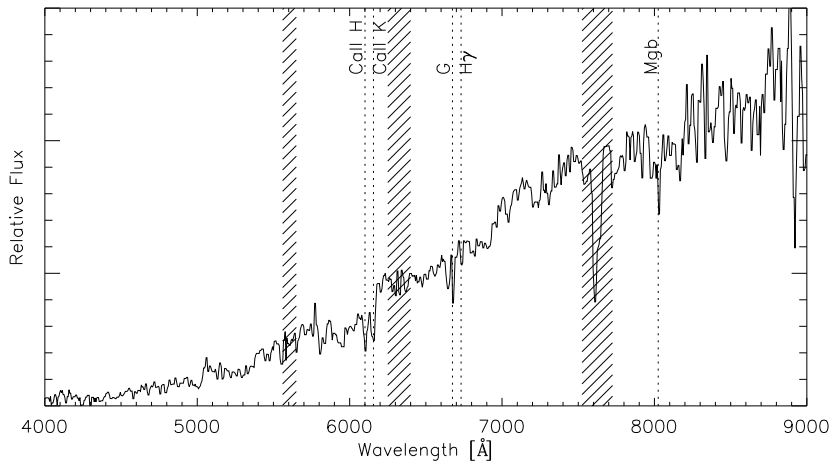

Figure 3.5: *The linear flux calibrated VLT/FORS1 spectrum (smoothed) of the central lensing galaxy towards COSMOS 5921+0638. Identified lines are labeled. Shaded areas denote regions with strong sky emission or absorption.*

related to each other and gives by itself an estimate for the redshift of the source, similarly to the Lyman break technique (e.g., Giavalisco 1998) used for the detection of high redshift star forming galaxies. Assuming our background source is an AGN, which are Lyα emitters, we can classify it as a u* "drop-out". Thus, we can set the location of the Lyman break + Lyα line longwards of the u* band central wavelength, giving a lower limit for the redshift of the background AGN of $z_s \gtrsim 3$.

3.3.2 The FORS spectra

Using a slit covering a large portion of the system (see Figure 3.4), we were able to obtain a clear spectrum of the galaxy. The observed spectrum is consistent with a typical early type galaxy SED at a redshift of z=0.551±0.001 (see Figure 3.5). This value was derived using the CaII H, CaII K, G, Hγ and Mgb absorption lines.

Using the other slits of the FORS1 observations, we have been able to derive the redshift of 9 additional galaxies in the $\sim 7'$ field centered on COSMOS 5921+0638. In Figure 3.6 and Table 3.2 we report the location and the redshift of these galaxies.

Even though the slit of the FORS1 observations on top of this system is placed as to contain three of the point-like objects (see Figure 3.4), at first sight, no emission line from the point-like objects is visible. The single spectrum that could be extracted is highly contaminated by the much brighter galaxy in the spectral range. However, when subtracting an elliptical galaxy template spectrum (Kinney et al. 1996) from the observed spectrum (see Figure 3.7), a small feature is observed at 5050Å.

The asymmetric shape of this feature, suggests that it is Lyα emission. The fact that the galaxy is brighter than the AGN, specially at longer wavelengths, tells us that Lyα is the only emission line that could be seen: The Lyα line is in general brighter than other broad emission lines and is located (in this case) in the fainter part of the galaxy's spectrum, thus, less contaminated by it. This line yields a redshift for the point-like objects of z=3.14±0.05. This redshift is assigned by the single line (!) and the error determined by its width.

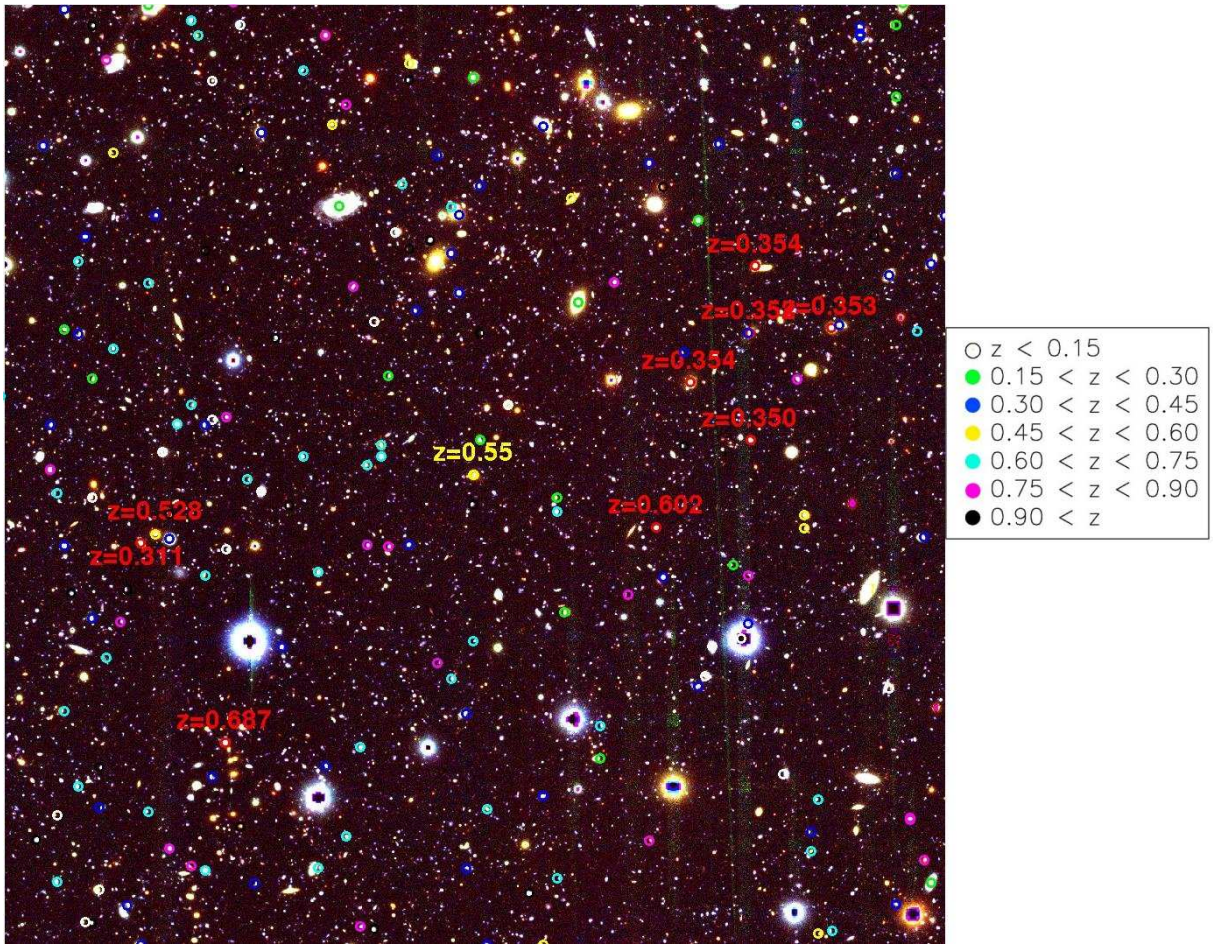

Figure 3.6: *Galaxies with measured redshifts from the FORS observations (red circles) of the ∼7′ field centered on COSMOS 5921+0638. A 8′×8′ cut-out of the field is shown. The galaxy indicated by the yellow circle in the center of the field is the main lensing galaxy of the system. The galaxies with redshifts from the zCOSMOS catalog are also displayed in color coded redshift bins.*

3.3.3 Conclusion on the point-like objects

The u⋆ drop-out suggests that, if this is a genuine lensed AGN, as hinted by the typical physical configuration of the system (four images of a source, a close pair, an Einstein ring formed by the host galaxy), the redshift would be z$\gtrsim$3. The identification of a Lyα emission line candidate using the FORS1 spectrum is evidence that this is indeed the case and the source is an AGN at a candidate redshift of z_s=3.14±0.05.

3.4 Astrometry and photometry of the system

Mass models of the lens depend on the brightnesses and, even more importantly, on the relative positions of the source images. It is hence necessary to accurately measure the astrometry (and photometry) of the images of the background source and the lensing galaxy in order to build a reliable mass model for the lens.

Table 3.2: *Galaxies with measured redshifts from our FORS observations in the field of COSMOS 5921+0638. The measured errors for the redshifts are* Δz=10^{-3}.

RA	DEC	z
09:59:09.69	02:07:53.6	0.353
09:59:12.21	02:08:25.4	0.354
09:59:12.39	02:06:56.4	0.352
09:59:12.41	02:07:51.2	0.352
09:59:14.44	02:07:26.0	0.355
09:59:15.59	02:06:12.0	0.602
09:59:21.79	02:06:38.7	0.551
09:59:30.27	02:04:22.0	0.687
09:59:32.69	02:06:08.8	0.527
09:59:33.24	02:05:47.6	0.312

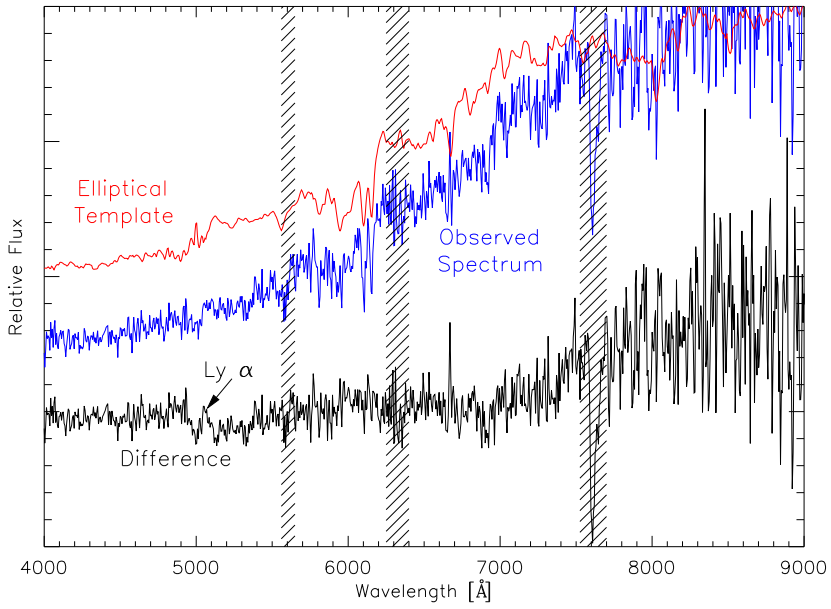

Figure 3.7: *The COSMOS 5921+0638 subtracted spectrum. The elliptical template spectrum (red curve) and the observed spectrum of the lensing galaxy + point-like images (blue curve) are shown. The difference between these two is displayed in the bottom (black curve). The difference spectrum shows an evident residual feature around 5050Å that we interpret as Lyα at z=3.14. Shaded areas denote regions with strong sky emission or absorption.*

For that purpose, we use the GALFIT software (Peng et al. 2002) on the WFPC2 (F606W) and ACS (F814W) space based observations. The software allows to fit analytical two dimensional light profiles to the objects seen in a frame, in our case, the four point-like images of the background source and the lensing galaxy.

3.4.1 The PSFs

GALFIT requires as an input the point spread function (PSF) of the observations in order to convolve it with the different analytical profiles. We obtained the PSF model for the WFPC2 observations from the "WFPC2 PSF library"[4]. The selected PSF was created using stars located on the same chip (#3) and with the same filter the observations presented here were done.

The ACS PSF, however, shows a much larger temporal and spatial variation than the WFPC2 PSF. So, in order to obtain an accurate PSF model, we referred to Rhodes et al. (2006, 2007) that show a statistical study which yields as a result a measure of the focus value f (to a micro-metric accuracy) of the different COSMOS ACS exposures. Using this information for the ACS exposure ($f\sim$-4.5μm) we used their IDL procedures[5] coupled with the TINYTIM[6] software to generate PSF models, in particular choosing those in the location of the CCD where the system is located, in the same way as we proceeded with the WFPC2 exposures.

3.4.2 Fitting the light profile

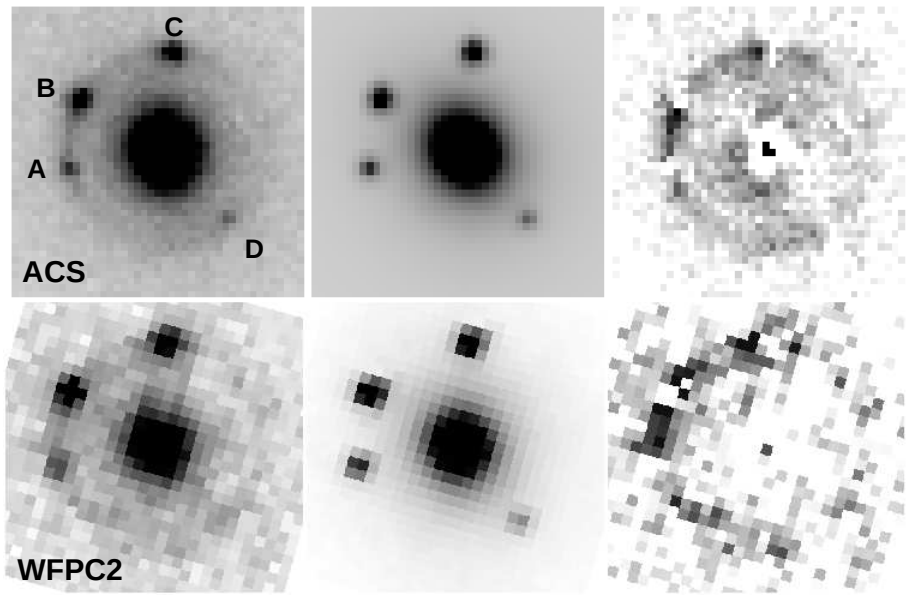

Figure 3.8: *Top Panel, left to right: Original ACS F814W exposure of COSMOS 5921+0638,* GALFIT *de Vaucouleurs + 4 point sources fitted model and residuals. Bottom Panel: the same display scheme for the WFPC2 F606W exposure.*

As the spectrum of the lensing galaxy matches that of an elliptical galaxy, the lensing galaxy was fitted by a de Vaucouleurs profile (de Vaucouleurs 1948). The parameters that define this profile are: the effective radius (R_{eff}), the central position, the ellipticity, the position angle (PA, defined in degrees measured from north to east) and the magnitude. The effective radius is defined as the radius at which one half of the total light of the profile is

[4]http://www.stsci.edu:8090/instruments/wfpc2/Wfpc2_psf/wfpc2-psf-form.html
[5]http://www.astro.caltech.edu/~rjm/acs/PSF/
[6]http://www.stsci.edu/software/tinytim

emitted and the ellipticity is defined as: $e=\frac{a-b}{a}$ (with a: semi-major axis and b: semi-minor axis).

The four point-like images were parametrized as point sources which have central positions and magnitudes as free parameters. Due to the lower resolution of the WFPC2 observations, the parameters that define the de Vaucouleurs profile are fixed to those obtained with the ACS fitting (with the exception of the magnitudes and central positions). In both cases, the background was fixed to the median value of empty regions selected in the field. The fitted light profiles and residuals are displayed in Figure 3.8. The parameters obtained for the galaxy are summarized in Table 3.3 and the photometry for the background source images in Table 3.4. Additionally, Table 3.5 shows the flux ratios, in reference to the bright image B, derived from these magnitudes. The fitted positions of the different objects in the system are displayed in Table 3.6. As the most accurate fit is obtained for the ACS exposure we quote and use throughout the rest of this chapter the astrometry obtained with this observation.

The error bars provided by GALFIT are based on the assumption that there has been a perfect fit to the data (i.e., χ^2=1), which is not the general case. Hence, to obtain error bars on the different parameters of the fit, we do 500 Monte Carlo realizations for each of the HST datasets and obtain the uncertainty from the scatter of the GALFIT results (see Appendix B). These errors are in close agreement with those shown by a single GALFIT fit on the ACS data, but in the WFPC2 data, where the fit of the lensing galaxy is not as good, the errors delivered by GALFIT, even though of the same order, are underestimated.

An attempt of light profile fitting was done on the ground based observations. However, due to the low quality of the PSF in these observations, the results were inconclusive.

Table 3.3: *Parameters of the de Vaucouleurs fit to the lensing galaxy towards COSMOS 5921+0638.*

Filter	R_{eff} [″]	e	PA	mag
F606W	0.45 (fix)	0.148 (fix)	27.3 (fix)	21.77±0.03
F814W	0.45±0.01	0.148±0.009	27.3±2.0	20.310±0.009

Table 3.4: *Photometry of the background AGN images in COSMOS 5921+0638, magnitude values. Images labeled as in Figure 3.2.*

Filter	A	B	C	D
F606W	25.85±0.13	24.82±0.07	24.98±0.07	26.88±0.30
F814W	25.42±0.06	24.59±0.03	24.53±0.03	26.19±0.10

The photometry of the lensing galaxy presented in the discovery paper (Faure et al. 2008), was done by fitting a disk (exponential) + bulge (sersic), which led to a slightly different ACS-F814W magnitude (20.34±0.02), albeit in agreement with the value presented here. On the other hand, the COSMOS ground based photometry of the lensing galaxy (Capak et al. 2007) was done considering the galaxy + 4 point sources + ring as a single object, thus, overestimating its brightness.

Table 3.5: *Flux ratios for the background AGN images in COSMOS 5921+0638 calculated with the magnitude values shown in Table 3.4.*

Date	Filter	A/B	C/B	D/B
2004/04/08	F814W	0.47±0.03	1.06±0.04	0.23±0.02
2008/01/07	F606W	0.39±0.06	0.86±0.08	0.15±0.04

Table 3.6: *Astrometry obtained with* GALFIT *for the background source images in COSMOS 5921+0638. All quoted values are in arcseconds with respect to the lensing galaxy.*

Filter		A	B	C	D
F814W	Δ_{RA}	0.702±0.005	0.617±0.003	-0.067±0.003	-0.468±0.008
	Δ_{DEC}	-0.132±0.005	0.382±0.002	0.727±0.002	-0.507±0.008

3.5 The neighborhood of COSMOS 5921+0638

Before building a mass model the system, we want to inspect the influence of secondary structures in the line-of-sight to the source that could perturb the lensing system. In order to do this, we use the zCOSMOS optical group catalog (Knobel et al. 2009, submitted). The catalog was created using the information of the second data release of the zCOSMOS redshift survey. It contains 800 galaxy groups characterized by different quantities among which we find, the "fudge" virial mass and the "fudge" velocity dispersion. These "fudge" quantities are obtained using the group richness and redshift as a medium to obtain the virial velocity and mass, adopting the observed relation between these and the mock catalogs created from numerical simulations for the COSMOS field.

In order to study the gravitational influence of these groups on COSMOS 5921+0638, we need to evaluate the total convergence κ and shear γ introduced by them. We select 21 groups located in a circle of ∼5 arcminutes radius (or 2 Mpc at redshift z=0.551) centered in COSMOS 5921+0638 (see Figure 3.9 and Table 3.7). Using the location and mass (or velocity dispersion) of these groups, we evaluate κ and γ at the position of the lens using three different assumptions for the mass profile of the groups: (i) point mass, (ii) Singular Isothermal Sphere and (iii) truncated isothermal sphere (see Appendix A for the formal treatment).

The point mass model assumes a singular total mass (which we selected as the virial mass), thus, there is no surface mass density outside the singularity and we can only observe the tidal shear γ produced by this mass. Assuming a Singular Isothermal Sphere (SIS) profile for the groups we can observe both the convergence and the shear (which are equal in this profile). Nevertheless, as the total mass of the SIS profile diverges, the values of κ produced by this profile are certainly over estimated far from the center of each group, which is the case in our analysis. Truncating the profile eliminates the issue. The virial radius[7] was chosen for this truncation.

By adding the individual κ and γ values (vector sum in the case of the shear) of the 21

[7]The virial radius, mass and velocity dispersion relate between each other through: $v=\sqrt{GM/R}$.

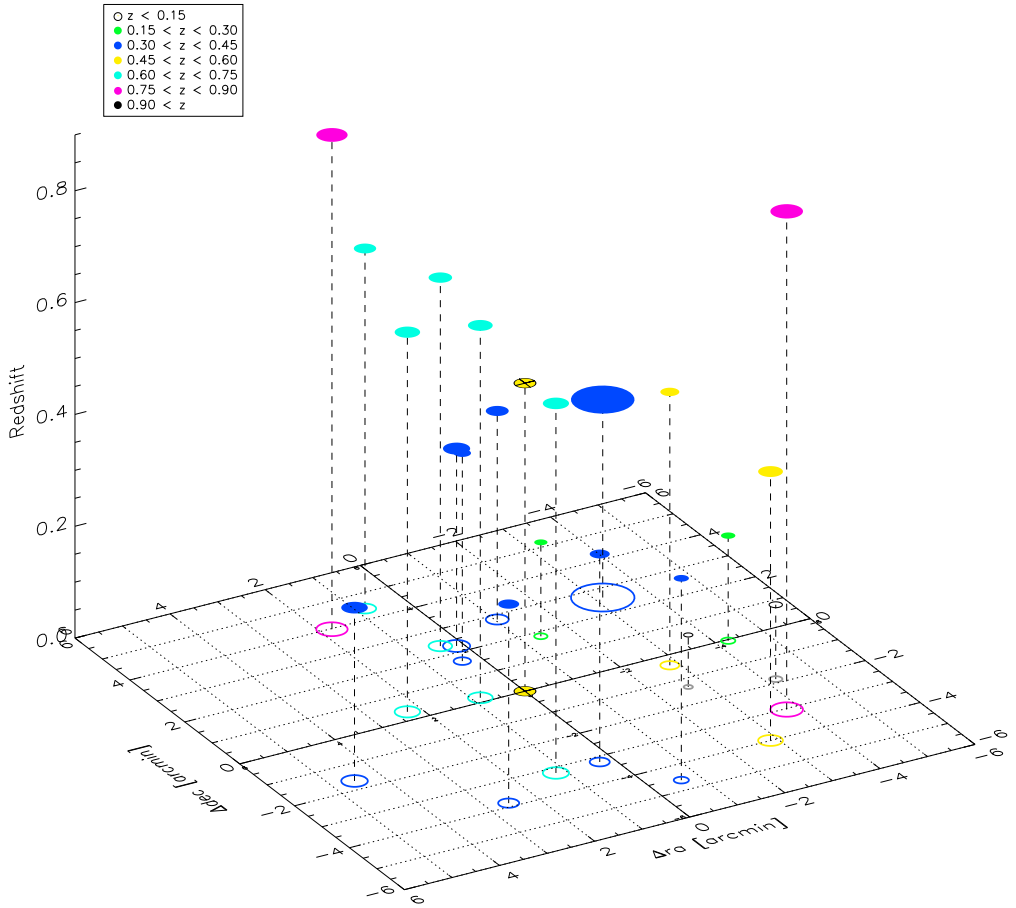

Figure 3.9: *The 21 groups from the zCOSMOS optical group catalog around COSMOS 5921+0638. Displayed as colored circles are the groups, the relative sizes of the circles scale with the "fudge" velocity dispersion. The lensing galaxy is displayed in the center as the yellow crossed circle. The groups are projected to the observer's plane as empty circles as a reference. The color coding matches that of Figure 3.6.*

Table 3.7: *Groups within a circle of about 5′ radius centered on COSMOS 5921+0638, sorted from closest to farthest (C. Knobel, private communication). The contribution of each group to the lensing potential at the position of the lensing galaxy as described in the text, is also displayed.*

Δ	Δ_{RA}	Δ_{DEC}	z	"Fudge" virial mass	"Fudge" σ_v	P. mass γ_{eff}	SIS $\kappa_{eff}=\gamma_{eff}$	Trunc. SIS κ_{eff}	Trunc. SIS γ_{eff}
[′]	[′]	[′]		$[M_\odot]$	[km/s]	$\times10^{-3}$	$\times10^{-3}$	$\times10^{-3}$	$\times10^{-3}$
0.90	0.84	0.17	0.666	6.9×10^{12}	278	6.70	9.81	3.79	9.21
1.77	0.37	1.65	0.372	1.6×10^{12}	195	0.66	2.88	0.98	2.62
2.35	0.14	2.24	0.353	9.1×10^{12}	305	2.02	5.07	1.85	4.69
2.40	-1.39	1.82	0.168	0.7×10^{12}	149	0.12	0.59	0.28	0.57
2.41	2.28	0.33	0.679	8.4×10^{12}	286	1.08	3.71	0.17	1.91
2.53	0.40	2.39	0.659	3.4×10^{12}	264	0.42	3.18	0.33	2.12
2.98	-2.82	-0.39	0.489	2.1×10^{12}	213	0.31	2.59	0.36	1.88
3.12	-2.66	-1.33	0.093	0.4×10^{12}	103	0.04	0.12	0.06	0.12
3.15	-1.04	2.82	0.373	3.5×10^{12}	257	0.45	2.81	0.32	1.92
3.38	0.28	-3.21	0.372	4.1×10^{12}	225	0.45	2.00	0.22	1.35
3.59	1.20	-3.21	0.661	4.9×10^{12}	294	0.30	2.77	0.49	2.16
4.32	-3.16	2.64	0.354	1.2×10^{14}	713	7.68	15.30	0.70	9.46
4.45	-4.25	-0.04	0.188	1.1×10^{12}	161	0.06	0.41	0.04	0.27
4.56	1.76	3.98	0.884	1.7×10^{13}	352	0.34	1.79	0.06	0.80
4.70	0.82	4.41	0.644	3.0×10^{12}	251	0.11	1.61	0.17	1.08
4.81	-4.21	-1.85	0.133	0.9×10^{12}	149	0.04	0.24	0.03	0.16
4.85	2.57	-3.85	0.356	4.0×10^{12}	236	0.21	1.48	0.08	0.79
4.87	-0.63	-4.60	0.361	1.0×10^{12}	170	0.05	0.77	0.07	0.49
5.05	-3.75	-3.04	0.891	1.7×10^{13}	366	0.27	1.72	0.05	0.74
5.06	4.54	-1.66	0.310	7.2×10^{12}	298	0.33	1.99	0.08	0.95
5.14	-2.86	-4.00	0.481	4.8×10^{12}	278	0.24	2.52	0.19	1.50

Table 3.8: *Total contribution of the groups around COSMOS 5921+0638 assuming the different profiles.*

	P. Mass	SIS	Trunc
κ_{tot}	0.000	0.063	0.010
γ_{tot}	0.006	0.007	0.004
$\theta_{\gamma,tot}$	21°	-39°	-35°

galaxy groups, we can obtain the total influence of the environment. Table 3.7 and Table 3.8 show the individual and total κ and γ produced by the groups, respectively. As expected, the total environmental convergence κ produced by the groups assuming point mass potential is zero. Assuming a SIS profile we observe total convergence κ=0.063 and for the truncated isothermal profile a much smaller κ=0.010. From the latter, we can see that the total κ contribution is negligible. However, it is important to remark that due to the fact that the total convergence is a sum of positive scalar values, incompleteness in the catalog (i.e., unidentified galaxy groups) leads to an underestimation of this value. On the other hand, total external shear is a vector sum, thus, incompleteness in the catalog may lead to an under- or overestimation of the value, resulting in a slighter effect on the total sum (even though the direction of this total shear can be compromised). Additionally, as shear is produced by tidal "pulls" from the mass distribution, the choice of potential profile, does not have a large influence on the final result (as shown in Table 3.7). The total external shear observed

is smaller than the variance expected by cosmic shear, thus, the γ contribution exerted by the zCOSMOS groups in the catalog cannot produce significant perturbations to the lens potential in COSMOS 5921+0638 either.

3.6 Mass modeling of the lens

In order to further confirm the lens nature of the system and understand its mass distribution, we perform a mass potential model of the lens. This is done using two types of mass models: non-parametric and parametric. The non-parametric models have the advantage of making no assumptions on the mass density profile of the lens. The parametric mass model, on the other hand, needs the assumption of a specific mass density profile, but in exchange returns information on the lensing galaxy that can be compared to observational quantities. In all of the models we assume that the lens plane is at z_l=0.551 and the redshift of the source is z_s=3.14.

3.6.1 Non-parametric mass model

The PIXELENS code (Saha & Williams 2004)[8] provides a non-parametric mass model of the lens employing the positions of the images. A requirement for the minimization is that the arrival time order of images is known. If incorrect image orders are put in, the model will either not converge or the fitted time-delay surface will reveal critical points in locations not occupied by images of the background source.

Using this fact, by trial and error, we can obtain the correct order for the images (and the type of singularity they sit on), which in this case is: C(minimum)$\mapsto$ A(minimum)$\mapsto$ B(saddle)$\mapsto$ D(saddle). Using this order for the images we obtain a non-parametric model for the lens. The time-delay contours for the correct image order are shown in Figure 3.10 (top left panel).

We tested two models: one without an external shear and one with. As the mass profile is free, a non-symmetrical mass distribution results from the fit. However, by dividing the mass distributions into symmetrical and non-symmetrical components (as shown in Figure 3.10, lower panel) we can see that the non-symmetric residual is rather small (in both cases).

For the model without an external shear, we obtain a mass profile with an ellipticity similar to the one of the observed galaxy, however, the position angle of this distribution appears to be larger than 45° (compared to the 27.3° observed position angle). The amount of non-symmetrical mass in the mass profile accounts for approximately 10% of the total mass.

The model with an external shear (shown in Figure 3.10) shows again a similar ellipticity as the observed galaxy, this time with a position angle similar to the observed one as well. Additionally, the non-symmetrical residual of the mass distribution accounts only for 7% of the total mass. These facts hint that, even though small, the contribution of an external shear is required in order to model this system, or there is a mass/light misalignment in the lens (e.g., Keeton et al. 1997). Note that regardless of the fact that the contribution from the asymmetrical part of the mass profile located south west of the center of the lens galaxy is low, it may be a hint for the requirement of some kind of substructure on the lens.

In both non-parametric fits (with and without external shear), due to the steepness degeneracy (Falco et al. 1985), having as constraints only the position of the images (lying on

[8]http://www.qgd.uzh.ch/projects/pixelens/

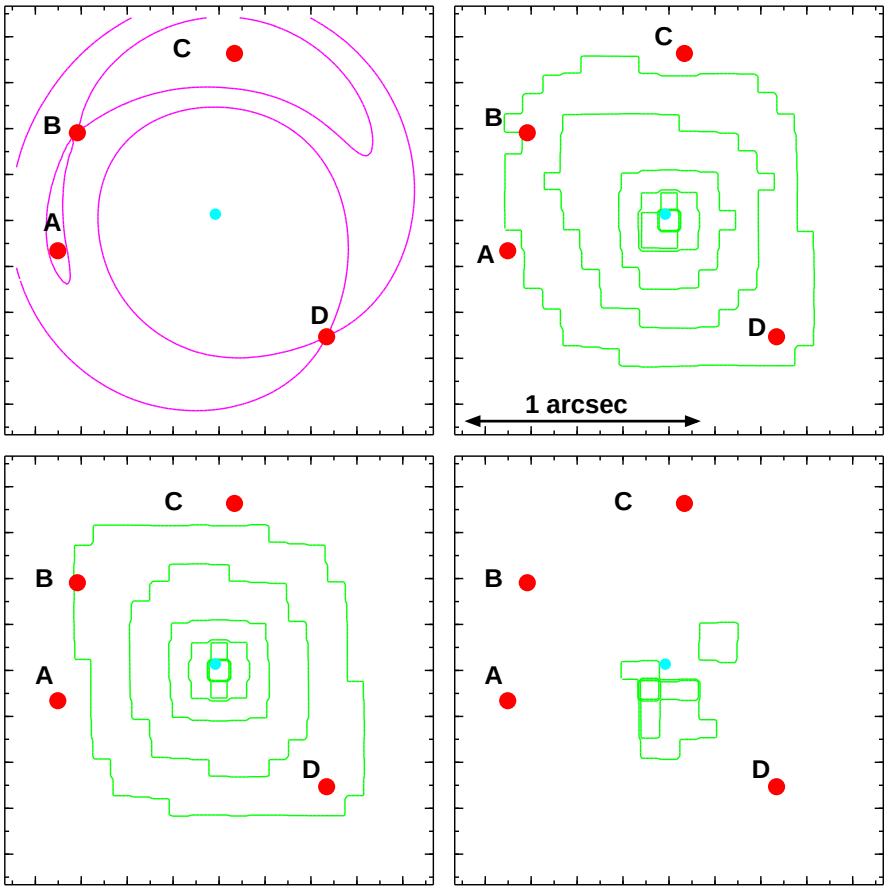

Figure 3.10: *Non-parametric model including external shear of COSMOS 5921+0638. The top left panel shows the time-delay surface contours which map the location of the critical points (saddle, maxima and minima), thus, the location of the images. The top right hand panel shows the fitted mass distribution while the bottom left and right panels show the symmetric and non-symmetric contributions to this mass distribution. Mass contours are defined as* $-2.5log(M)$*. The non-symmetric part accounts for approximately 7% of the total mass.*

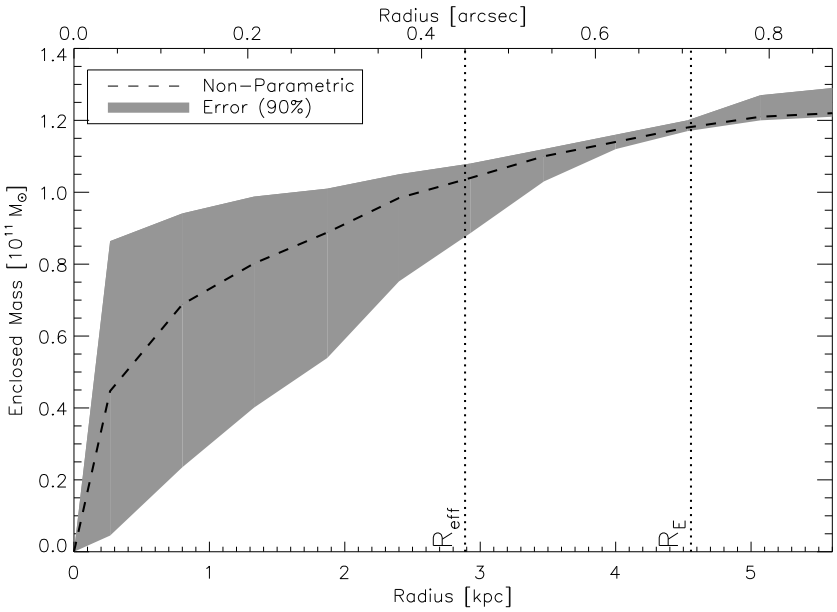

Figure 3.11: *Radially enclosed mass of the lensing galaxy in COSMOS 5921+0638 obtained with the non-parametric model which included external shear. The segmented lines display the effective radius (R_{eff}) fitted for the lensing galaxy and the measured Einstein radius (R_E) of the system respectively.*

a ring) and a low ellipticity, the slope of the profile is very degenerate (see Figure 3.11). Nevertheless, the total mass inside the Einstein ring (0.71″or 4.5 kpc at the redshift of the lensing galaxy) is well defined and amounts to $M_{R_E} \approx 1.2 \times 10^{11} M_{\odot}$ in the cases with and without shear. This is also expected from the expression of the Einstein radius for a point mass lens:

$$R_E = \sqrt{\frac{4GM}{c^2} \frac{D_{ls}}{D_l D_s}} \tag{3.1}$$

where R_E is the size of the radius of the Einstein Ring, D_l, D_s and D_{ls} are respectively the angular diameters distances between the observer and the lens, the observer and the source and the lens and the source. M is the total mass enclosed by the Einstein ring.

Time-delay values for both models are relatively similar but with large error bars. They are of the order of half a week for the longest delay (C to D) and of the order of a couple of hours for the shortest (A to B).

Non-parametric modeling (Saha & Williams 2004) gives us an interesting qualitative look to the mass profile distribution and familiarization with the system. However, being non-parametric, it naturally has a huge freedom in defining the mass profile and does not allow a quantitative comparison to the observations. The final pixelated map reflects the highest probability model from the ensemble of models tested (100 in our case).

3.6.2 Parametric mass model

In order to obtain a quantitative analysis on the mass model and compare with the information obtained with PIXELENS, we move on to attempt a parametric model of the system using LENSTOOL[9] (Kneib 1993). With LENSTOOL we do Bayesian source plane minimization of the parameter space (Jullo et al. 2007). This allows us to cover a large parameter space, as the Bayesian minimization avoids local minima. As an input for the modeling, we use the position constraints on the AGN images, with a conservative error of Δ=0.01″. This error accounts for the imperfections on the fitted position of the lensing galaxy due to the overestimation of the flux in its central cusp.

Constraining the galaxy's central position to its observational constraints ($\pm$0.01″), the ellipticity and position angle to the observed values and fitting a Singular Isothermal Ellipsoid (SIE) yields a poor fit to the data ($\chi^2_\nu \approx 100$), as expected from the results of the non-parametric modeling.

Table 3.9: *SIE and SIE+γ fit to the lensing galaxy in COSMOS 5921+0638. All observational constrains were fixed to the observed values. The galaxy's central position was allowed to move within 0.01″ that is the estimated uncertainty.*

	SIE	SIE+γ
Δx [″]	0.01	-0.0074$\pm$0.0027
Δy [″]	0.005	-0.0026$\pm$0.0026
σ [km/s]	190.7	189.3 $\pm$ 0.2
e	0.15 (fixed)	0.15 (fixed)
PA	27.3° (fixed)	27.3° (fixed)
γ	-	0.056 $\pm$ 0.003
PA_γ	-	-73.28 $\pm$ 1.52
χ^2_ν	$\sim$100	1.02

However, when we add to our SIE model an external shear, we obtain much better results as displayed in Table 3.9 and Figure 3.12. Figure 3.12 shows the comparison between the input AGN image locations (asterisks) and the found image locations (triangles). These found image locations come from the mapping of the average location of the minimized source position. The zoom in the right panel, allows to see the position of the source with respect to the caustics produced by the mass potential. The total mass within the Einstein radius matches the value inferred with the non-parametric model ($M_{R_E} \approx 1.2 \times 10^{11} M_\odot$).

As seen in Table 3.9, the model requires a small external shear (γ=0.058) in order to reproduce the observed image locations. The small strength of this shear is compatible with the fact that we do not observe a strong influence from the environment. It can indicate substructure, a slight misalignment between the light and the mass distribution in the lensing galaxy or contribution from individual galaxies close to the main lensing galaxy. However, at the time being, there is no spectroscopic measurement of the immediate neighbors. Nevertheless, the three brightest and closest neighboring galaxies (<6″, see Figure 3.13) are aligned in an $\sim$105° east from north, in close agreement with the modeled external shear. Their photometric redshifts indicate that are not at the same plane as the main lensing galaxy; using these redshifts and assuming singular isothermal profiles (using the analysis described

[9] http://www.oamp.fr/cosmology/lenstool/

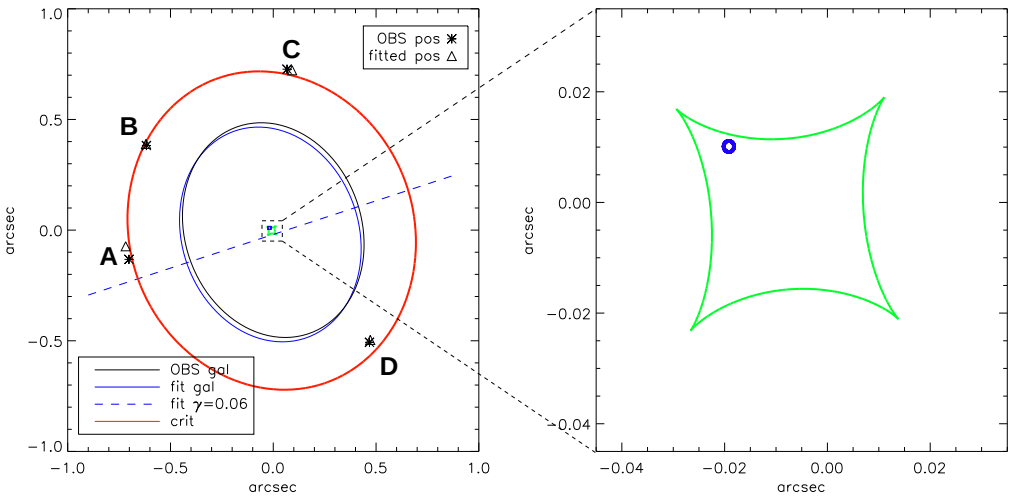

Figure 3.12: LENSTOOL*'s SIE+γ fit to the lensing galaxy in COSMOS 5921+0638. Left panel: The red curve shows the lens plane critical curve, the green curve shows the source plane caustics and the blue dashed line shows the orientation of the external shear. Asterisks denote the observed (A, B, C and D) image positions, and the triangles denote the modeled image positions. The blue circle shows the fitted source position. Right Panel: Zoom to the center of the system where the position of the source (blue circle) with respect to the caustics (green diamond shaped curve) can be seen.

in Appendix A), they could reproduce the required external shear if the three galaxies have velocity dispersions $\sigma\sim$300 km s^{-1}. Even when velocity dispersions of that order have been measured in galaxies, the low brightness of these candidates and the low probability of finding three aligned massive galaxies, makes it an unlikely possibility.

By having a parametric model, there are different properties of the system that we can check both in the lens and the source plane. The fitted description of the potential can be used to measure the values of convergence (κ), shear (γ) and magnification (μ) at different positions in the lens plane. With the modeled magnification values at the position of the images, we can measure then the expected flux ratios for the different images. The κ, γ, μ values and the flux ratios (with respect to image B) for the different images are displayed in Table 3.10. Comparing these modeled flux ratios with the observed ones (see Table 3.5), we can see a discrepancy. The possible explanations for this discrepancy are discussed in Section 3.7.

The magnification values displayed in Table 3.10 can be coupled to the measured photometry of the individual point-like images (Table 3.4) to obtain an estimate of the intrinsic brightness of the background source. We obtain an approximate absolute magnitude for the source of: $M_{606W}\sim$-17.4 and $M_{814W}\sim$-18.1. Even though this values are the median of the absolute magnitudes obtained for each image, which are subject to uncertainties due to flux ratio anomalies (see Section 3.7) and on the assumption of a SIE mass profile, they reveal the low luminosity nature of the source AGN (LLAGN; e.g., Storchi-Bergmann et al. 1995; Bower et al. 1996; Cid Fernandes et al. 2004).

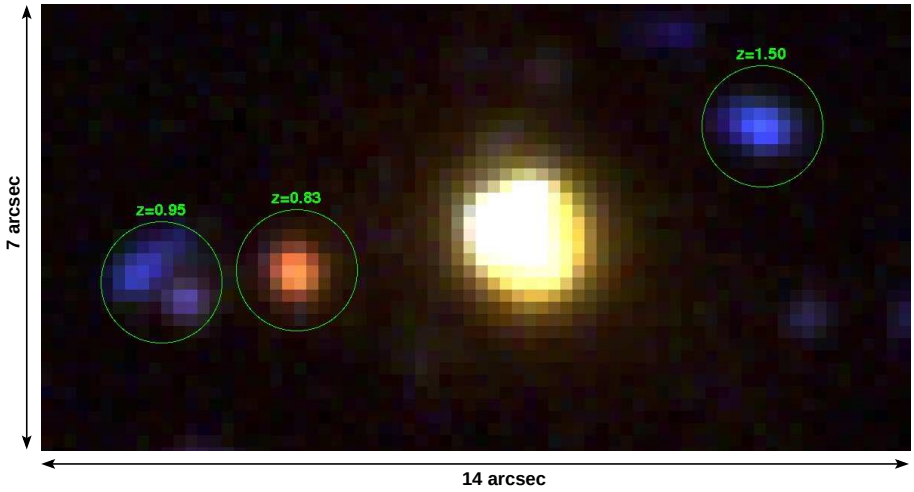

Figure 3.13: *Galaxies in the immediate neighborhood of COSMOS 5921+0638 with photometric redshifts displayed in green. Their alignment closely agrees with the external shear direction.*

Table 3.10: *Convergence (κ), shear (γ) and magnification (μ) shown by the potential (SIE+γ) at the location of each lens plane image in COSMOS 5921+0638. The last column shows the flux ratio of each image with respect to image B inferred with the magnification values μ.*

Image	κ	γ	μ	Fl. Ratio (/B)
A	0.687	0.742	40.7	0.62
B	0.742	0.737	66.1	1.00
C	0.726	0.689	31.8	0.48
D	0.795	0.767	14.9	0.23

3.6.3 Mass-to-light ratio

Theoretical mass modeling has delivered an accurate estimate for the total mass enclosed within the Einstein ring. Using the observed angular Einstein ring (i.e., θ_E=0.71″) we also measure the amount of light enclosed in it by doing aperture photometry. This is done on the GALFIT de Vaucouleurs profiles fitted, to avoid the contribution from the lensed images.

We obtained an ACS F814W aperture magnitude of 20.88 for the lensing galaxy. Using a k-correction of 0.45 for an elliptical galaxy at redshift z=0.551 in the F814W filter and an absolute magnitude for the sun of $M_{\odot_{F814W}}$=4.53 (see http://www.ucolick.org/∼cnaw/sun.html), we obtain L_{F814W}=$4.26\times10^{10}L_{\odot_{F814W}}$. This, together with the enclosed mass ($1.2\times10^{11}M_{\odot}$, see Section 6.1 and 6.2), leads to a mass-to-light ratio of M/L_{F814W}=$2.7M_{\odot}/L_{\odot_{F814W}}$. The WFPC2 F606W observations yield an aperture magnitude of 22.28 within the Einstein radius. Using a k-correction of 1.33 and an absolute magnitude for the sun of $M_{\odot_{F606W}}$=4.74, we obtain L_{F606W}=$3.33\times10^{10}L_{\odot_{F606W}}$, leading to a mass-to-light ratio of M/L_{F606W}=$3.6M_{\odot}/L_{\odot_{F606W}}$.

Fukugita et al. (1995) show typical rest frame elliptical galaxy colors of B-F814W=2.23 and B-F606W=1.29. We couple these colors with our aperture photometry (F814W and

F606W) data and an absolute magnitude for the sun of M_B=5.33 to obtain luminosities for the lensing galaxy of $L_{B_{F814W}}$=$1.19 \times 10^{10} L_{\odot_B}$ (using the F814W data) and $L_{B_{F606W}}$=$1.75 \times 10^{10} L_{\odot_B}$ (using the F606W data). These lead, respectively, to: $M/L_{B_{F814W}}$=$10.1 M_{\odot}/L_{\odot_B}$ and $M/L_{B_{F606W}}$=$6.9 M_{\odot}/L_{\odot_B}$ which lead to a value of $log_{10}(M/L_B) \approx 0.92 \pm 0.12$. These values are in marginal agreement with those shown by Keeton et al. (1998) for the mass-to-light ratio within the Einstein ring of 10 elliptical lens galaxies.

3.7 Anomalous flux ratios

From the observed flux ratios shown in Table 3.5 we can see that the ratio of brightnesses between images A and B does not vary (within the uncertainties) between the different filters and the different epochs (A/B 2004_F814=0.46±0.03 and A/B 2008_F606=0.39±0.06). However, the flux ratios C/B and D/B show small variations between the different filter and/or over time (C/B 2004_F814=1.06±0.04 and C/B 2008_F606=0.86±0.08; D/B 2004_F814=0.23±0.02 and D/B 2008_F606=0.15±0.04).

Additionally, comparing the theoretical flux ratio values (Table 3.10: A/B=0.62, C/B=0.48 and D/B=0.23) with the observed flux ratios (Table 3.5), a disagreement can be seen. Even more generally, any symmetric model that we choose for the lens potential, expects images A and B to be the brightest images, as they are the merging images of the lensing system and, consequently, the highest magnification images. However, this is not the observed case, as image C is as bright as image B and brighter than image A in the ACS observations.

Several phenomena can explain the flux differences between the images in different filters and in different epochs, and their comparison with theoretical expectations, such as: galactic extinction, substructure, intrinsic variability of the background source or microlensing:

- Galactic extinction: Galactic extinction is a static phenomenon (in human time scales) in which dust in the lensing galaxy absorbs the blue light coming from the background source images. This makes that lensed images located behind different column densities of dust appear with color perturbations, in particular, those behind a bigger dust column density would appear redder. For this particular system, we obtain F606W-F814W colors of: 0.33, 0.19, 0.42 and 0.69 for images A, B, C and D, respectively. Under the galactic extinction interpretation, there would be less dust accumulated over the projection of the lensing galaxy in the location of image B than in the others. While this is a valid interpretation, the four images of the background source lie on a ring around the lensing galaxy, therefore, unlikely to have very different dust densities unless a gradient in the dust distribution is present. It is important to remark that the F606W-F814W color values are calculated with observations at different epochs, thus prone to be affected by different temporal phenomena as the ones discussed hereafter.

- Mass substructure: Much like galactic extinction, mass substructure can produce a static anomalies in the measured flux ratios. A galaxy with mass substructure (of the order of $\sim 10^7$; $\sim 10^9 M_{\odot}$) -i.e.: non-symmetrical luminous or dark matter components or even unseen satellite galaxies- might modify the lensing potential, particularly the flux ratios (Kochanek & Dalal 2004). In the case of COSMOS 5921+0638, even though quite small, the non-parametric model of the lens shows a non symmetric part of the distribution which might be a hint for substructure in the lens. If this is indeed the case, additional observations should display no variations with respect to the present data set.

- Intrinsic variability: AGNs vary their brightness during periods of weeks, days and even hours (Wagner et al. 1990), usually becoming bluer as they become brighter: Unfortunately, as stated before, the observations, even though taken in different filters, are also taken in different epochs, giving a lot of freedom in the interpretation of the chromatic effect. As the AGN images are separated between each other by time-delays (of the orders of hours to half a week, according to the mass modeling), the intrinsic variation of the AGN should be in time scales smaller than these to see the anomalously bright image C, brighter than the close pair A and B. This very short time scale variation would then make very unlikely the fact that after 4 years we observe slightly different flux ratios but the same overall tendency in brightness order.

- Microlensing: Microlensing is also a temporal phenomenon in "macro"-lensed AGNs. In this case, stars in the lensing galaxy produce an additional (de)magnification on the source images. Due to the projected location of the background source images in the lensing galaxy, microlensing in this system is expected. Much like intrinsic variability, (de)magnification by microlensing, in the general case, produces a blue excess: the blue emission from the background source comes from a smaller region, therefore, getting more effectively magnified than the outer regions. As before, the fact that the observations in different bands are taken in different epochs, no strong conclusions can be made from the chromatic point of view. The main difference with intrinsic variability, is that microlensing has no correlation between the multiple AGN images. The projected velocities of the stars in the lensing galaxy and the background source set the microlensing time scales to the order of months to decades, compatible with the observed variations. Under this interpretation, and considering that the measured flux in image C is larger than expected, the flux anomaly that we observe in image C is either due to: (i) microlensing magnification of the flux from this image, mainly during the observations from 2004, (ii) magnification of image B during the 2008 observations or (iii) a combination of both. As the four lensed images are located in region with similar optical depth, variations in the brightness of all images should be seen in time.

3.8 Summary and Conclusions

In this chapter we have presented a detailed study of the gravitationally lensed system candidate COSMOS 5921+0638 discovered in the COSMOS field (Faure et al. 2008). Using part of the COSMOS observations plus additional HST-WFPC2 and VLT-FORS1 observations, we have obtained astrometrical, photometrical and morphological parameters for the objects in the field. With the FORS1 observations we have obtained the redshift of 10 galaxies in the field of COSMOS 5921+0638, including the central galaxy of the system at z=0.551±0.001. Using different criteria and the available observations, we conclude that this galaxy is lensing a background AGN and its host galaxy located at a tentative redshift z=3.14±0.05.

An environmental analysis using the zCOSMOS optical group catalog, does not reveal a strong influence from galaxy groups in the line-of-sight to the system. This result can, however, be sensitive to incompleteness in the catalog.

We have investigated the mass profile of the lensing system and its environment via strong lens modeling, both non-parametric and parametric. Both kinds of modeling agree in the requirement of a small external shear (γ=0.058) in order to produce the configuration of the images. Not explained by perturbation due to galaxy groups from the zCOSMOS optical group catalog, the requirement for this external shear may be due to substructure in

the lensing galaxy or the contribution from individual field galaxies close to the lens. The modeling shows time-delays of the order of hours to days for the different images and a total magnification of $\mu \approx 150$. Comparing the observed brightness of the images with this magnification induced by the fitted mass profile, reveals the low luminosity nature of the background AGN with intrinsic brightness $M \sim$-17.5. The inferred mass-to-light ratio of the lensing galaxy within the Einstein ring is of $log_{10}(M/L_B) \approx 0.92 \pm 0.12$.

Flux anomalies are observed in the different lensed images. With the available dataset, it is not possible to certify a unique reason for these variations. Mainly due to the fact that the observations we have for this system that allow accurate photometry for the point-like images are on different bands and on different epochs. This does not allow to distinguish if the phenomenon is dynamic or static. With this in mind, our preferred explanations for these incompatibilities are microlensing and/or substructure in the lens, with microlensing in general being the most natural explanation for flux ratio anomalies in the optical range.

By doing follow-up observations of this system, the phenomenon or phenomena responsible for these anomalies could be found and quantified. Multi-band photometry of the system at a single epoch would allow to measure the color of the different images free of possible temporal anomalies. Additionally, by repeated multi-band observations on different epochs the possible temporal flux variations could be proven and quantified. If active microlensing is present in this system, the additional resolution power brought by microlensing could reveal interesting properties of the background source, such as measurements of its internal structure (see Chapter 5). If the anomaly is static, a measure of possible substructure in this lens can be accomplished.

The small separations and the low brightness of the images of the background AGN in COSMOS 5921+0638, makes it an ideal candidate for additional space-based and/or new generation optics ground based follow up observations to address the open issues and understand the nature of the background AGN. The lensing induced magnification of the faint high redshift background AGN in COSMOS 5921+0638, allows to study the properties of an object which would have otherwise been undetected in the COSMOS field. Even though Low Luminosity AGNs (LLAGNs) are expected to be far more common than high luminosity AGNs, few of these objects have been observed beyond the local Universe.

4

Integral Field Spectroscopy of Four Lensed Quasar Systems: Analysis of their Neighborhood and Evidence for Microlensing

In the previous chapter we have coupled observational evidence with theoretical concepts in order to assess the lens nature of a candidate strong lensing system. In this chapter, we take advantage of advanced spectroscopic observational equipment to analyze and study the observational properties of confirmed lensed quasar systems. Besides the environment and the main lensing galaxies of the systems, these observations allow us to analyze in depth the flux anomalies between multiple images and the intrinsic emission properties of four background sources. A condensed version of the work presented in this chapter has been published in A&A (Anguita et al. 2008a).

4.1 Introduction

We have already characterized a lensing system by analyzing the observations available. Most of the study shown previously, was done in order to understand the lens and its potential. We have shown that it can be important to understand the internal and environmental properties of the system. Lensing galaxies, in general, do not provide a smooth potential, but are subject to different internal and external anisotropies. External perturbations are due to clusters, groups and individual galaxies around the line-of-sight towards the lensing systems. Internal perturbations, on the other hand, may come from dark and bright matter substructure, dust and even individual stars in the lensing galaxy. External perturbations can modify the positions, as well as the brightnesses of the images of lensed source quasars, whereas internal perturbations mostly modify the relative fluxes and colors of the multiple images (note that substructure can be responsible for modifying both).

Spectroscopy allows a more detailed analysis of the flux and flux anomalies in gravitationally lensed quasars, without the need of a comparison with expectations from theoretical

models. It allows to measure the location of objects in the line-of-sight (absorption features), as well as the intrinsic emission characteristics of the bright background source.

We have used the integral field spectroscopy mode of the VIsible Multi Object Spectrograph (VIMOS) installed at the ESO/VLT-UT2 telescope at cerro Paranal (Chile) to obtain 3D spectroscopy of the fields around four gravitationally lensed quasar systems: HE 0230-2130, RX J0911+0551, H 1413+117 and B 1359+154. This program was conducted at ESO during period 74 (proposal IDs: 074.A-0152(A) and 074.A-0152(B), PI: C. Faure) and was intended to study the close environment of these systems, as well as the spectra of the background quasars.

The four targets are briefly introduced in Section 4.2. The VIMOS Integral Field Unit (IFU) and the dataset are presented in Section 4.3. The reduction of the dataset obtained with VIMOS in its high, medium and low resolution modes is described in Section 4.4. The extraction and identification of the spectra from the different objects in the field of each lensing system, together with their analysis, are reported upon in Section 4.5. Finally, flux ratio anomalies observed in three of the quasar systems are presented and discussed in Section 4.6.

4.2 The targets

The lensed quasar targets were selected based on the fact that the presence of a galaxy cluster/group was either known or suspected in the line-of-sight to them. Furthermore, in RX J0911+0551 and H 1413+117, microlensing activity was suspected (Bade et al. 1997; Angonin et al. 1990).

4.2.1 The quadruple quasar HE 0230-2130

The quadruple lensed quasar HE 0230-2130 was discovered by Wisotzki et al. (1999) in the course of the Hamburg/ESO survey (Wisotzki et al. 1996). The quasar is at redshift z=2.16. The separation between the four quasar images ranges from Δ_{AB}=0.74″ to Δ_{AD}=2.1″. A galaxy over-density was discovered 40″ south-west of the quasar images (Faure et al. 2004). Eigenbrod et al. (2006) identified the redshift of the two main lensing galaxies that lie between the quasar images respectively at z_{LG1}=0.523±0.001 and z_{LG2}=0.526±0.002. A detailed image of the components of the system is displayed in top left panel of Figure 4.1.

4.2.2 The quadruple quasar RX J0911+0551

The quasar RX J0911+0551, was originally selected from the ROSAT All-Sky Survey (RASS; Bade et al. 1995). It was classified by Bade et al. (1997) as a multiply imaged quasar with at least three images at redshift z=2.80. In an analysis with higher resolution imaging from the Nordic Optical Telescope (NOT, La Palma) observations, Burud et al. (1998) discovered a fourth image of the quasar. The lensed quasar is described as three very close images (A1, A2 and A3, with Δ_{A1A2}=0.48″, Δ_{A1A3}=0.96″) and an isolated fourth image (B) located Δ_{A1B}=3.05″ west of image A1. The lensing system comprises an elongated lensing galaxy located at Δ_{A1G}=0.86″ and a galaxy cluster centered at a distance of 38″ from the quasar images. The redshift of the lensing galaxy was measured from Keck observations: z_l=0.769 (see Kneib et al. 2000). Kneib et al. (2000) characterized the galaxy cluster located south-west of the quasar images at z=0.769±0.002, based on the spectroscopic measurements of 24 galaxy members. The measured velocity dispersion of the galaxy cluster is of: $\sigma=836^{+180}_{-200}$ km s^{-1}.

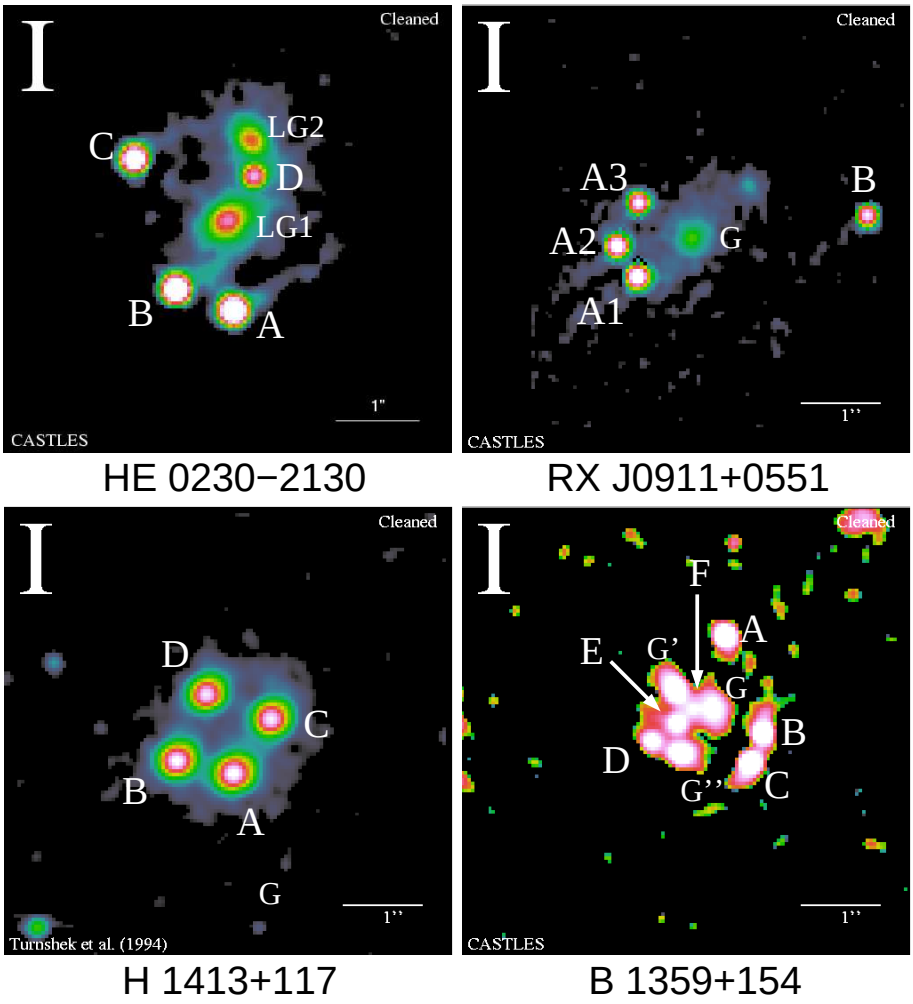

Figure 4.1: *HST F814W images of the four lensed quasars and their lensing galaxies. Left to right, top to bottom: HE 0230-2130, RX J0911+0551, H 1413+117 and B 1359+154. All images except that of H 1413+117 (WFPC2 observations Turnshek 1994) were obtained as part of the CASTLES survey with the NICMOS instrument (Muñoz et al. 1998). All images extracted from the CASTLES website: http://cfa-www.harvard.edu/castles/.*

A detailed image of the components of the system is displayed in top right panel of Figure 4.1.

4.2.3 The quadruple quasar H 1413+117

The quadruply imaged quasar H 1413+117 was first identified as a gravitationally lensed quasar by Magain et al. (1988). It is one of the rare multiply imaged Broad Absorption Line (BAL) quasars. The quasar is at a redshift z=2.55, while the spectroscopic redshift of the lensing galaxy is still unknown. The presence of a galaxy cluster in the direction of the quasar was first suspected by Kneib et al. (1998) and confirmed by Faure et al. (2004), at a photometric redshift z$\sim$0.8$\pm$0.3 (using up to six photometric bands). Additional absorption systems were identified in the BAL quasar spectrum at redshifts z=1.66 and z=1.44 (Magain et al. 1988). A detailed image of the lensed quasar images is displayed in the bottom left panel of Figure 4.1.

4.2.4 The multiple quasar B 1359+154

The lensed quasar B 1359+154 was discovered as part of the CLASS survey and discussed by Myers et al. (1999). The quasar is at redshift z=3.24 and has a maximum image separation of 1.7″. As identified by Rusin et al. (2001), this system shows at least six images of a radio source and its star forming host galaxy. The main share of the lensing potential is produced by three lensing galaxies (G, G' and G" in Figure 4.1) inside the Einstein ring with currently no spectroscopic redshift available; however, the three galaxies have been identified as the core of a galaxy group possibly at redshift z$\simeq$1 based on optical colors and mass estimates derived from models of the system (Rusin et al. 2001). A detailed image of the components of the system is displayed in the bottom right panel of Figure 4.1.

4.3 The VIMOS dataset

This set of observations was collected in service mode between October 2004 and March 2005. The data were taken with the Integral Field Unit (IFU) using the low, medium and high spectral resolution modes.

4.3.1 The VIMOS Integral Field Unit

A schematic representation of the VIMOS Integral Field Unit (IFU) is displayed in Figure 4.2 (extracted from Zanichelli et al. 2005). The IFU head consists of 6400 fibers coupled to microlenses[1], divided into four quadrants. Each quadrant is made of four sub-sets of 400 fibers corresponding to 20×20 pixels areas (A, B, C and D in Figure 4.2) which are, again, subdivided into 5 modules of 20×4 pixels (1 to 5 from the figure). Each quadrant (40×40 pixels) has a mask associated which has four "pseudo-slits" (A, B, C, D) that are fed with the corresponding 20×20 pixels sub-set (A, B, C, D). The 80 fibers inside each of the 5 modules composing these subsets are aligned in the pseudo-slit (top-right panel in Figure 4.2) and the five modules are stacked together (bottom-right panel from Figure 4.2).

The instrument can work in three resolution modes: low resolution (LR, spectral resolution: 210-260, dispersion: 5.3 Å pix^{-1}), medium resolution (MR, spectral resolution: 580-720, dispersion: 2.5 Å pix^{-1}) and high resolution (HR, spectral resolution: 2500-3100, dispersion:

[1]Optical micro-lenses, not to be confused with gravitational microlenses.

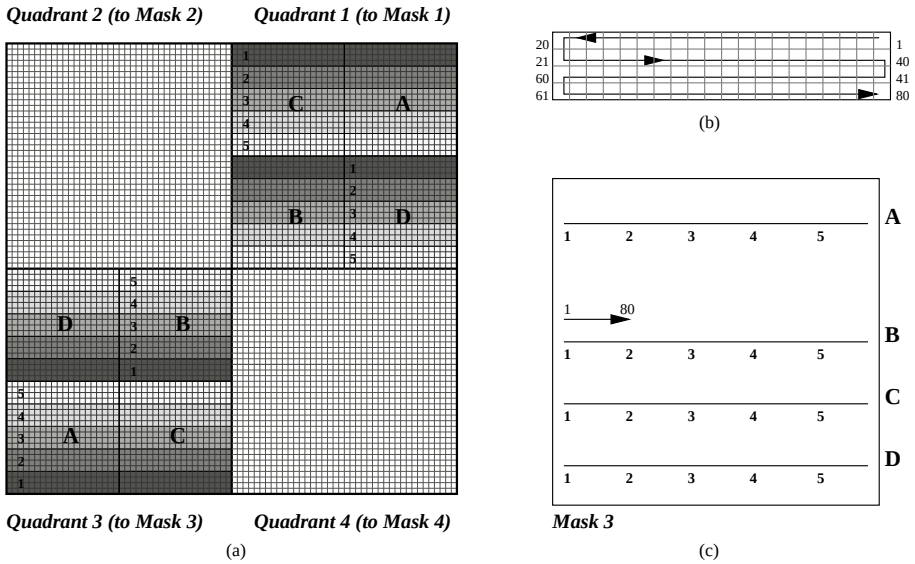

Figure 4.2: *Schematic representation of the VIMOS IFU: (a) The 80×80 micro-lenses coupled to fibers divided into four quadrants, divided into four sub-sets of 20×20 pixels: A, B, C and D (for clarity, shown only for quadrants 1 and 3). These sub-sets feed the four "pseudo-slits" on the IFU masks (c) in the VIMOS focal plane (shown for quadrant 3). Each 20×20 pixels sub-set is in turn divided into 5 modules of 80 fibers each. The fibers in each module are aligned onto the pseudo-slits, following a line by line reading as can be seen in (b). These modules are aligned in the pseudo-slit as displayed in (c). Figure extracted from Zanichelli et al. (2005).*

0.6Å pix^{-1}). In the LR mode all fibers are used, whereas in the MR and HR modes only one pseudo-slit is used per quadrant (sub-sets and pseudo-slits B from Figure 4.2). Therefore, the size of the field-of-view depends on the spatial sampling. We have selected the sampling so as to cover a $27''\times27''$ field size ($0.33''$/fiber in LR and $0.67''$/fiber in MR/HR). The targets were observed through the LR-blue, MR and/or HR-red/orange grisms[2].

We have coupled the LR-blue grism with the OS-blue filter to cover a wavelength range of λ: 3700-6700Å. The MR- and HR-red grism observations were coupled with the GG475 filter to cover a wavelength range of λ: 5000-10000Å and λ: 6350-8600Å respectively, while the HR-orange grism was coupled with the GG435 filter to cover a wavelength range of λ: 5250-7550Å.

4.3.2 Observing runs

A summary of the observing runs used for this analysis is displayed in Table 4.1. For RX J0911+0551 and HE 0230-2130 we have retained only the exposures conducted under a seeing below $1.1''$ and an airmass less than 1.7. For H 1413+117 and B 1359+154 we have considered the observations including at least three quadrants and obtained with an airmass below 1.7, as well. This represents total exposure times of 7 ks in LR and 11 ks in HR for HE 0230-2130, of 7 ks in LR and 9 ks in HR for RX J0911+0551, of 7 ks in LR and 9 ks in MR for H 1413+117 and of 11 ks in MR for B 1359+154.

4.4 Data reduction

The data reduction has been performed mainly using the VIMOS Interactive Pipeline & Graphical Interface (VIPGI: Scodeggio et al. 2005; Zanichelli et al. 2005). While most information concerning the data processing can be retrieved from the VIPGI Cookbook (Garilli et al. 2007) and some important issues are discussed in Covone et al. (2006), we find it necessary to provide additional details on some of the most complex reduction steps in order to make the VIMOS IFU data reduction more transparent for future VIPGI users. A flowchart of the reduction procedure is displayed in Figure 4.3 (extracted from Zanichelli et al. 2005).

4.4.1 First adjustments

The location of the object spectra and the wavelength calibration both require an accurate description of the instrumental distortions. The pattern of these distortions is provided in the data header. However, the instrument flexures change with the pointing direction and, therefore, these values can only be used as "first guesses" for a further improvement by polynomial fits. The VIPGI software offers the opportunity to tailor these first guesses separately for each frame in the observation run.

During this step, individual fibers can be flagged as "dead" if necessary (i.e. zero fiber transmission/efficiency). The flagged fibers will not be considered in any of the subsequent fittings. If the flagging is not made properly, it yields a distorted image of the astronomical object, as illustrated for example in Figure 4.4. A quality control routine allows us to check the adjustments in the different science exposures. The corrected first guesses are then applied to the entire scientific and calibration dataset.

[2]For HR, the observations through quadrants 1, 2 and 3 were obtained with the red filter, while there was no red grism for quadrant 4. Here we used the orange grism instead, see VIMOS Handbook 30 June 2005.

Table 4.1: *Observation log (all observations performed between October 2004 and March 2005).*

Object	Mode	Night	FWHM ″	Air Mass	Exp sec
HE 0230-2130	LR Blue	Nov. 17	0.60	1.24	2355
		Nov. 17	0.58	1.50	2355
		Dec. 5	1.08	1.02	2355
HE 0230-2130	HR Red	Oct. 16	0.60	1.18	2205
		Oct. 16	0.72	1.07	2205
		Oct. 16	0.87	1.02	2205
		Oct. 16	0.61	1.09	2205
		Nov. 13	0.54	1.24	2205
RX J0911+0551	LR Blue	Dec. 8	0.58	1.28	2355
		Dec. 9	0.67	1.31	2355
		Dec. 15	0.83	1.29	2355
RX J0911+0551	HR Red	Dec. 5	0.47	1.25	2205
		Dec. 5	0.46	1.41	2205
		Dec. 10	0.52	1.24	2205
		Dec. 10	0.50	1.40	2205
H 1413+117	LR Blue	Mar. 18	1.27	1.25	2355
		Mar. 18	1.13	1.26	2355
		Mar. 18	1.21	1.64	2355
H 1413+117	MR Orange	Mar .17	0.83	1.24	2205
		Mar. 17	1.22	1.29	2205
		Mar. 17	1.03	1.42	2205
		Mar.17	1.12	1.68	2205
B 1359+154	MR Orange	Feb .13	1.40	1.24	2205
		Mar. 4	0.81	1.33	2205
		Mar. 15	0.59	1.30	2205
		Mar.15	0.39	1.33	2205
		Mar.16	0.88	1.38	2205

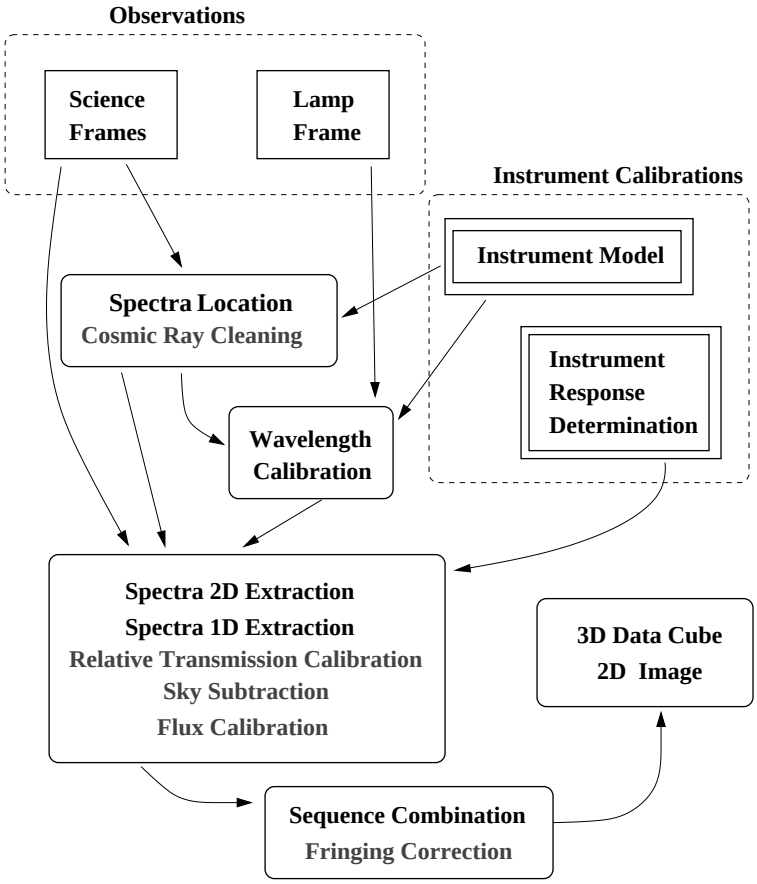

Figure 4.3: *Flowchart of the different reduction steps in* VIPGI. *Optional steps are displayed in gray. Figure extracted from Zanichelli et al. (2005).*

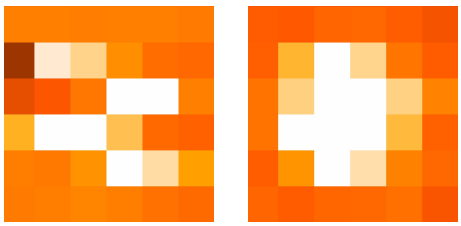

Figure 4.4: *Resulting images of a point-like object in the HR mode for incorrect (left panel) and correct (right panel) flagging of the fibers. In the left panel dead fibers have not been flagged, hence during the first guess adjustment, the software assigns to these fibers the flux of the adjacent one.*

In the second quadrant of the LR mode, the first 80 fibers were flagged as dead because of their low transmission in all frames.

4.4.2 Spectra tracing and extraction

After the first guess correction, one needs to trace the spectra in the different exposures. To do so, we use a high signal flat field exposure obtained immediately after the science exposure. In the LR mode, we use the global fit parameters proposed in the image headers, as they allow a good tracing; for the pixel binning we use 20 pixels to trace the spectra from their start to their end. For the MR/HR frames, better results are obtained ignoring the global fit distortion model, thus, the IFU binning then needs to be larger than 20 pixels (the best fit was obtained for $\sim$50 pixels). From this fit, a table of spectra positions is built. The position table has to be visually inspected to check whether the spectra are correctly traced.

The inverse dispersion solution is calculated next in the "create master lamp" routine. This is done by fitting a third order polynomial to the lamp frame, starting from the first guesses. The inverse dispersion solution was checked visually over the raw frames as well as through the distribution of the Root Mean Square (RMS) residuals of the fit. The RMS residuals are of about 0.7Å$\pm$0.7Å for the LR frames and 0.09Å$\pm$0.06Å for the MR/HR frames.

Independently, the science frames are corrected by a master-bias and over-scan trimming. Then, the object spectra are extracted from the science exposures. At this stage, cosmic rays are detected and eliminated and the wavelength calibration is applied.

4.4.3 Last calibration and exposure combination

The final phase of the reduction process includes many steps. First, the software applies a fiber-to-fiber correction in which the transmission of each fiber is calibrated. This fiber-to-fiber correction is calculated using a bright and isolated sky-line present in all fibers. The transmission is corrected so that each fiber has the same flux all along the sky-line. To perform this correction we have selected the 5577Å sky-line in LR-blue, MR and HR-orange and the 6300Å sky-line in HR-red.

The sky contribution is dealt with in a statistical way (Scodeggio et al. 2005) by subtracting the mode spectrum in each pseudo-slit. This gives satisfactory results if at least 50% of the fibers in the frames relate to pure sky, which is the case for the current dataset. The spectro-photometric calibration of the science frames was made using the observation of standard stars, which accurately corrects for the relative flux.

The information available in the science frame headers concerning the position of the pointing for our data is not accurate enough to be used as a guide for combining the dithered exposures. Therefore, we have computed the shifts between the different exposures using the brightest objects in the frame. This is a delicate step because of a Point Spread Function (PSF) shape problem which is discussed in Section 4.4.4.

Then, the different exposures are combined using a median filter to eliminate the dead pixels and remaining cosmic rays. The resulting product is a datacube: for each pixel within the $27'' \times 27''$ region of the sky, a spectrum is available (see Figure 4.5 for a sketch of the cube). During this combination, a fringing correction may be applied.

The datacube is then corrected for differential atmospheric refraction. Applying a theoretical differential atmospheric refraction correction was attempted, but it did not give satisfactory results. Instead, we have computed and applied an empirical differential atmospheric correction: in most cases, the quasars are very bright in the datacube, so we have been able

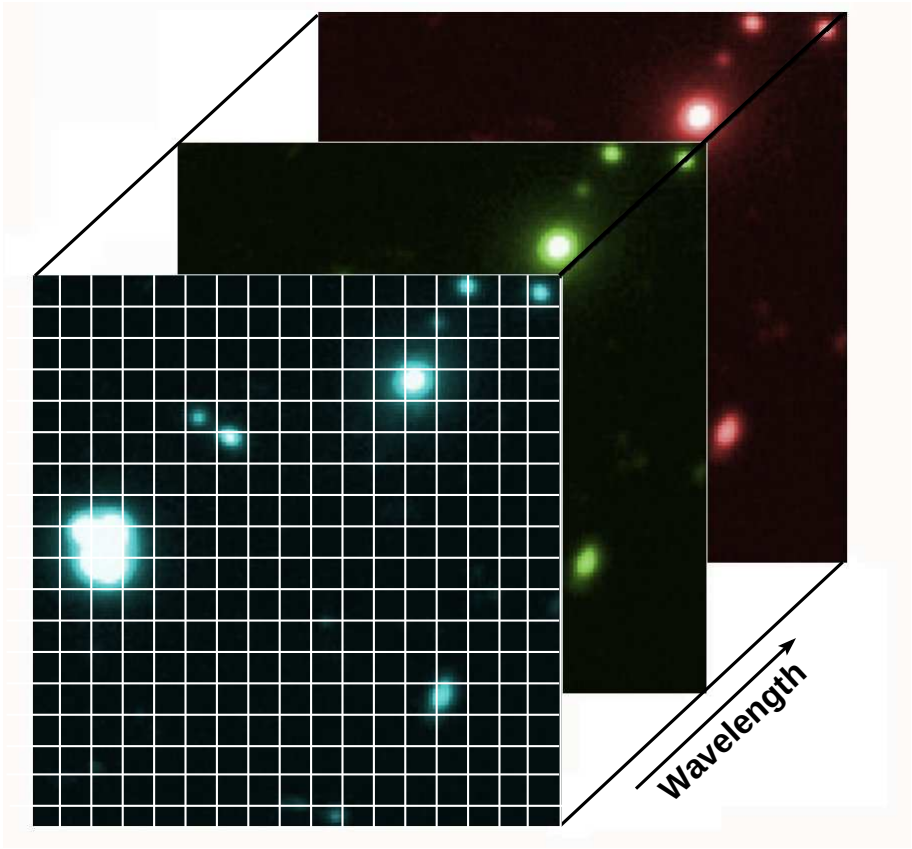

Figure 4.5: *Sketch of the final IFU datacube. Each pixel on the front face of the cube contains a spectrum with wavelength dispersion as indicated in the figure.*

to fit a polynomial to the highest flux position of the quasar image for each wavelength. Then the position correction to be applied to each wavelength cut of the datacube was known.

Images of the fields around HE 0230-2130, RX J0911+0551 and H 1413+117 are shown in Figures 4.6, 4.7 and 4.8. The images were created by adding all the monochromatic slices in the datacube, excluding those corresponding to strong sky emission lines and the edges of the grisms. In the case of B 1359+154 we only have MR observations with one missing quadrant and low signal-to-noise ratio (S/N∼4), hence we could not create such an image.

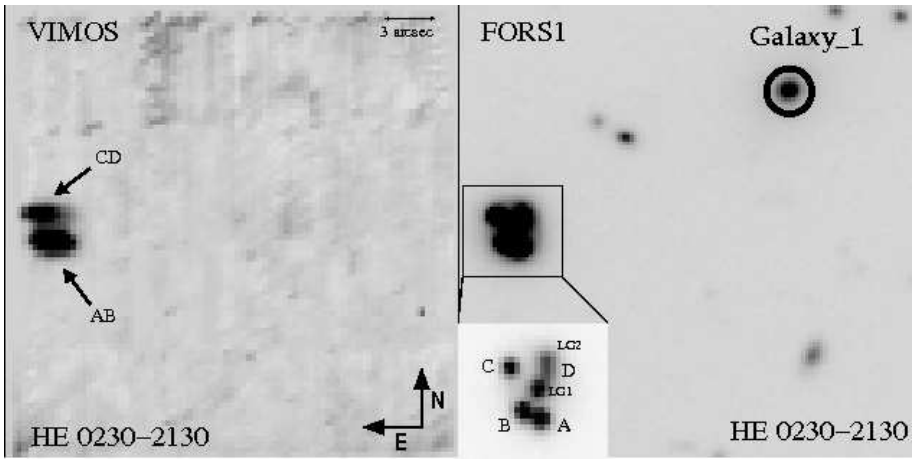

Figure 4.6: *The 27″×27″ field-of-view around the multiple quasar HE 0230-2130: VIMOS IFU LR data cube (left panel) and FORS1 R band image (right panel). The components of the system are labeled as in the text. Orientation and scale are identical in the left and right panels. A FORS1 R band zoom of the system is displayed in the bottom left hand corner of the right panel.*

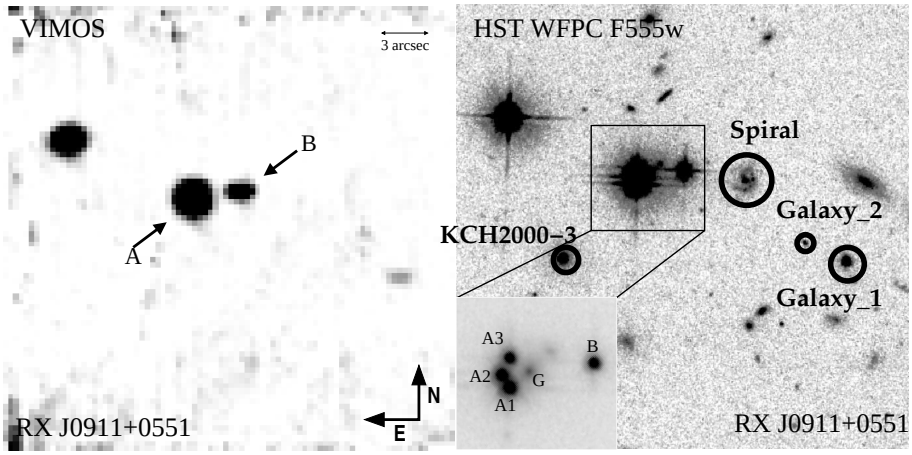

Figure 4.7: *The 27″×27″ field-of-view around the multiple quasar RX J0911+0551: VIMOS IFU LR data (left panel) and WFPC F555W band image (right panel). The components of the system are labeled as in the text. Orientation and scale are identical in the left and right panels. A WFPC F814W band zoom of the system is displayed in the bottom left hand corner of the right panel.*

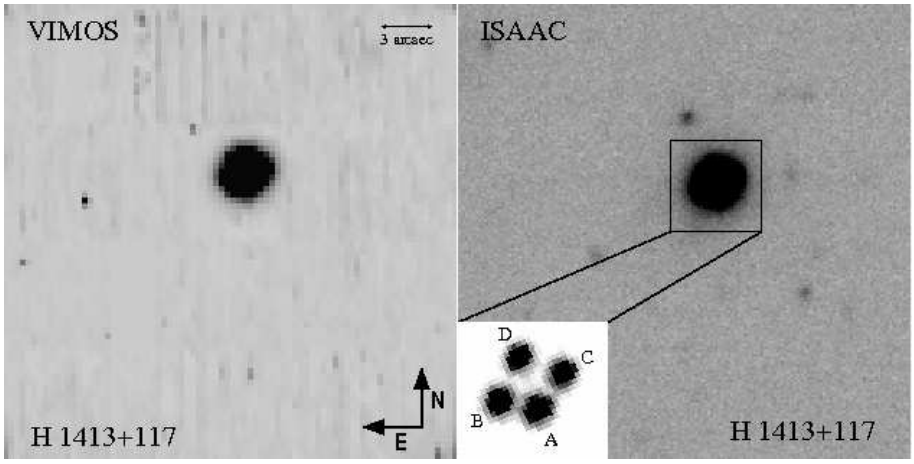

Figure 4.8: *The 27″×27″ field-of-view around the multiple quasar H 1413+117: VIMOS IFU LR data (left panel) and ISAAC J band image (right panel). The components of the system are labeled as in the text. Orientation and scale are identical in the left and right panels. A WFPC F814W band zoom of the system is displayed in the bottom left hand corner of the right panel.*

4.4.4 An additional PSF problem with VIMOS

After the reduction steps and the corresponding checks described above, the PSF in the science target and standard star datacubes still appeared elongated along the east-west direction for all individual exposures. We could not find any VIMOS documentation reporting on this problem; however, it has been confirmed by ESO staff (private communication) that, as the IFU head is placed at the edge of the VIMOS field-of-view, the image of a point source is subject to an aberration and appears slightly elongated in one direction (see for example image B of RX J0911+0551 in the left panel of Figure 4.7). Besides the time investment in understanding the reason for the elongation, it is very difficult to quantify how much this issue impairs the image resolution in the datacubes, as it is a combination of other effects as well (seeing, signal-to-noise and dithering).

However, and as shown hereafter, it is still possible to extract relevant spatial information from the data.

4.5 Identification of the quasar and galaxy spectra

A number of tools were used to visualize and analyze VIMOS datacubes. We used mainly the Euro3D software (Sánchez 2005, http://www.aip.de/Euro3D) that allows us to inspect the datacube, both in an interactive and automated manner (guidance on the use of the software can be found in the Euro3D documentation).

We have used existing deep images of the target field-of-views to identify and locate objects that are faint in the VIMOS rebuilt images (27″×27″). We have used VLT/FORS1 R band data to locate objects in the field around HE 0230-2130, HST/WFPC-F555W and F814W for RX J0911+0551 and HST/WFPC-I814W, ISAAC J and ISAAC K for H 1413+117 (HST program PIs, respectively: J. Hjorth and A. Westphal and VLT program PI: F. Courbin).

The objects for which we have detected a signal are shown and labeled in Figures 4.6,

4.7 and 4.8 for HE 0230-2130, RX J0911+0551 and H 1413+117, respectively. For redshift analysis we use the EZ[3] software coupled with spectral templates (Kinney et al. 1996), plus IRAF routines. We provide below a detailed analysis of the different spectra.

4.5.1 The field of HE 0230-2130

The quasar spectra

The spectra of the quasar images have a very high signal-to-noise ratio (S/N∼40 in the continuum). However, because of PSF shape problems and of the small angular separation between the quasar images, it is not possible to separate all the spectra of the different quasar images. We have partitioned the images in two groups, A+B (from now on AB) and C+D (from now on CD), which are visually resolved in the final datacube (see Figures 4.1 and 4.6 for labels). Based on the Lyman α(1215Å) + NV(1240Å), SiIV+OIV](1398Å), CIV(1550Å) and CIII](1908Å) emission lines, the spectra from both AB and CD provide a source redshift z=2.163±0.003, in agreement with Wisotzki et al. (1999). In the two spectra an absorption system is detected at the same redshift of the quasar, likely originating from the quasar's host galaxy. No other obvious absorption systems are detected in the spectra (see Figure 4.9).

Galaxies in the field around HE 0230-2130

We have extracted spectra at the location of the main lensing galaxies (LG1 and LG2 as shown in Figures 4.1 and 4.6) that are highly contaminated by quasar emission. Therefore, a scaled version of the spectrum of the isolated quasar image C has been subtracted. Doing so, we are able to detect absorption lines from both lensing galaxies. We measure the redshift of LG1 at z=0.521±0.004 and of LG2 at z=0.524±0.003. These redshifts are in agreement with those obtained by Eigenbrod et al. (2006) ($z_{\rm LG1}$=0.523±0.001; $z_{\rm LG2}$=0.526±0.002).

Another galaxy is seen in the field, north-west of the quasar image A ($\Delta\alpha$=-15″, $\Delta\delta$=9.2″, Galaxy_1 in Figure 4.6). Its spectrum shows the CaII K, CaII H and G-band absorption lines, and also the [OIII] and [OII] emission lines (see Figure 4.10). From these lines we measure a redshift of z=0.518±0.002, thus, this galaxy is probably a member of the group or cluster to which the lensing galaxies LG1 and LG2 belong.

4.5.2 The field of RX J0911+0551

The quasar spectra

Much like with the previous system, due to the small separations between images A1, A2 and A3 ($\Delta_{\rm A1A2}$=0.48″, $\Delta_{\rm A1A3}$=0.96″, $\Delta_{\rm A2A3}$=0.61″) and the distorted shape of the PSF, it was not possible to separate the spectra of the three quasar images. Therefore, they are treated as a single object called A (see Figure 4.7, left panel).

In the LR-blue mode, the A and B quasar spectra exhibit Lyman α+NV+OV], SiIV+OIV] and CIV emission lines at redshift z=2.790±0.009. As already mentioned by Bade et al. (1997), we can also detect several absorption lines in both the A and B spectra; CIV and Lyman α at z=2.42 (or ∼-29,000 km s^{-1} with respect to the quasar), CIV, SiIV, and Lyman α at z=2.63 (or ∼-13,000 km s^{-1} with respect to the quasar), and a few more absorption lines at wavelengths below 4500Å. An absorption line at 5488Å, if identified as CIV, would imply a redshift of z=2.54 (or ∼-22,000 km s^{-1} with respect to the quasar). It might correspond

[3]Redshift analysis software by the authors of VIPGI: http://cosmos.iasf-milano.inaf.it/pandora/EZ.html

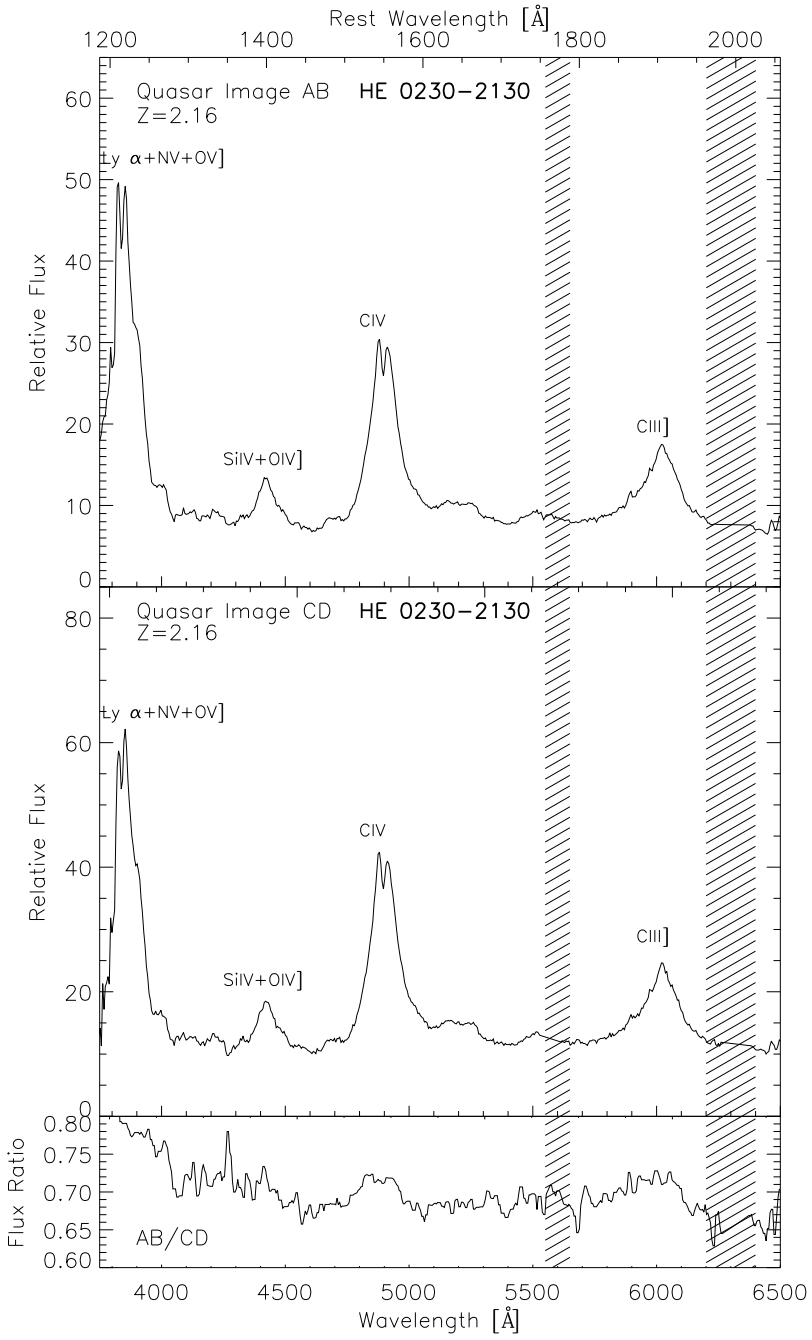

Figure 4.9: *Low resolution spectra of HE 0230-2130. Top panel: combined spectra for images AB. Middle Panel: combined spectra for images CD. Bottom panel: flux ratio between the two spectra. Shaded regions indicate the spectral ranges dominated by intense sky line residuals.*

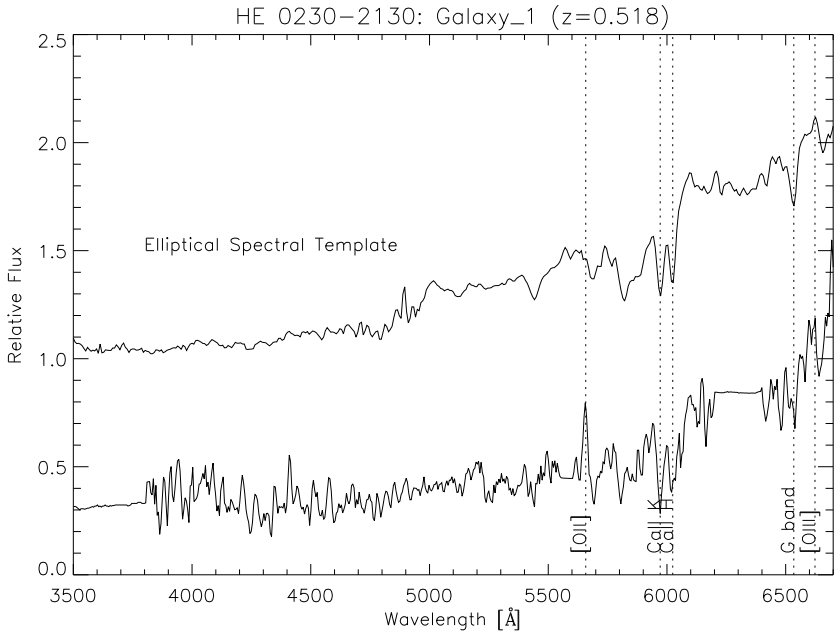

Figure 4.10: *Neighborhood of HE 0230-2130: Low resolution spectrum of the galaxy in the field around HE 0230-2130 (labeled Galaxy_1 in Figure 2) and a scaled version of a template elliptical galaxy spectrum. From the lines shown we measure a redshift of z=0.518±0.002.*

Table 4.2: *Values obtained for the five parameter Gaussian fits of the absorption lines detected in the spectra of RX J0911+0551. An asterisk (*) denotes the lines close to the 5577Å sky line.*

Redshift	Line	Center [Å]	FWHM [Å]	σ [km s^{-1}]
z=2.80	$Ly\alpha$	-	-	-
	C_{IV}	5840.5	15	330
	C_{III}	7185.5	19	340
z=2.63	$Ly\alpha$	4404	30	940
	$C_{IV}*$	5618.5	19	430
	C_{III}	-	-	-
z=2.54	$Ly\alpha$	-	-	-
	$C_{IV}*$	5487.5	28	640
	C_{III}	-	-	-
z=2.45	$Ly\alpha$	4163	29	900
	C_{IV}	-	-	-
	C_{III}	-	-	-

to the line identified by Bade et al. (1997) at 5546Å (z=2.57), although its proximity to the 5577Å intense sky line makes its redshift determination uncertain. The absorption lines have velocity dispersions of $\sigma \leq 1000$ km s^{-1} (see Table 4.2), hence, the quasar was classified as a

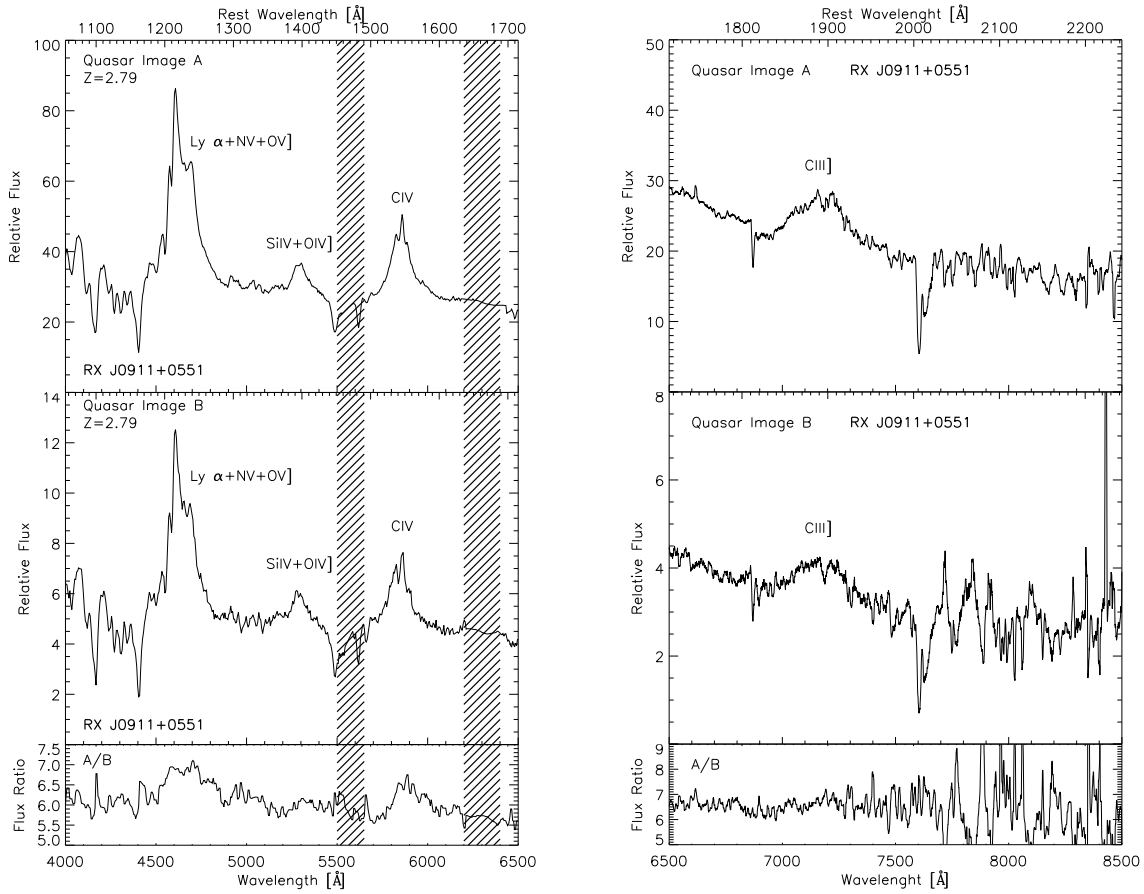

Figure 4.11: *VIMOS IFU spectra of RX J0911+0551. Left panel: low resolution spectra. Right panel: high resolution spectra. Top panels: summed spectrum for image A. Middle panels: spectrum for image B. Bottom panels: flux ratio between the spectra A and B. Shaded regions indicate spectral ranges dominated by sky residuals in the low resolution, whereas everything longwards of 7500Å in the high resolution spectra, is dominated by sky residuals.*

mini-BAL quasar (e.g., Chartas et al. 2001). The physical origin of the absorption lines is still under discussion; the most likely interpretation is that these lines are due to high-velocity outflows related to the quasar central engine (e.g., Reichard et al. 2003).

In the HR-red spectra of the A and B quasar images, we detect the CIII] emission line at the quasar redshift, not seen in the previous spectra of Bade et al. (1997). Thanks to the VIMOS high quality data, we also detect a few absorption features on top of the CIV and CIII] emission lines. Their FWHM are smaller than those of the other absorption lines previously indicated (see Table 4.2). These narrow features could either be produced by outflowing material from the quasar central engine, or signatures of the quasar host galaxy.

In Figure 4.11 the spectra of images A and B are shown in low and high resolution modes respectively, as well as the flux ratios between the spectra. Residuals in the flux ratios are

discussed in Section 4.6.

Galaxies in the field around RX J0911+0551

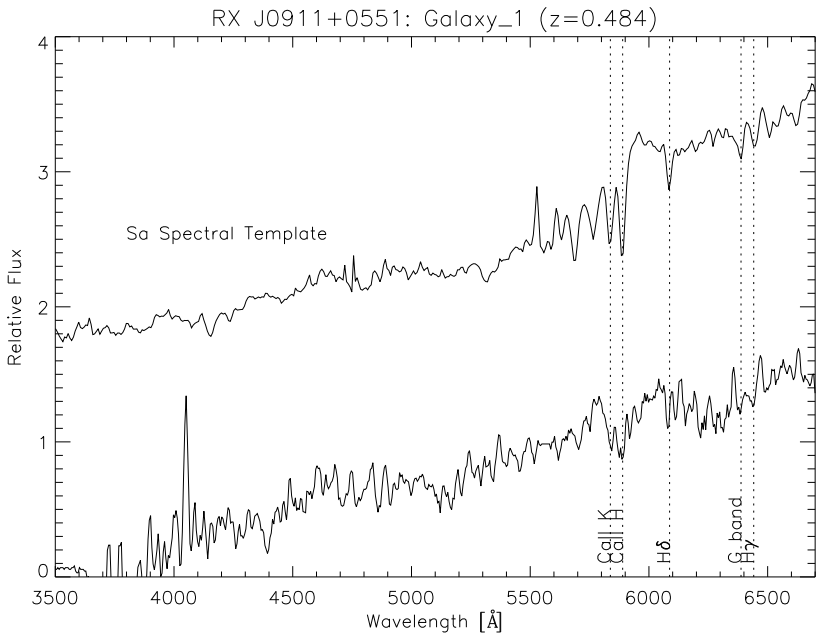

Figure 4.12: *Neighborhood of RX J0911+0551: Spectrum of Galaxy_1 and of an Sa spectral template for comparison. Identified lines are highlighted by dotted straight lines. They yield a redshift z=0.484±0.001.*

We are unable to detect any absorption features from the lensing galaxy because of the intense contribution of the three quasar images. Nevertheless, in the low resolution data we newly identify three objects in the field: Galaxy_1, Galaxy_2 and Spiral as labeled in Figure 4.7. We are only able to confidently measure the redshift of Galaxy_1 for which we obtain a value z=0.484±0.001 (see Figure 4.12), indicating that it is not a member of the cluster found by Kneib et al. (2000) at z=0.769.

In the HR-red mode, we identify the galaxy labeled KCH2000-3 in Figure 4.7, which had been previously detected by Kneib et al. (2000) and measured at z=0.7618. Our determination of the redshift gives z=0.762, in good agreement. This galaxy is part of the galaxy group discovered south-west of the quasar.

4.5.3 The field of H 1413+117

The quasar images cannot be visually resolved in the two dimensional cuts, either in the LR or in the MR spectroscopy. The low and medium resolution summed spectra for all four quasar images show the Lyman α, NV, SiIV emission lines coupled with their broad absorption counterparts and the CIII] line. From the emission lines we measure the quasar redshift at z=2.554±0.002.

The higher spectral resolution and longer wavelength range available in the medium resolution mode allows us to detect the absorption systems already described by Magain et al.

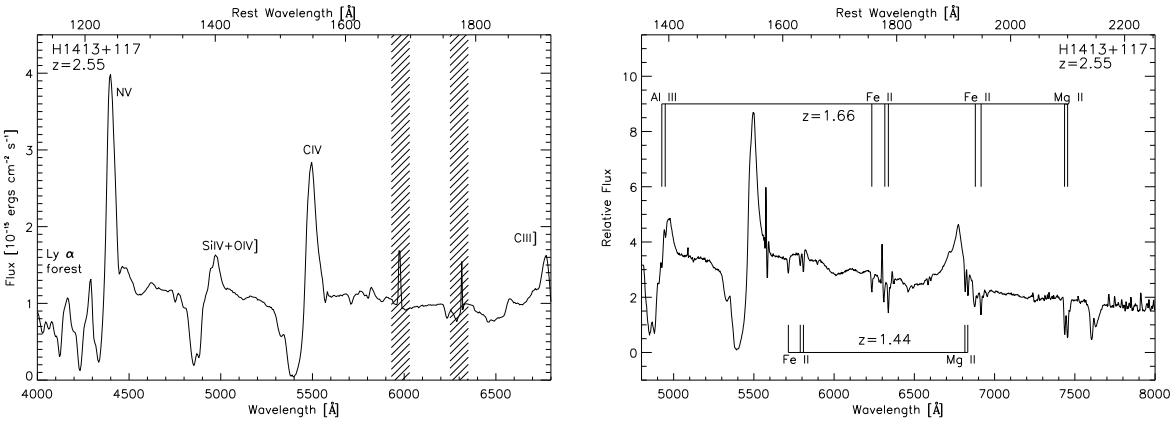

Figure 4.13: *Left panel: LR-blue spectrum of H 1413+117. Right panel: MR-orange spectrum of H 1413+117. Both spectra were reconstructed by adding the contributions from the four quasar images. The dashed areas highlight regions affected by sky subtraction residuals. The lines identified with the z=1.44 and z=1.66 absorption systems are indicated on the medium resolution spectrum. Two other doublet systems are seen at ∼6450Å and ∼6600Å.*

(1988). Taking advantage of the improved resolution and small width of the absorption lines we have been able to obtain very tight values for their redshifts. In the first absorption system, the FeII triplet (∼5750Å) and the MgII doublet (∼6850Å) yield a redshift z=1.4381±0.0002; in the second system, the AlIII doublet (∼4950Å), FeII triplet (∼6300Å), the FeII doublet (∼6900Å) and the MgII doublet (∼7450Å) yield a redshift z=1.657±0.001. Two other doublets are detected at ∼6450Å and ∼6600Å; they do not seem to be related and it is hazardous to assign them a specific identification. Low and mid-resolution spectra are displayed in Figure 4.13.

4.5.4 The field of B 1359+154

For the quasar system B 1359+154 only the MR-mode was used. It being a faint and high redshift quasar, the signal-to-noise ratio is lower than in the other datasets (S/N∼4 in the continuum).

However, we can recover a spectrum of the quasar by summing over the spatial elements in the two dimensional wavelength cuts (spaxels) of the different quasar images. The spectrum (displayed in Figure 4.14) exhibits the Lyman α, NV, SiIV+OIV], CIV and HeII lines, yielding a redshift z=3.235±0.003.

No absorption systems are observed in the spectrum. In addition, no galaxy is detected in the field. As no spectroscopic signature could be recovered from individual images, no further analysis was possible for this quasar.

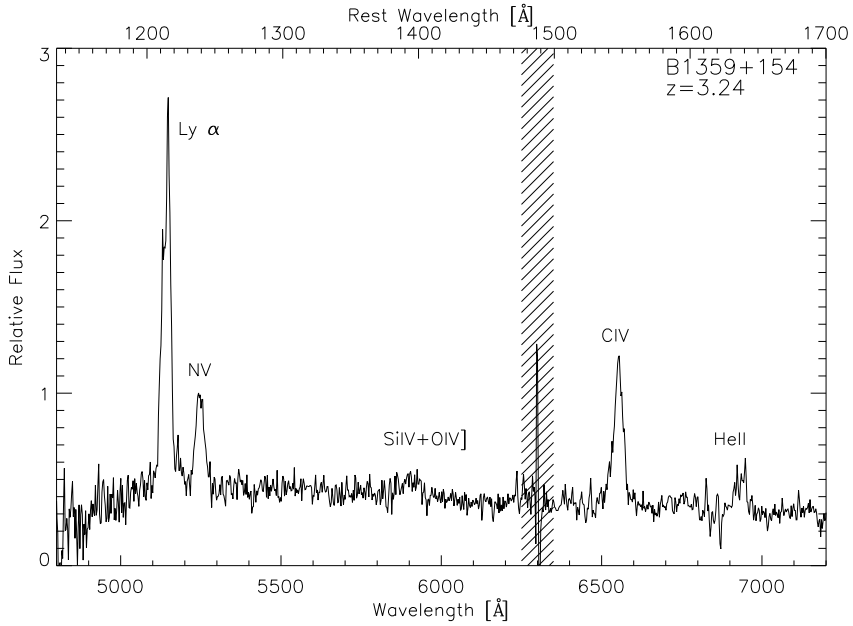

Figure 4.14: *MR-orange spectrum of B 1359+154 (all spaxels with signal have been summed). Shaded areas correspond to regions affected by sky subtraction residuals.*

4.6 Interpretation of the spectral differences between the quasar images

4.6.1 Spectral differences in HE 0230-2130

In order to identify and analyze any differences between the spectra from images AB and CD, we first simply measure the ratio between the two spectra. The ratio varies with wavelength, in particular it is different if measured over the continuum or over the emission lines. Furthermore, a mild slope in the continuum flux ratio is observed. Notice that the edge of the grism (<4000Å) is an un-trustable region and has been dropped in the analysis.

To study this phenomenon further, we developed a specific procedure to extract the spectral energy distribution (SED) of the four individual quasar images: a surface with four Gaussian profiles was fitted to each 2D monochromatic slice of the LR-blue datacube. Distances between the Gaussian centroids correspond to the distances between the quasar images as provided in the CASTLES web page[4], from HST data. A further constraint is that the FWHM (in both directions: x and y) should be identical for the four profiles at each wavelength cut. The fit was performed using Levenberg-Marquardt routines in an iterative fashion (MPFIT, Craig Markwardt[5]). In Figure 4.15 we show the extracted spectra for images A and D of HE 0230-2130, while their ratio is displayed in Figures 4.16 and 4.17. The spectra of the isolated images A and D display emission line differences as well as a mild continuum slope difference. This is not surprising as image D of the quasar is located almost behind the lensing galaxies: LG1 and LG2 (Figures 4.1 and 4.6), therefore, it is prone to be affected by individual stars and interstellar matter in them. Indeed, the flux ratios between images A

[4]http://cfa-www.harvard.edu/castles/
[5]http://cow.physics.wisc.edu/∼craigm/idl/

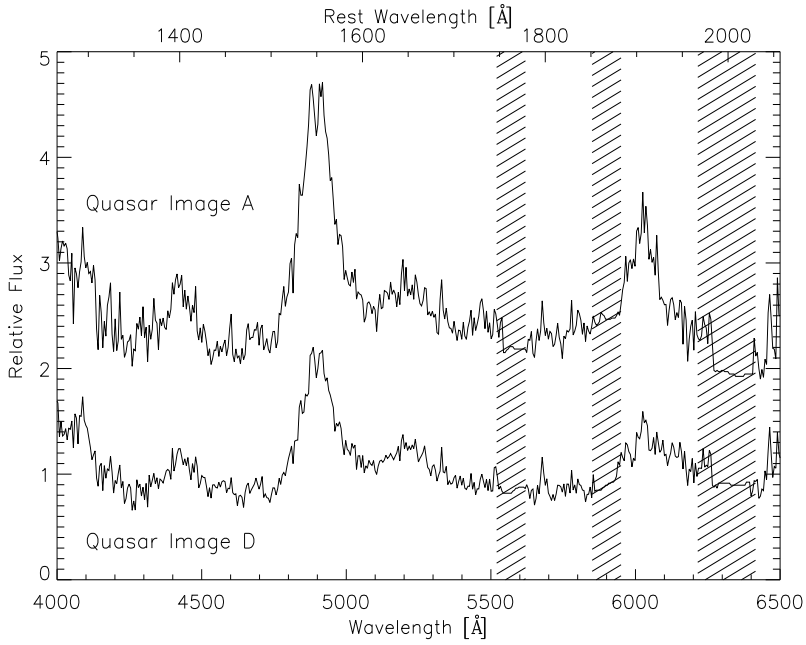

Figure 4.15: *Spectra of the individual images A and D of HE 0230-2130. The normalized spectrum for each image is displayed. The spectrum for image A has been shifted upwards by 1.5 flux units for comparison. Shaded areas highlight regions affected by sky subtraction residuals.*

and B and between images A and C (not shown here) show little or no variation above the noise, contrary to image D.

Intrinsic quasar variability is a possible, but unlikely, explanation for this phenomenon. Indeed, images A and D are separated by a time-delay and, therefore, any intrinsic variation of the quasar flux would be reflected at different epochs in images A and D. However, intrinsic variability of the quasar itself would more likely show selective emission line differences rather than similar magnification in all the emission lines. Indeed, different lines being emitted from different regions in the quasar are not likely to vary at the same time (Kaspi et al. 2000). Hence a more plausible explanation for the emission line differences is microlensing by stars in the lensing galaxy, affecting preferentially image D of the quasar.

Microlensing is expected to affect the continuum emission more strongly than the broad line emission because the continuum emitting region is thought to have a size comparable to those of the Einstein rings of stellar microlenses, whereas the broad line region is much larger (e.g., Schneider & Wambsganss 1990; Abajas et al. 2002). To demonstrate this: based on the virial theorem, the size of the broad line region ($R_{\rm BLR}$) is estimated to be (Peterson et al. 1998):

$$R_{\rm BLR} = 0.57{\rm pc}\left(\frac{v_{\rm FWHM}}{10^3{\rm km\ s^{-1}}}\right)^{-2}\left(\frac{M_{\rm BH}}{10^8 M_\odot}\right) \tag{4.1}$$

where $v_{\rm FWHM}$ is the velocity derived from the FWHM of an emission line and $M_{\rm BH}$ is the black hole mass. Assuming a reasonable size for the continuum emitting region ($R_{\rm cont}$) of

1,000 Schwarzschild radii (r_s), we get:

$$R_{\rm cont} = 9.1 \times 10^{-3} {\rm pc} \left(\frac{M_{\rm BH}}{10^8 M_\odot} \right). \tag{4.2}$$

It is obvious that $R_{\rm cont} \ll R_{\rm BLR}$, independently of the black hole mass. In this case, the continuum of image D could be magnified by microlensing, making the emission lines "sink" in the continuum and, therefore, making them appear small in comparison to the emission lines of image A.

Could microlensing also explain the slope difference (chromatic effect) seen between the two images A and D? Accretion disk models predict that continuum emission from the central part is bluer than that from the outer part (Shakura & Sunyaev 1973). In general, the innermost part of an accretion disk (blue-emitting) is more strongly affected by microlensing than the outer part (red-emitting) as the Einstein ring of microlenses matches better the size of the inner accretion disk (e.g., Wambsganss & Paczynski 1991; Yonehara et al. 1998). Therefore, to first order and in a naive vision, an image affected by microlensing should exhibit a bluer continuum. In image D, the situation is reversed: the quasar image thought to be affected by microlensing (image D) appears redder than the image not affected by microlensing (image A). Let us examine how this could happen.

In Figure 4.16 we illustrate how microlensing can change the slope of the flux ratio between images A and D, by using a simple model for the caustic. We adopt a standard accretion disk model for the continuum emitting region (Shakura & Sunyaev 1973). The black hole mass is set at $10^8 M_\odot$, the accretion rate is set fixed at the critical accretion rate and the inner and outer radii are set at $3r_s$ and $1{,}000r_s$ respectively. Additionally, we assume a single straight line caustic and apply the following approximated formula for magnification (μ) (e.g., Schneider et al. 1992):

$$\begin{aligned} \mu &= \left(\frac{x}{x_{\rm scale}} \right)^{-1/2} + \mu_{\rm a} \quad (x > 0) \\ &= \mu_{\rm a} \quad (x < 0) \end{aligned} \tag{4.3}$$

where $x_{\rm scale}$ is the scale length of the caustic and is chosen to be identical to the Einstein ring radius of a lensing object with mass $1M_\odot$. The parameter μ_a represents the total magnification except for a pair of micro-images which appear/disappear at the caustic crossing. For image A and image D, the μ_a values are arbitrarily set to be 3.0 and 2.0 in order to match the observed continuum flux ratio ($\sim$1.5).

As already seen in Chapter 3, microlensing is not the only possible explanation for the chromatic effect. Galactic dust extinction through the lensing galaxy is also an alternative. In this case, galactic dust would block the blue light from image D, making it look redder in comparison to image A, and resulting in a decreasing flux ratio towards the redder part of the spectrum, as observed between images A and D. We evaluate the chromatic feature which is to be expected from differential dust extinction (e.g., Jean & Surdej 1998). For these calculations, we consider a normal extinction law, R_V=3.1, for dust in the Milky Way (Cardelli et al. 1989) and an extinction law as in the Small Magellanic Cloud (Gordon et al. 2003). In both cases, we assume a local gas-to-dust ratio (Bohlin et al. 1978) $A_V = 5.3 \times 10^{-22} N_H$, where A_V and N_H are, respectively, the dust extinction in the V band (in magnitudes) and the column density of hydrogen gas in cm^{-2}. We also assume that the difference in the gas column density in front of the images is 5×10^{20}cm^{-2} in the case of the Milky Way, and is 5×10^{21}cm^{-2} in the

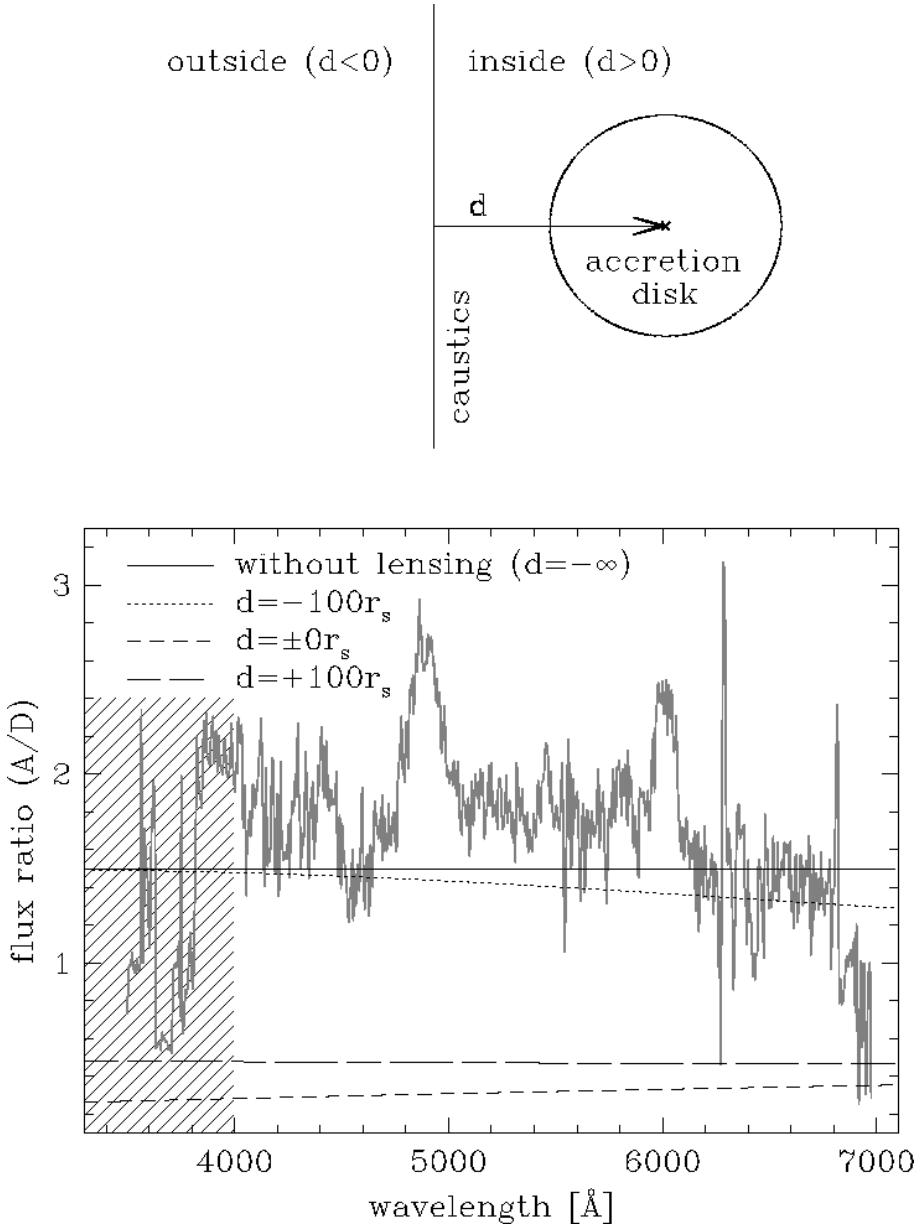

Figure 4.16: *Simple microlensing model for HE 0230-2130. Top panel: Schematic of the straight line caustic with respect to the source. d is the distance measured between the center of the source and the caustic. Bottom figure: flux ratio between HE 0230-2130 images A and D. Superimposed on the flux ratio observed curve, the straight lines are the modeled flux ratios in different situations, that is for different distances d. The solid line is the modeled flux ratio without microlensing (i.e. d=∞). The dotted, the dashed, and the long-dashed lines correspond, respectively, to the modeled flux ratios with microlensing for distances between the caustic and the source center as described in the legend. The shaded area denotes the blue extremum of the grism (un-trustable region).*

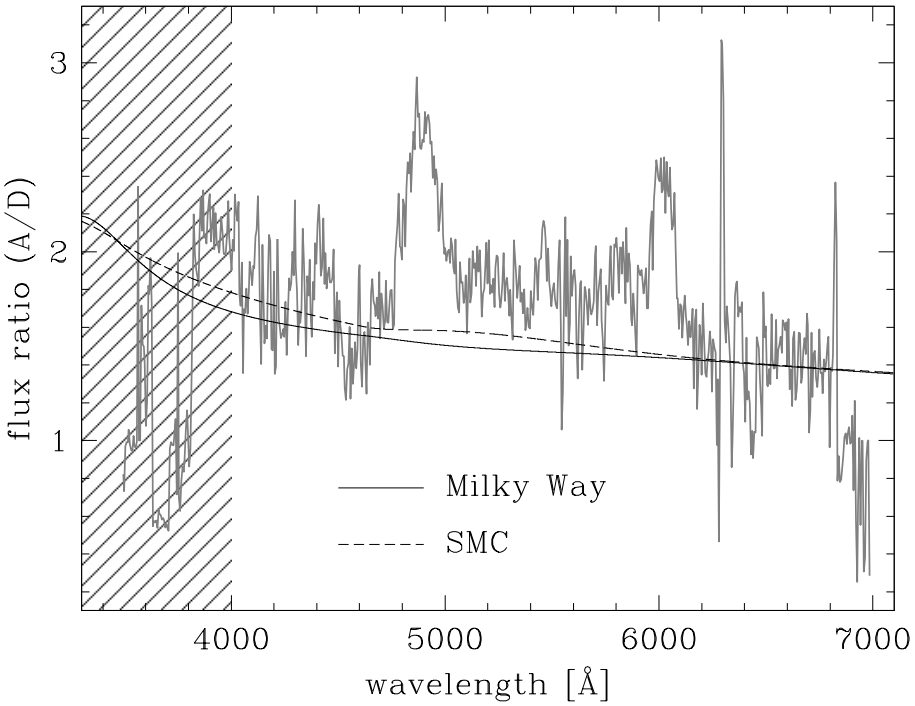

Figure 4.17: *A normal extinction law, R_V=3.1, for dust in the Milky Way (solid line) and an extinction law as in the Small Magellanic Cloud (dotted line) on top of the flux ratio between images A and D of HE 0230-2130. The shaded area denotes the blue extremum of the grism (un-trustable region).*

case of Small Magellanic Cloud. Figure 4.17 shows the extinction expected from these two models. Both of them seem to trace at least part of the slope that we see in the continuum flux ratio, therefore, galactic extinction is a plausible explanation for the phenomenon.

In conclusion, in the case of HE 0230-2130, our preferred interpretation for the difference between the spectra of images A and D is microlensing due to the lensing galaxies LG1 and LG2 affecting image D. It explains both the emission line dimming and the continuum reddening in the spectrum of image D. However, this is not the only interpretation: in particular the effect of the interstellar matter and dust in the lensing galaxies should not be overlooked.

4.6.2 Spectral differences in RX J0911+0551

The different images of quasar RX J0911+0551 also exhibit spectral flux differences. However due to the small separation of the images, it is impossible to apply the same extraction procedure as for HE 0230-2130. In order to quantify the differences between the spectra, we have performed Gaussian profile fits to the three main emission lines in the LR-blue wavelength range. Using the continuum levels obtained from the Gaussian fits, we have derived the equivalent widths (EW) of the emission lines, and considered them as a measure of their strength. This was performed using:

$$EW = \int_{\lambda_1}^{\lambda_2} \frac{(S(\lambda) - I)}{I} d\lambda \tag{4.4}$$

where $S(\lambda)$ is the flux at wavelength λ and I is the continuum level for the chosen wavelength range (in this case the range of the emission lines, delimited by λ_1 and λ_2). The parameters are displayed in Table 4.3.

Table 4.3: *Parameters of the Gaussian fits for the emission lines in the system RX J0911+0551: amplitude and continuum level are expressed in* 10^{-15} *erg* s^{-1}*, position centers, Gaussian* σ *and equivalent widths in Å. The equivalent widths are measured in the rest frame.*

LINE	$Ly\alpha$		Si_{IV}		C_{IV}	
IMAGE	A	B	A	B	A	B
Amplitude	4.42	0.59	0.72	0.10	1.86	0.24
λ_{Cent} [Å]	4639	4636	5292	5287	5853	5843
σ [Å]	75.95	73.69	33.03	31.63	55.61	59.35
Continuum	2.85	0.47	2.94	0.50	2.70	0.46
EW [Å]	81.83	63.69	5.43	4.50	24.93	20.13

The differences between images A and B are confirmed by looking at the equivalent width values which are systematically larger in image A. While the continuum ratio is around 5.9, the emission line ratio goes up to 7.7. Emission line residuals are seen in the flux ratio between images A and B, but in contrast to HE 0230-2130, the emission lines appear to be stronger in the image that is closer to the lensing galaxies. As argued in Section 4.6.1, we think that microlensing is the most probable explanation for the emission line residuals, but in this case, given the distances of the images to the lensing galaxy, we would rather be dealing with microlensing de-magnification in the image complex A.

To test this interpretation, we have built a "macro" lens model for RX J0911+0551, using an elliptical effective lensing potential (Blandford & Kochanek 1987) with external shear.

Using this lens model, we have evaluated the effective shear (γ_{eff}) and the convergence (${\kappa_\star}^{eff}$) on all the images of the quasar, in order to characterize the properties of the time-delay surface (e.g., Blandford & Narayan 1986): minima, maxima or saddle points. The results are shown in Figure 4.18. Since images A1 and A3 are located at saddle points, they are more likely to be de-magnified by microlensing (Schechter & Wambsganss 2002), therefore, it is quite plausible that the continuum emitting region of image complex A (A1, A2, A3) is overall de-magnified.

Of course, the effective shear and convergence depend on the convergence provided by a smooth distribution of matter (κ_c) and a clumpy stellar component ($\kappa_\star$) in the following way:

$$\begin{aligned} \kappa_\star^{eff} &= \frac{\kappa_\star}{1 - \kappa_c} \\ \gamma_{eff} &= \frac{\gamma}{1 - \kappa_c} \end{aligned} \tag{4.5}$$

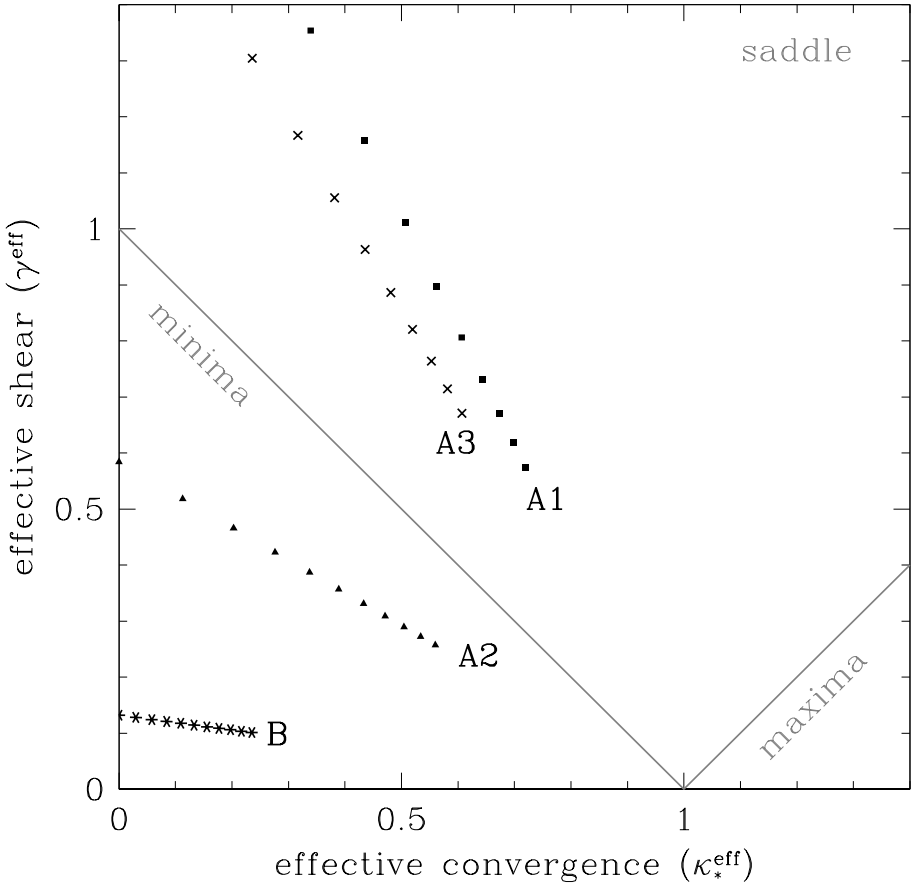

Figure 4.18: *Results of a simple lens model for RX J0911+0551: Different values for the effective shear versus effective convergence. The symbols correspond to different images of the quasar: black squares: A1, black triangles: A2, crosses: A3 and stars: B. From left to right, the contribution of κ_c to $\kappa_\star$ varies from 100% to 0%. All combinations place the images A1 and A3 in the zone of saddle points.*

However, the quasar images A1 and A3 lie at saddle points, no matter which fraction of κ_c and $\kappa_\star$ is incorporated in the lens model (see Figure 4.18).

Regarding the slope of the continuum flux ratio for RX J0911+0551, a mild tilt is also observed. We have measured the slope of this variation by adjusting a straight line over the whole spectral range (see Figure 4.19). The fit has been adjusted over the continuum ratio which was obtained after subtracting the Gaussian fits of the emission lines from the total flux ratio. We have measured a slope of (-1.75±0.15)$\times 10^{-4}$Å^{-1}. Due to the evidence for microlensing de-magnification, as argued above to explain the emission line residuals, we are led to consider that microlensing is also responsible for the chromatic distortions, making the complex image A appear bluer. However, this measured effect is of small significance and impossible to disentangle from differential extinction with the present dataset.

4.6.3 Spectral differences in H 1413+117

In order to extract an individual spectrum for each image of the quasar we apply the procedure described earlier in Section 4.6.1. As before, owing to the small separation of the images, it

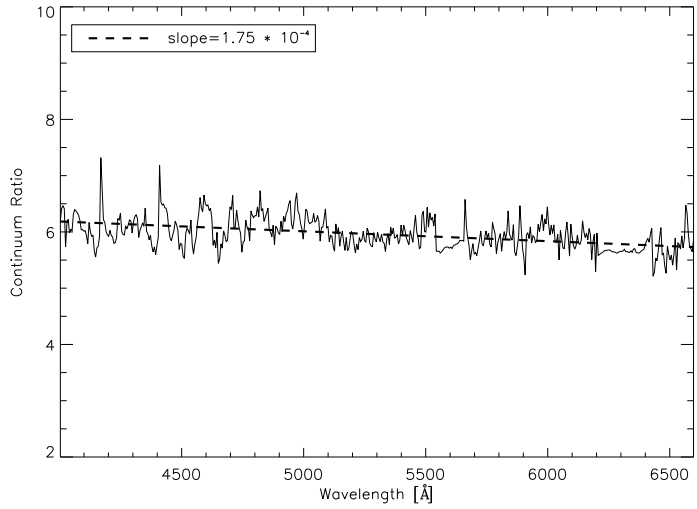

Figure 4.19: *A linear fit to the continuum ratio for the lensing system RX J0911+0551. A mild slope can be seen.*

is possible to do so only with data obtained in the low resolution configuration. The spectra of the four images are displayed in Figure 4.20.

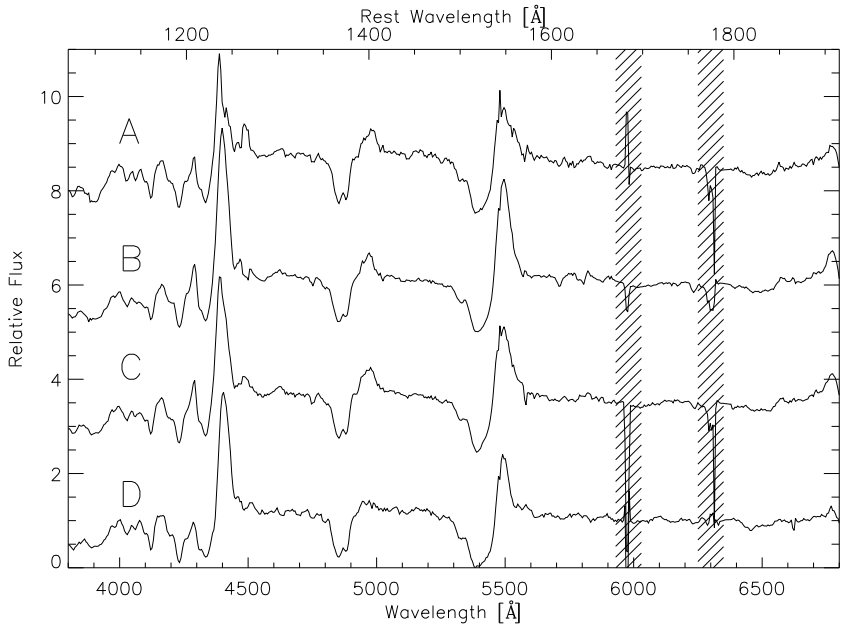

Figure 4.20: *Individual spectra for the four images of the quasar H 1413+117 after the fitting procedure. They have been normalized and shifted vertically for easier comparison (by 2.5 with respect to the bottom one). Shaded areas highlight regions affected by sky residuals.*

We notice some differences between the spectra. The quasar image D exhibits the most

obvious differences when compared to the other images (see also Figure 4.21): the CIV line clearly shows a smaller intensity with respect to the continuum, while the SiIV+OIV] line has practically vanished. This again is consistent with the continuum of image D being magnified by microlensing.

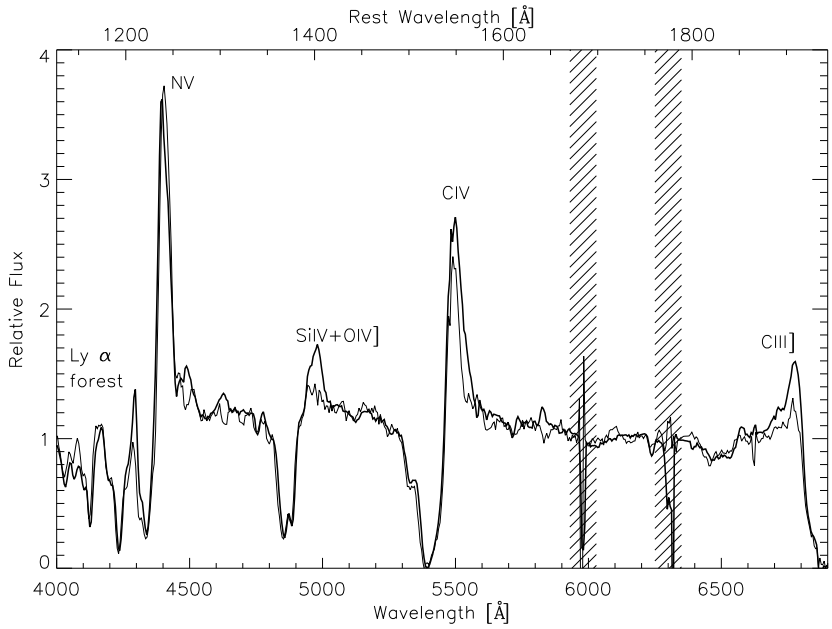

Figure 4.21: *The normalized spectrum of image D of H 1413+117 (thin line) and the mean spectrum of images A, B and C (thick line). Shaded areas show regions affected by sky line residuals. The difference in the relative amplification between the continuum and the emission lines is evident, especially at the SiIV+OIV] and CIV lines.*

Kayser et al. (1990) suggested microlensing as an explanation for photometric variations seen in image D of the quasar. Using integral field spectroscopy observations, Angonin et al. (1990) found spectral differences between image D and the other three images. They suggested that the differences were produced by broad absorption line clouds being selectively magnified by microlensing. A comparison between the present VIMOS spectral dataset and the Angonin et al. (1990) dataset, in particular for image D, shows that the relative spectra have changed: the CIV broad absorption feature 16 years ago was wider in image D than in the other images, whereas it now looks the same, and the SiIV+OIV] emission feature is even smaller in the VIMOS dataset ($\sim$1/3 compared to the average of the other images measured from the continuum) than in the Angonin et al. (1990) dataset ($\sim$1/2 compared to the average of the other images). In addition, there appears to be a slight slope difference in the Angonin et al. (1990) dataset when image D is compared to the other images. However, this difference is not observed in the VIMOS dataset. Again some or all of these features could be explained by three phenomena: galactic extinction, microlensing or intrinsic variability. We comment below upon the evidences against or in favor of such possibilities:

- Galactic extinction: if there is a steeper slope in the continuum of a quasar image when compared to the other images, it can be interpreted as galactic extinction. In the Angonin et al. (1990) dataset, this might be the case with image D, however, no slope

difference can be seen in the VIMOS dataset. As galactic extinction is not expected to vary over time (especially on such a short time scale of 15 years) the slope should have persisted. Furthermore, Turnshek et al. (1997) showed that the reddenings between images B and C, as well as between images A and C were considerably larger than that between images D and C. Finally, differential extinction cannot explain the relative flux differences between the continuum and the emission lines when measured in different images. Therefore, we reject this interpretation.

- Microlensing: the variation of the continuum slope of image D, together with the variation on the relative intensity of the emission lines in all four images (particularly image D) give a clear signal that microlensing is at work and is the best candidate for generating the observed changes. As explained previously, microlensing can explain the chromatic continuum magnification. In this case, the image that suffers magnification of its continuum is also the one that showed a bluer spectrum, which is the most likely kind of chromaticity induced by continuum microlensing. The differences of the broad absorption features seen in Angonin et al. (1990) were interpreted as microlensing from broad absorption clouds. This suggestion has been tested with different microlensing simulations over the years (e.g., Hutsemekers 1993; Hutsemekers et al. 1994; Lewis & Belle 1998), in which the BAL profile of image D was reproducible. These differences are not seen anymore in the VIMOS dataset, which again is a result favoring microlensing in image D, as 15 years is roughly the expected timescale for microlensing variations in H 1413+117 (Hutsemekers 1993). Finally, Ostensen et al. (1997) have shown, from their photometric monitoring between 1987 and 1995, almost parallel light curves for the quasar images, except for image D. Image D exhibits a slightly higher amplitude in its overall variation, which, added to its spectral differences, makes a strong case for additional microlensing affecting image D.

- Intrinsic variability: intrinsic variations of the quasar flux coupled with time-delays between its multiple images would also induce spectral differences between the images. Time-delays for this quasar have not been measured yet. Even though its expected value depends on the model, the symmetric disposition of the images suggests that it should be of the order of a month (e.g., model by Chae & Turnshek 1999). If the timescale of the quasar intrinsic variations is shorter than the time-delay for image D, then the brightness differences could also be explained by this phenomenon and should be seen in all four images at epochs separated by the time-delays.

Although it is not possible to rule out the quasar intrinsic variability as the cause of the spectral differences between the images (without doing a comprehensive and quantitative study based upon regular and precise spectrophotometric monitoring), we find it very likely that the spectral differences seen in H 1413+117 result from microlensing. Microlensing can explain all the feature differences seen in the spectra and is a natural explanation.

4.7 Summary and conclusions

We used the VIMOS-IFU device at the VLT to search for objects in the vicinity of four lensed quasars for which a galaxy group or galaxy cluster was either confirmed or expected as part of the lensing system. Additionally, at least two of these lensed quasars were suspected to be under flux (de)magnification due to microlensing. We have described our data reduction techniques for integral field spectroscopy as an aid for future VIMOS users.

We were able to measure flux ratio differences between the different quasar images in three of the systems: HE 0230-2130, RX J0911+0551 and H 1413+117. Using the high quality spectra collected, our interpretation of the origin of these phenomena is microlensing in the three cases. Based on differences in the flux ratios between the different images when measured in the continuum or the emission lines, we conclude that: HE 0230-2130 is affected by microlensing magnification on the continuum of image D while image A (A1+A2+A3) of RX J0911+0551 is affected by a microlensing de-magnification of the continuum. Finally, image D of H 1413+117 shows a consistent history of having been affected by microlensing over the past 15 years. However, even though less likely as described in Section 4.6.3, these flux ratio differences could also be attributed to intrinsic variability from the quasars coupled with time-delays between the images.

In the three cases, the flux ratios between the quasar images show or have shown a non-zero slope, which is also consistent with microlensing. Nevertheless, in the RX J0911+0551 and HE 0230-2130 systems this phenomenon could also be explained by dust extinction due to the lensing galaxy or, even more likely, a combination of both phenomena. For H 1413+117, if there has been a slope difference between the images in the past, galactic extinction is not a likely explanation as this slope is not seen in the present VIMOS dataset.

If, as we suspect, the three systems are affected by microlensing, future photometric and/or spectroscopic monitoring should fully characterize the phenomenon and allow derivation of the physical properties of the background sources.

We have also detected absorption features from the two main lensing galaxies in the system HE 0230-2130 at z_1=0.521 and z_2=0.523. A third galaxy at similar redshift (z=0.518) has also been detected $\Delta\theta\sim17''$ away from the quasar images. In the field around RX J0911+0551 we have newly identified a galaxy, at a distance $\Delta\theta\sim12''$ from the quasar images, and at redshift z=0.484, which makes it independent of the known galaxy cluster in the line-of-sight to this quasar. Even though not directly bound to the lensing galaxies, its vicinity to the quasar line-of-sight suggests that it might influence the total lensing potential. For H 1413+117 the higher resolution spectra clearly reveal the already known absorption systems at redshifts $\sim$1.44 and $\sim$1.66 with high accuracy.

Unfortunately, due to a combination of low exposure time, intrinsic PSF distortions and non-optimal observing conditions, the quality of the data obtained for B 1359+154 does not reveal any new information on the system or its surroundings.

5

The Quadruple Quasar Q2237+0305 Under a Microlensing Caustic

In the previous chapters we have shown different diagnostic methods to assess which phenomena could be responsible for flux ratio anomalies in lensed quasar systems. In most (if not all) of the cases, microlensing has been the most likely cause. In this chapter we use the microlensing phenomenon as a natural tool to probe the inner structure of a multiple lensed quasar by coupling the microlensing induced dynamic photometric variations of images of the multiple quasar Q 2237+0305 with theoretical microlensing simulations. A condensed version of the work presented in this chapter has been published in A&A (Anguita et al. 2008b).

5.1 Microlensing in Q 2237+0305

Q 2237+0305 is one of the best studied quasar lensing systems yet. This quasar was discovered as part of the Center for Astrophysics (CfA) redshift survey (Huchra et al. 1985). The system is made up of a barred spiral galaxy at a redshift z=0.0394 and four images of a quasar at a redshift z=1.695 that appear in a nearly symmetric configuration around the core of the spiral galaxy, at a distance of approximately $1''$ from the center of the bulge (see Figure 5.1). Due to this particular image disposition, Q 2237+0305 is also referred to as "The Einstein Cross".

Q 2237+0305 is an ideal system to study quasar microlensing. At the position of the quasar images the optical depth due to microlensing by the stars is high ($\sim$1; Kayser et al. 1986; Kayser & Refsdal 1989; Wambsganss et al. 1990). Additionally, the quasar is $\sim$10 times farther from us than the lensing galaxy, leading to a large projected velocity of the stars in the source plane, and thus a short timescale of caustic events. Furthermore, the expected time-delay between the images of this quasar is of the order of a day or less (Schneider et al. 1988; Rix et al. 1992; Wambsganss & Paczynski 1994). As microlensing events for this system are of the order of months or years, it is easy to distinguish intrinsic variability from microlensing. Not long after its discovery in 1985, Irwin et al. (1989) observed the first microlensing signature in the system. The quasar has been intensely monitored for almost two decades by different surveys (e.g., Corrigan et al. 1991; Pen et al. 1993; Ostensen et al. 1996;

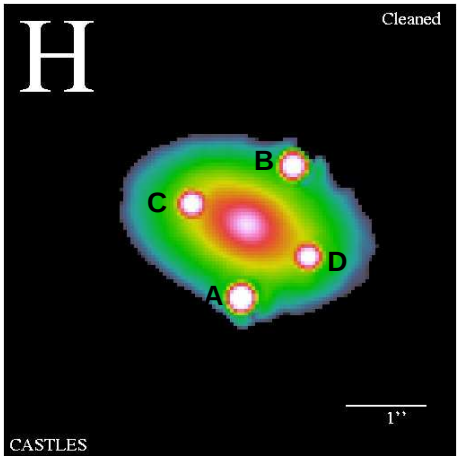

Figure 5.1: *HST NICMOS F160W (H) image of Q 2237+0305. It shows the nearly symmetrical configuration of the quasar images around the core of the spiral galaxy. Image from the CASTLES project (Muñoz et al. 1998).*

Alcalde et al. 2002; Schmidt et al. 2002). The one that has the longest and best sampled data is that of the Optical Gravitational Lensing Experiment (OGLE) team (Woźniak et al. 2000; Udalski et al. 2006). They have monitored Q 2237+0305 since 1997 delivering the most complete light curves in which many microlensing events can be seen (see Figure 5.2). These data have been used for various studies of the system: Wyithe et al. (2000a,b,d,e,f); Yonehara (2001); Shalyapin et al. (2002) and Kochanek (2004) used these data together with microlensing simulations not only to obtain limits on the properties of the quasar such as size and transversal velocity, but also on the mass of the microlensing objects.

The OGLE team has monitored this quasar with a single V band filter. However, Wambsganss & Paczynski (1991) showed that color variations should be seen in quasar microlensing events and how they would provide additional information on the background source. We know from thermal accretion disk models that emission in the central regions of a quasar should be bluer than in the outer regions (e.g., Shakura & Sunyaev 1973). As shown previously (Equation 4.2), the size of the continuum emitting region of a quasar can be approximated by:

$$R_{\rm ad} = 1000 \times r_s = 2.8 \times 10^{16} \left(\frac{M_{\rm BH}}{10^8 M_\odot} \right) {\rm cm} \tag{5.1}$$

where r_s is the Schwarzschild radius, $R_{\rm ad}$ is the radius of the accretion disk and $M_{\rm BH}$ is the mass of the black hole. As shown in Section 2.3.4, we can compare this value with the Einstein Radius (R_E) produced by stars in the lensing galaxy -the magnification length scale used in lensing (see Section 2.3.2)- which is given in the source plane by (Equation 2.41):

$$R_E = \sqrt{\frac{4GM}{c^2} \frac{D_s D_{ls}}{D_l}} = 5.68 \times 10^{16} \sqrt{\frac{M}{0.1 M_\odot}} {\rm cm} \tag{5.2}$$

where we have replaced the values of the distances D_l, D_s and D_{ls} to the specific ones corresponding to Q 2237+0305. The accretion disk scales are thus comparable to those of the Einstein rings of stars in the lensing galaxy. This shows that differential magnification of the different emission regions of the quasar can be observed.

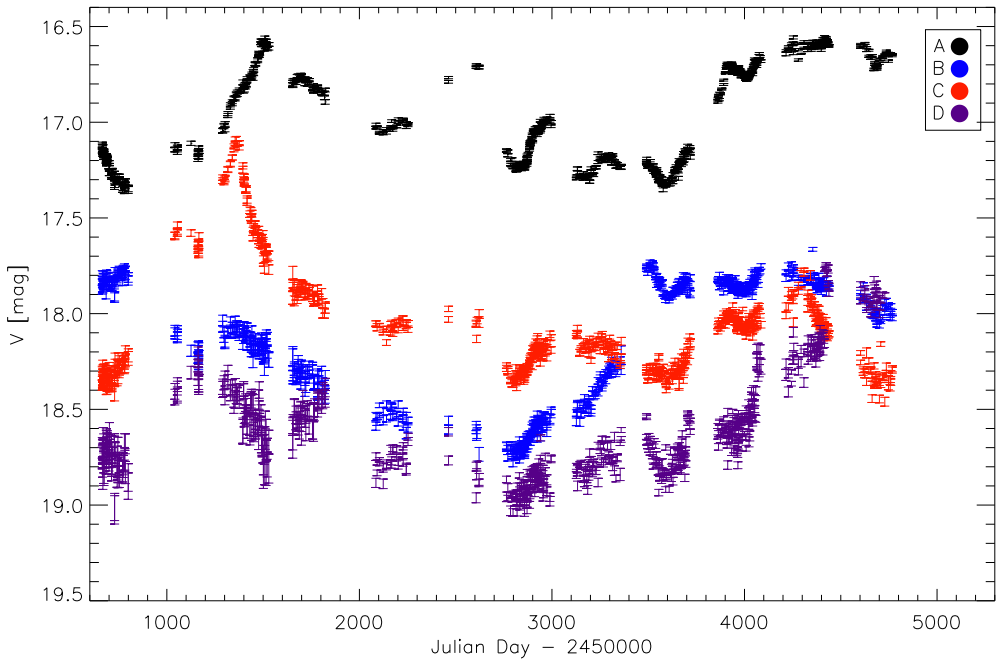

Figure 5.2: *OGLE light curves for the four images of Q 2237+0305 between the years 1997 and 2008. The observed relative brightness variations are due to microlensing by stars in the lensing. Data points from the OGLE campaign (Woźniak et al. 2000; Udalski et al. 2006, + recent (2007, 2008) updates).*

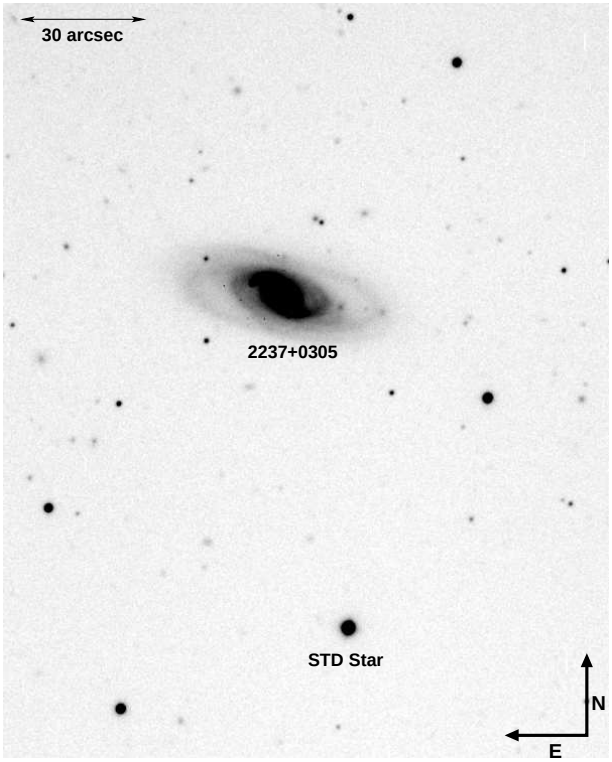

Figure 5.3: *APO g' image of the quasar system Q 2237+0305.*

Some multi-band observations of this system have been carried out (Corrigan et al. 1991; Vakulik et al. 1997, 2004; Koptelova et al. 2005), however, most of them have either large gaps between the observations, or no obvious microlensing events.

A very interesting event, that has been one of the bases for predictions (Wyithe et al. 2000b) and study (Yonehara 2001; Shalyapin et al. 2002; Vakulik et al. 2004), is the high magnification event of image C in the year 1999 as observed by OGLE .

In this chapter we present data of this particular event obtained in two filters at Apache Point Observatory (APO). We analyze the event using both the OGLE light curves and the APO data and study the implications for the size of the quasar emission region using microlensing simulations.

5.2 Apache Point Observatory data, observations & data reduction

For this study we use two different datasets. The first one is that of the OGLE[1] team light curves for this quasar (Woźniak et al. 2000; Udalski et al. 2006), for which we select the data between Julian days 2451290 (April 21, 1999) and 2451539 (December 26, 1999), comprising 83 data points. The result is a dense light curve for the event we analyze. The second data set is APO two-band monitoring data for Q 2237+0305. We selected the nights between May 17 1999 (Julian day: 2451316) and January 8 2000 (Julian day: 2451551) which also track

[1] http://bulge.princeton.edu/∼ogle/ogle2/huchra.html

the event, comprising 8 nights with data points.

The APO data were taken with the 3.5 m telescope at Apache Point Observatory using the Seaver Prototype Imaging camera (SPIcam) in both the SDSS g' and r' filters. The SPIcam has a 2048×2048 pixels CCD and a minimum pixel scale of 0.141″/pixel, however, for the observations we use, the pixels were binned to 0.282″/pixel.

5.2.1 Standard CCD reduction

For the standard CCD reduction we use a combination of the astronomical image reduction software package IRAF and the IDL data language. We apply bias correction, create one master flat-field image for each night and each filter and calibrate the science frames with these. Cosmic rays are eliminated from the science frames using median filtering away from the sources.

In order to remove the remaining cosmic rays and imperfections of the CCD, as well as to improve the signal-to-noise ratio of the images, we combine the frames corresponding to the same night, excluding those with asymmetric point spread functions (PSFs). In the end we obtain a clean high quality image for each night in the g' and r' filters.

5.2.2 Photometry

The photometry for this system is made difficult because the quasar images are seen through the core of the lensing galaxy. Our first attempt, following the procedure as in Woźniak et al. (2000), was to use an image subtraction method (Alard & Lupton 1998). However, our field-of-view lacks the high number of bright stars required in order to run a successful correlation and PSF characterization for the procedure. This is why we use GALFIT (Peng et al. 2002) instead. GALFIT is a galaxy/point source fitting algorithm that fits 2-D parameterized image components directly to the images.

GALFIT model

For the galaxy we use the model shown by Schmidt (1996) (see also Trott & Webster 2002) from HST F7815LP band data, in which the lensing galaxy is parameterized with a de Vaucouleurs profile (de Vaucouleurs 1948) for the bulge and an exponential profile for the disk. The bulge's de Vaucouleurs profile is constrained to a 4.1″ (3.1 kpc) scale length, a 0.31 ellipticity and a 77° position angle (measured from north to east). For the exponential profile we use a 11.3″ (8.6 kpc) scale length, a 0.5 ellipticity and a 77° position angle. These profiles are constrained to have the exact same central position within each frame and a fixed magnitude difference.

The quasar images are parameterized as point sources. The relative separation between them is fixed in the GALFIT code to the values obtained by Blanton et al. (1998) from UV data and the separation between the group of images and the center of the bulge is fixed to the values obtained with HST F7815LP filter data (HST proposal ID 3799): $\Delta\mathrm{RA}_{AG}$=-0.075″and $\Delta\mathrm{DEC}_{AG}$=0.937″.

The PSF we use to convolve the different parameterizations is taken from the bright star (STD) shown in Figure 5.3. After fitting the different profiles, the brightness of each component is measured. We run the GALFIT routine over each night in each one of the two bands available. The residuals from this fitting technique are low, usually of the order of 5 percent (see Figure 5.4). In order to obtain error bars on the magnitude measurements, we create 500 Monte-Carlo realizations of the observed images and determine the measurement

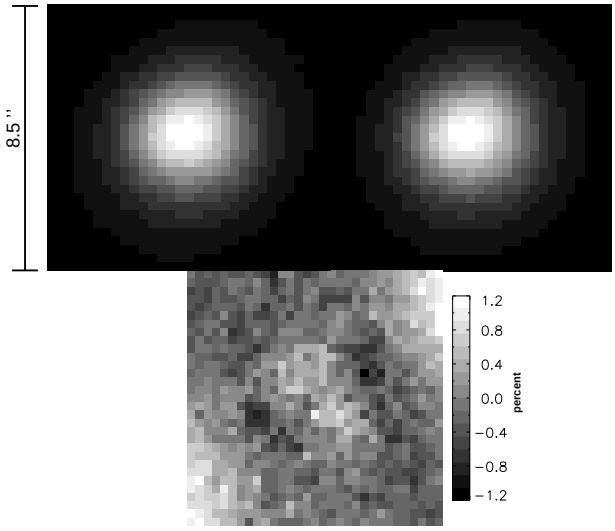

Figure 5.4: GALFIT *fitting procedure over an individual green filter frame of Q 2237+0305. The figures show a zoom into the galactic core. Top left panel: original image from the galaxy core and the four quasar images. Top right panel: best fit model for the galaxy and the quasar images. Bottom panel: rescaled subtraction between original and modeled data. The gray scale shows the percentage in relation with the highest count in the raw image of the system.*

uncertainty from the scatter of the GALFIT results (see Appendix B). The g'- and r'-band light curves for image C are shown in Figure 5.5. The measurements for images A and C are given in Table 5.1. No reliable photometry is obtained for images B and D because they were too faint.

As shown in Figure 5.5, the APO g'-band light curve shows a very similar behavior to the OGLE V-band light curve, however, the APO r'-band light curve shows a lower amplitude at the brightness peak. Thus, the resultant g'-r' color curve, does not appear flat but shows a chromatic variation during the microlensing event.

5.3 Microlensing simulations

In order to compare the observed data with simulations we generate source plane magnification patterns for quasar images C and B using the "inverse ray shooting" method (Wambsganss 1990, 1999).

The method consists in the "shooting" of light rays from the observer's point of view to the lens plane. This lens plane contains a random distribution of microlenses that deflect each individual light ray independently. The deflected light rays are followed onto the source plane, where they are collected in a two-dimensional pixelated plane.

The number of microlenses in the lens plane and the deflection, depend on the local "macro" lensing parameters: convergence (or surface mass density) κ and shear γ of the given image. Furthermore, the surface mass density κ is split into two components we call $\kappa_\star$ and κ_c, which represent the density arising from point-like objects (stars) and smoothly distributed matter, respectively (as shown in Section 4.6.2). Using the lens equation (see Chapter 2), the formal mapping of each ray from the lens to the source plane can thus be

Table 5.1: *APO light curves for quasar images A and C of Q 2237+0305. Magnitudes are shown relative to the value of the last data point of image C in the g' filter.*

Julian Day	A		C		FWHM
-2450000	g' [mag]	r' [mag]	g' [mag]	r' [mag]	[″]
1315	-0.822±0.016	-0.675±0.012	-0.533±0.016	-0.381±0.013	1.6
1334	-0.826±0.056	-0.680±0.021	-0.554±0.056	-0.393±0.021	1.4
1373	-0.925±0.017	-0.729±0.013	-0.672±0.017	-0.445±0.013	1.2
1385	-0.971±0.017	-0.782±0.015	-0.635±0.017	-0.411±0.015	1.0
1400	-0.912±0.019	-0.757±0.014	-0.487±0.019	-0.298±0.014	1.1
1531	-1.148±0.024	-0.887±0.016	-0.013±0.026	0.067±0.015	1.1
1541	-1.158±0.015	-0.909±0.015	-0.037±0.016	0.016±0.018	1.1
1551	-1.137±0.018	-0.916±0.014	0.000±0.024	0.094±0.015	1.2

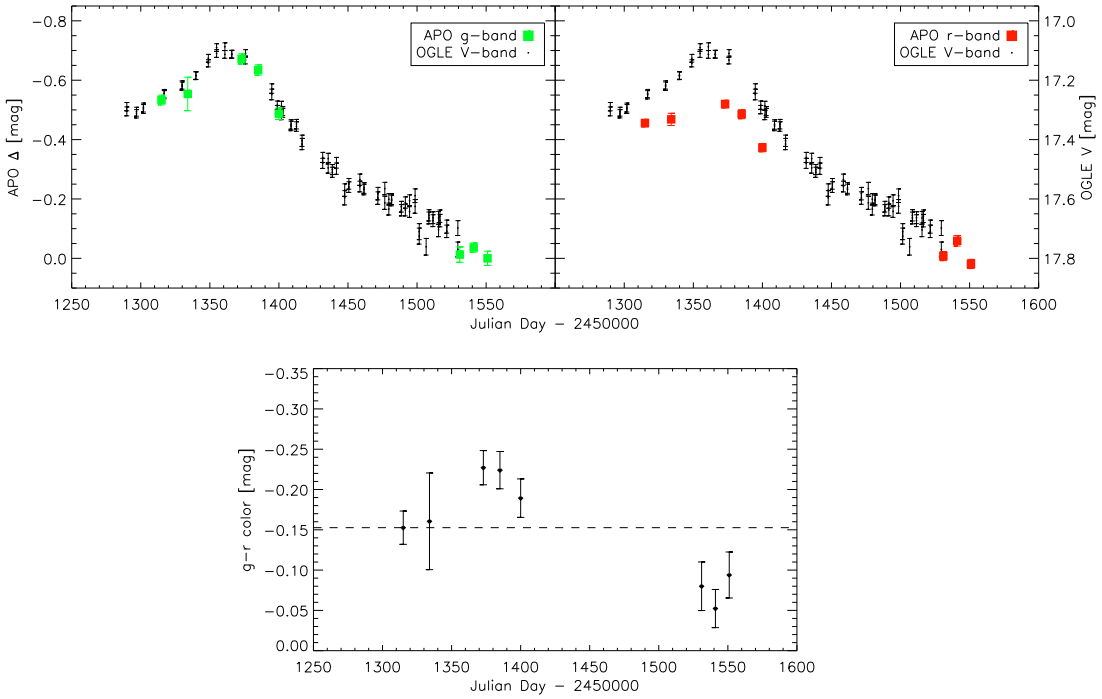

Figure 5.5: *APO light curves. Top left panel: APO g'-band light curve (green squares) of the high magnification event seen in image C of Q 2237+0305 in 1999. Top right panel: APO r'-band light curve for the event (red squares), shifted by 0.075 magnitudes for easier comparison. In black, the OGLE V-band light curve sampling this event is shown. Bottom panel: APO g'-r' color curve. The dashed line is shown as a reference.*

Table 5.2: *Local macro-lensing parameters for quasar images B and C of Q 2237+0305 from Schmidt et al. (1998). κ is the scaled surface density, γ is the shear, μ_{tot} is the total magnification.*

Image	κ	γ	μ_{tot}
B	0.36	0.42	4.29
C	0.69	0.71	2.45

expressed as (Wambsganss 1990):

$$\overrightarrow{y} = \begin{pmatrix} 1-\gamma & 0 \\ 0 & 1+\gamma \end{pmatrix} \overrightarrow{x} - \kappa_c \overrightarrow{x} - \sum_{i=1}^{N} \frac{m_i(\overrightarrow{x} - \overrightarrow{x_i})}{(\overrightarrow{x} - \overrightarrow{x_i})^2} \tag{5.3}$$

where we have set the action of the shear to be parallel to an axis of the plane. $\overrightarrow{x}$ and $\overrightarrow{y}$ are the coordinates of the ray in the lens and source planes, respectively. $\overrightarrow{x_i}$ and m_i are the coordinates and mass of each one of the total N microlenses in the lens plane, respectively.

The pixelated plane is finally normalized by the number of rays shot and the local "macro" magnification (using κ and γ as shown in Equation 2.33) of a given image resulting in a magnification pattern. Each pixel in the magnification pattern reflects the magnification a pixel sized source will experience at a given position.

In our simulations, we use ∼5000 identical mass microlenses distributed in the lens plane (the results do not depend on the mass distribution of the microlenses; Lewis & Irwin 1996). Approximately 10^{11} rays are shot, deflected in the lens plane and collected in a 10,000 by 10,000 pixels (equivalent to 50 Einstein radii by 50 Einstein radii) array in the source plane. The values of surface mass density κ and shear γ are taken from Schmidt et al. (1998) (Table 5.2). Even though we explore different stellar fractions $\kappa_\star$ and κ_c, as the quasar images are located within the central kiloparsec of the lensing galaxy, we focus our work mainly on the $\frac{\kappa_\star}{\kappa}$=1 stellar fraction. We create these magnification patterns for images C and B (the need of a pattern for image B will be explained in the next section).

As shown in Section 5.1, in quasar microlensing the source size is an important parameter because it is comparable with typical caustic scales. In order to study a sample of different source sizes, the raw magnification patterns are convolved with a set of profiles. Mortonson et al. (2005) showed that microlensing fluctuations are relatively insensitive to the source shape, so it is of little consequence whether we choose a standard model accretion disk (Shakura & Sunyaev 1973) or a Gaussian profile. For simplicity, we choose a Gaussian profile for the surface brightness, where the extent of the source is described by the variance σ. The Full Width at Half Maximum (FWHM) is defined as 2.35σ.

We vary the FWHM of a Gaussian profile from 2 to 120 pixels (which corresponds to 0.01 E_R and 0.60 E_R, respectively) for quasar image B and from 2 to 216 pixels (which corresponds to 0.01 E_R and 1.08 E_R, respectively) for quasar image C (the additional magnification patterns for image C are used for the color curve fitting explained in Section 5.5). For patterns below 12 pixels the step size is 2 pixels, and for patterns above 12 pixels the step size is 4 pixels. We find that this linear sampling gives more accurate results when interpolating compared to a logarithmic sampling.

For a specific convolved pattern we can now extract light curves. By defining a track (path of the source in the source plane magnification pattern) with a starting point, direction

and velocity, we extract the pixel counts in the positions of the pattern defined by this track, using bi-linear interpolation. The values are then converted into magnitudes. Figure 5.6 shows an example of extracted light curves using different profile sizes.

5.4 Light curve fitting

5.4.1 OGLE V light curve

Since quasars vary intrinsically, we need to untangle this variation from microlensing. We therefore study the difference between two light curves extracted from microlensing patterns created for different quasar images to eliminate this effect (the time-delay is negligible, see Section 5.1).

Using the V band OGLE light curves sampling this event in both images C and B of the quasar (Woźniak et al. 2000; Udalski et al. 2006) we construct the difference light curve C-B. We have specifically chosen image B to evaluate the difference as it showed the smallest variation during the 1999 event. Simulated light curves for each image are extracted using tracks over microlensing patterns created independently for each image and convolved with a Gaussian profile with the same size. By repeated light curve extraction with variation of the parameters, the best fit to these are obtained from the comparison with the OGLE C-B difference light curve. What is actually fitted are the parameters that define the track from which both light curves are obtained. This track is constrained to have identical direction and velocity in both the patterns C and B, but the starting point can be different among the different patterns. It is important to remark that the direction is set to be the same in both patterns, taking into consideration that the shear direction between images C and D is approximately perpendicular (Witt & Mao 1994).

For the minimization method we use a Levenberg-Marquardt least squares routine in IDL[2]. This routine is a χ^2 minimization based upon MINPACK-1 (Moré et al. 1980). As we are using 68 percent values for our errors, the χ^2 is simply calculated as:

$$\chi^2 = \sum_{i=0}^{DOF} \left(\frac{y_i - f(x_i)}{\sigma_i^{err}} \right)^2 \tag{5.4}$$

where DOF is the number of degrees of freedom, y is the measured value, x is the independent variable model and σ^{err} is the one sigma error of the particular measurement. In the case in which we fit the OGLE data for this event, the number of degrees of freedom is 75. y_i are the differences between the OGLE light curves for images C and B, σ_i^{err} are the uncertainties measured by the OGLE team, x_i are Julian days and $f(x_i)$ are the difference between of the two light curves extracted from the source plane magnification patterns for images C and B, convolved with an identical source profile. We also include a parameter, which we call m_0, that accounts for the magnitude offset between the images.

As the size of each one of the convolved patterns is very large compared to the time scale of the chosen event (of the order of several hundred times), and considering the fact that it is relatively easy to find good fits because of the huge parameter space that such large patterns give, we need to determine a high number of tracks for each pattern. To obtain a statistical sample, we search for 10,000 tracks for each considered source size. The first guesses for each one of the tracks are distributed uniformly. However, during the fitting process the starting

[2]http://cow.physics.wisc.edu/∼craigm/idl/

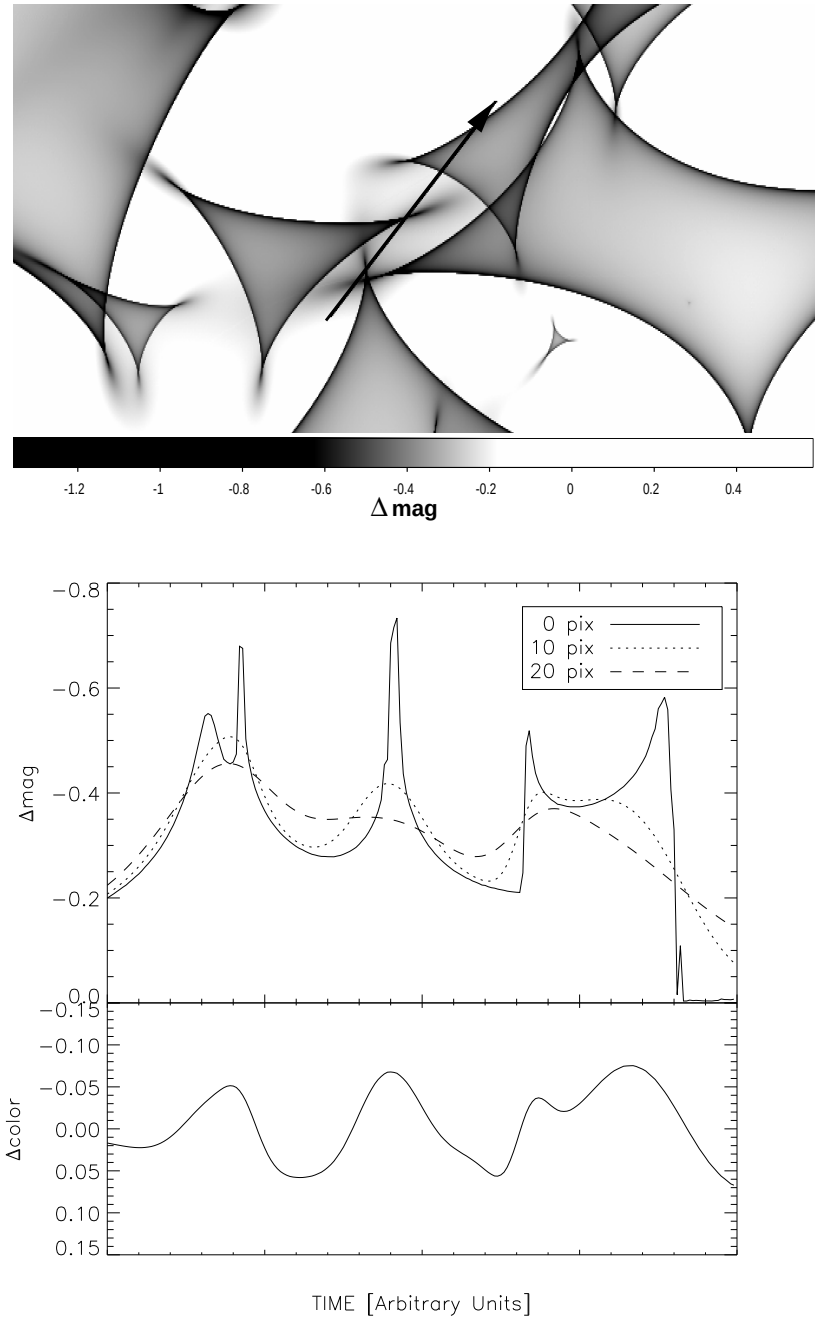

Figure 5.6: *Demonstration of the effect that different source sizes produce on extracted light curves. On the top panel a 1.5 x 3.3 E_R section of a magnification pattern is shown together with a random track in deep black. The middle panel shows the light curves extracted for different source sizes. The continuous, dashed and dotted lines are respectively: no convolution, 10 pixels FWHM and 20 pixels FWHM Gaussian profile convolution. The lower panel shows a color curve between the two mock sizes of 10 and 20 pixels. This is the subtraction of of both light curves.*

points of the tracks are constrained to stay within a square of 200 pixels side-length around the random initial value in order to force a sampling of the whole pattern.

After this minimization is done we have a track library containing 3×10^5 fitted tracks (10,000 tracks for 30 different source sizes with best-fitting velocity and magnitude offset).

5.4.2 APO color curve

Figure 5.5 shows that the OGLE V-band and the APO g'-band light curves are very similar. Since the microlensing effect depends strongly on the source size (see Figure 5.6), we assume for simplicity, that the OGLE V-band continuum region is of similar size as that of the APO's g'-band. Here we determine the ratio of the APO r'-band region and the g'-/OGLE V-band regions that follows from the color curve shown in Figure 5.5.

While the parameters that define the tracks are fixed by the procedure shown in the previous section, the two parameters that influence the shape of the color curve in this step are the ratio between the sizes of the two regions and the intrinsic color g'-r' of the quasar (c_0). These are the only parameters allowed to vary during this step. As before, we use the patterns convolved with Gaussian profiles up to 120 pixels FWHM for image C to obtain the g'-band light curve. To obtain the r'-band light curve we use the full set of patterns for image C. During the fitting process we interpolate the magnitude values of the extracted light curves in order to obtain continuous values for the source size ratio. After this second fitting procedure, the χ^2 values of the track library are updated: $\chi^2{=}\chi^2_{OGLE}{+}\chi^2_{APO}$. An example track of our track library, along its best fit to the light and color curves is shown in Figure 5.7.

5.5 Considerations

5.5.1 Degeneracies

There are two main degeneracies involved in the fitting process. First, the one between the source size and microlens mass. To cope with this, we express the size values in Einstein radii or scaled by a stellar mass as shown in Equation 5.2. Second, is the degeneracy between the size of the source and the transversal velocity we fit. If we fix the path velocity of a source and increase the size of it, its light curve will get broader due to the convolution of the magnification region with a larger profile. Conversely, if we fix a source size and decrease the velocity, the light curve will also become broader because it takes longer time for the source to cross the magnification region. This degeneracy is not absolute, but it is something that must be kept in mind when studying the results of the fitting.

5.5.2 Velocity considerations

The velocity one measures for a microlensing event is composed of different contributions. It is a combination of the velocities of the observer, the lenses and the source. This is a weighted combination of the following form (Kayser et al. 1986):

$$v_t = \frac{v_o}{1+z_l}\frac{D_{LS}}{D_{OL}} - \frac{v_l}{1+z_l}\frac{D_{OS}}{D_{OL}} + \frac{v_s}{1+z_s} \tag{5.5}$$

which for the case of Q 2237+0305 turns into:

$$v_t = 9.85v_0 - 10.81v_l + 0.37v_s \tag{5.6}$$

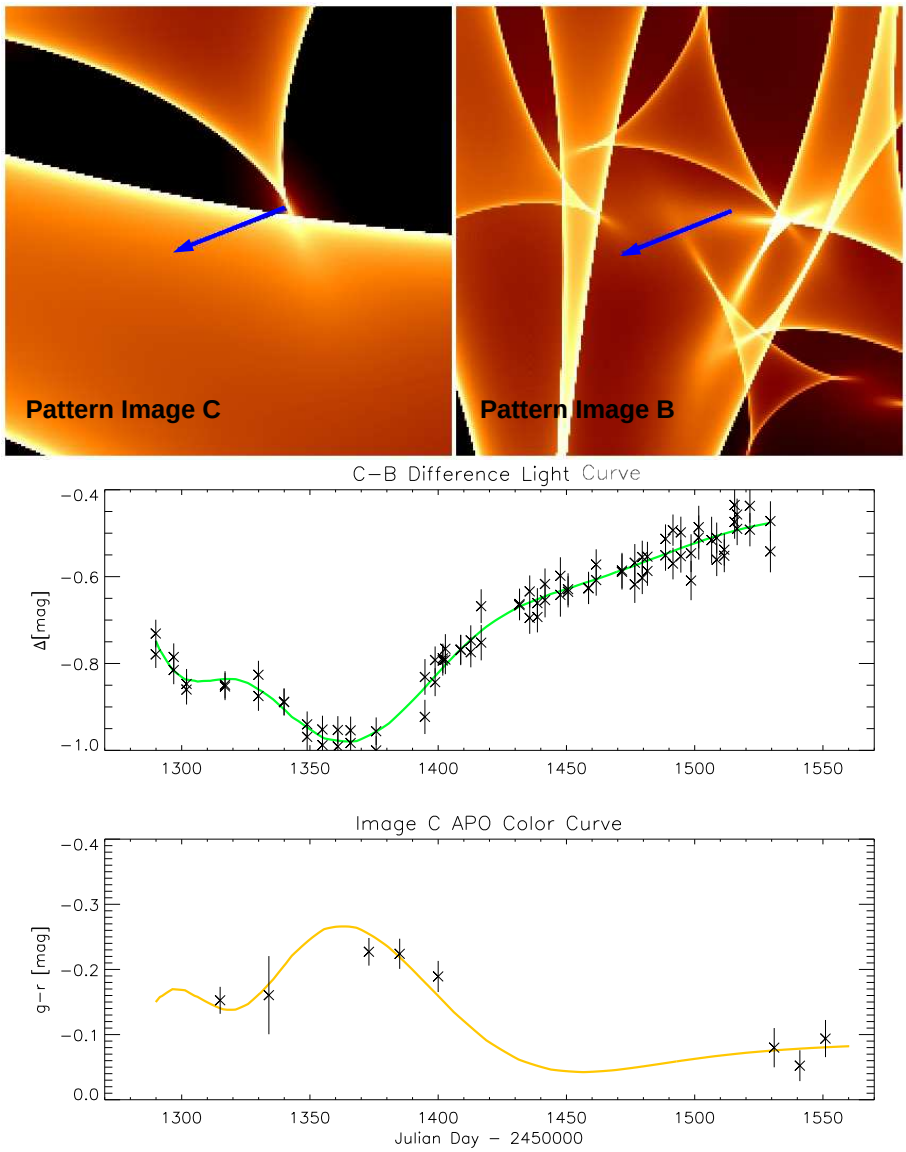

Figure 5.7: *Example track for a 0.05 E_R (10 pixel) FWHM g'-band source size and a source size ratio $\sigma_{r'}/\sigma_{g'}$=1.48. In the top panels the fitted track (blue arrow) is shown in a $1.0E_R \times 1.0E_R$ section of the microlensing patterns. In the middle panel the fitted difference light curve (green line) and the observed OGLE difference light curve (crosses) are shown. In the lower panel the best-fitting color curve (orange line) and the APO g'-r' color curve (crosses) are shown.*

where v_o, v_l and v_s are the velocities of the observer, the lens and the source, respectively. The velocity of the observer is simply the projection of the CMB dipole velocity. The Earth's motion relative to the microwave background is likely to be almost parallel to the direction of the quasar Q 2237+0305 (Witt & Mao 1994), so v_0 is negligible compared to the other velocity values. Thus, Equation 5.6 reduces to only the contribution of the lens and the source to the velocity. If we now assume the velocities of the lens and the source to be of the same order of magnitude, the source velocity is weighted by only 3.5% compared to the lens

velocity. Thus, the main contribution to the final velocity is the velocity of the lens.

This lens velocity has two components: the bulk velocity of the galaxy v_b and the velocity dispersion of the stars in the galaxy (microlenses) v_μ. A complete characterization of it would have required the use of "animated patterns" which consider non-static microlenses, in order to fully quantify the phenomenon. However, since the time span of the event that we fit is of ∼200 days, the significance of individual stellar motions in the fitting would be fairly low. Moreover, Kundic & Wambsganss (1993) and Wambsganss & Kundic (1995) show that, in a statistical sense, the overall effect of the individual stellar motions can be approximated by an artificially increased velocity (a factor ≈1.3) of the source across the pattern.

The scale we use for fitting the velocity is pixels per Julian day. Using Equation 5.2 we can see that this turns into:

$$1\ \frac{pix}{jd}\ =\ 0.005\ \frac{E_R}{jd} = 32870\sqrt{\frac{M}{0.1M_\odot}}\frac{km}{s} \tag{5.7}$$

in the source plane. Using the appropriate velocity scaling (Kayser et al. 1986), we find: 1 $\frac{pix}{jd}$∼3000 $\frac{km}{s}$ in the lens plane.

5.5.3 Size considerations

In a standard thin accretion disk model of a quasar, the black hole is surrounded by a thermally radiating accretion disk (Shakura & Sunyaev 1973). Kochanek et al. (2006) show that the radii R_λ, where radiation with wavelength λ is emitted, scale as $\lambda^{\frac{4}{3}}$. Thus:

$$f = \frac{R_{\lambda_1}}{R_{\lambda_2}} = \left(\frac{\lambda_1}{\lambda_2}\right)^{\frac{4}{3}}. \tag{5.8}$$

For the observed data from APO, the transmission curve for the SPIcam g' and r' filters have central wavelengths of ∼4700Å and ∼6400Å, respectively. Using these values and Equation 5.8 we obtain a predicted thin-disk ratio between the r'- and g'-band source sizes of ∼1.5.

5.6 A statistical approach to light curve analysis

There are different ways to approach quasar microlensing studies. It can be by analytical model fitting of the light curves (e.g., Yonehara 2001), studying the structure function (e.g., Lewis & Irwin 1996), doing statistics of parameter variations over time intervals (e.g., Schmidt & Wambsganss 1998; Wambsganss et al. 2000; Gil-Merino et al. 2005), obtaining probability distributions with light curve derivatives (e.g., Wyithe et al. 2000c) or Bayesian analysis (e.g., Kochanek 2004). Similar to Kochanek (2004), we construct a probability distribution for the quantities of interest (V/g'-band source size, source size ratio and transversal velocity) from our track library.

Each one of our tracks is a fit to the light and color curves and thus has a χ^2 value attached to it. We therefore infer information from the whole ensemble of models: the track library. Using the standard approach for ensemble analysis (e.g., Sambridge 1999), we assign a likelihood estimator to each track t_i: $p(t_i)\propto\exp(\frac{-\chi^2(t_i)}{2})$. Using this likelihood estimator,

the statistical weight for each track can be written as:

$$w(t_i) = \frac{p(t_i)}{n(t_i)} \tag{5.9}$$

where $w(t_i)$, $p(t_i)$ and $n(t_i)$ are, respectively: the weight, the likelihood obtained from the χ^2 and the density parameter for each track t_i. The density parameter describes the local track density in a multidimensional grid, in which each dimension corresponds to a parameter of interest. The density is normalized so that the sum of all the density parameters in the grid equals one. By summing over the statistical weights, we can calculate probability distribution histograms for all the parameters of interest.

Gil-Merino et al. (2005) (from now on G-M05) found an upper limit of 625 $\frac{km}{s}$ (90 percent confidence) on the effective transverse velocity of the lensing galaxy in Q 2237+0305. They performed microlensing simulations assuming microlenses with M=0.1$M_\odot$ for three different source sizes yielding similar results. We use their probability distribution for the velocity obtained with the largest source size value (Figure 5 in G-M05) in a further analysis step, where we factor it into our own probability distributions by importance sampling. In other words, we scale the probability of finding a track based on the G-M05 prior, and then re-obtain the best-fitting value for each parameter and confidence intervals.

5.7 Results and discussion

As described in the previous section, we obtain limits on the source size and transverse velocity from two sets of probability distributions. The first corresponds to the parameters obtained without the use of any prior, and a second one in which we apply the G-M05 prior on the transverse velocity of the lensing galaxy. For each probability distribution of a particular parameter we select the 68 percent confidence level. This is done by making horizontal cuts starting from the highest probability and screening down until 68 percent of the cumulative probability is reached. The distribution, the best-fitting values (or the average of the 68 percent confidence region where no single best-fitting solution is found) and the 68 percent confidence limits for the relevant parameters are shown in Figure 5.9 and Table 5.3. After applying the G-M05 prior only ∼1000 tracks carry 99 percent of the statistical weight. This makes the probability histogram for the source ratio sparsely populated for $\sigma_{r'}/\sigma_{g'}$>2. We therefore require at least 70 of these 1000 tracks to be part of each bin in the histogram in order to avoid low number statistics.

5.7.1 Relative transverse velocity and the size of the accretion disk

Without any velocity prior (see Figure 5.9), we have more fast tracks than slow tracks. No limit on the transversal velocity can be determined. This is mostly due to the degeneracy between source size and transverse velocity (see Section 5.5.1). Using the G-M05 prior, we obtain a best-fitting velocity of $682^{+227}_{-379}\sqrt{\frac{M}{0.1M_\odot}}\frac{km}{s}$ (projected into the lens plane). Note, however, that the distribution shows a longer tail towards the higher velocities when compared to the G-M05 probability distribution because, due to the steepness of the event, the fitting favors fast tracks or small source sizes.

The average Gaussian width we obtain on the OGLE V/APO g' source size without setting the velocity prior is $\sigma_{g'}$=$8.10^{+5.90}_{-5.99}\times10^{-2}R_E$ or $4.60^{+3.36}_{-3.40}\times10^{15}\sqrt{\frac{M}{0.1M_\odot}}cm$. These limits agree with those obtained by Yonehara (2001) and Kochanek (2004) (who used a logarithmic prior

Table 5.3: *Results and confidence limits for g'-band source size, ratio between r'- and g'-band source size and transverse velocity (projected to the lens plane).(*) The velocity obtained without the G-M05 prior is shown without error bars as we do not obtain limits for it.*

	Source Size $\sigma_{g'}$		Ratio	Velocity (*)
	$\times 10^{-2}\ R_E$	$\sqrt{\frac{M}{0.1M_\odot}}$ $\times 10^{15}$[cm]	$\frac{\sigma_{r'}}{\sigma_{g'}}$	$\sqrt{\frac{M}{0.1M_\odot}}$ [km/s]
No Prior	$8.10^{+5.90}_{-5.99}$	$4.60^{+3.36}_{-3.40}$	$1.25^{+0.45}_{-0.15}$	2930
With GM-05 Prior	$2.34^{+0.43}_{-1.28}$	$1.33^{+0.24}_{-0.73}$	$1.45^{+0.90}_{-0.25}$	682^{+227}_{-379}

on the transversal velocity). When we impose the velocity constraints of G-M05 we obtain an OGLE V/APO g' source size with a Gaussian width of $\sigma_{g'}=2.34^{+0.43}_{-1.28} \times 10^{-2} R_E$ which is equivalent to $1.33^{+0.24}_{-0.73} \times 10^{15}\sqrt{\frac{M}{0.1M_\odot}} cm$. This makes the upper limit tighter by a factor of five compared to the previous result, placing it just below the 68 percent confidence limit obtained by Kochanek (2004), very close to their resolution limit. For m_0 (parameter that accounts for the magnitude offset between images C and B; see Section 5.4.1) we obtain -1.75$\lesssim m_0 \lesssim$0.25 without and -0.75$\lesssim m_0 \lesssim$1.25 with the G-M05 prior, respectively.

The source size ratio between the r'- and g'-band emitting regions of the quasar is $\sigma_{r'}/\sigma_{g'}=1.25^{+0.45}_{-0.15}$ without, and $\sigma_{r'}/\sigma_{g'}=1.45^{+0.90}_{-0.25}$ with the G-M05 prior, respectively, coupled with an intrinsic color parameter: c_0=-0.18±0.05 in both cases (see Section 5.4.2). As shown in Figure 5.9, both source size ratio distributions are similar. The measurements are close to the theoretical value (f∼1.5) estimated in Section 5.5.3 with a Shakura & Sunyaev (1973) thermal profile.

5.7.2 Intrinsic variability during the event

We are also able to get information on the intrinsic variability of Q 2237+0305 during the time interval of the 1999 event. The difference light curve fitting, in principle, eliminates the contribution of intrinsic variability:

$$C - B = (C_\mu + I + E_C) - (B_\mu + I + E_B) = C_\mu - B_\mu + m_0 \tag{5.10}$$

where C and B are the observed light curves for images C and B respectively, the subindex μ denotes curves extracted from magnification patterns and I denotes intrinsic variability. E_C and E_B denote the magnitude offset in each image, which we add as the m_0 parameter. However, we can recover the intrinsic variability information by comparing the observed light curves with the ones extracted using our tracks at microlensing patterns for individual images in the following way:

$$I = C - C_\mu - E_C = B - B_\mu - E_B \tag{5.11}$$

Figure 5.8 shows intrinsic variability obtained as derived in Equation 5.11 (with omission of the the constant E_C and E_B values) together with all four OGLE light curves during this event (shifted in magnitude for easy comparison). The intrinsic variability curves result from

the weighted sum of all the tracks in the library (with and without the GM-05 prior) using both images B and C.

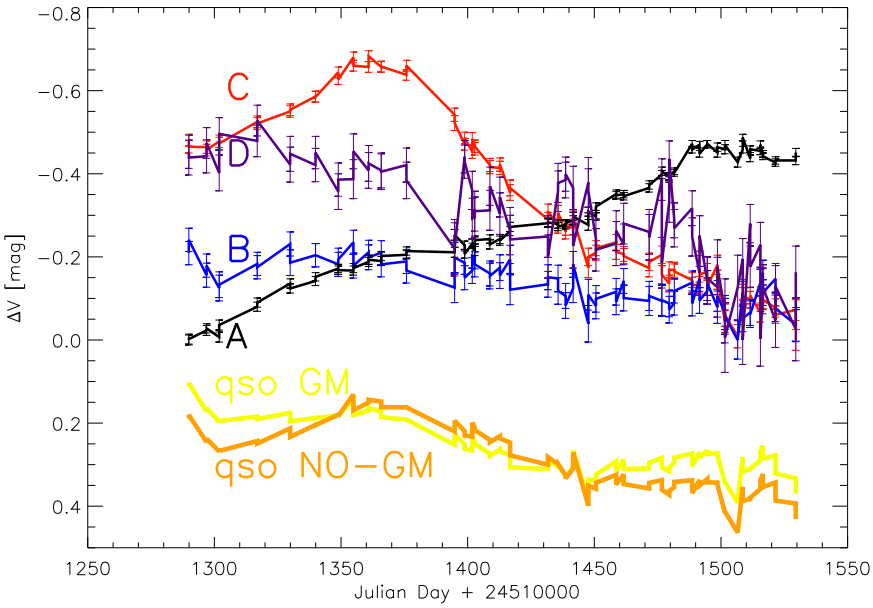

Figure 5.8: *Intrinsic variability of Q 2237+0305 during the 1999 event. The yellow and orange lines shows the weighted average quasar variability with and without the GM-05 prior on the velocity, respectively. The OGLE light curves for the different images are also displayed, shifted in magnitude for easier comparison.*

Even though the intrinsic variability obtained without the GM-05 prior shows a slightly larger range than the one without, both curves are indistinguishable under the noise. The curves show that the quasar varied by ∼0.3 magnitudes during this event declining its brightness towards the end, consistent with the observed light curves for images B, C and D. Image A appears to be entering a high magnification microlensing region therefore smearing out the effect of intrinsic variability on the global light curve. A small residual bump can be seen around Julian day 1370 (seen also by Kochanek 2004) that could be due the lack of knowledge of the exact accretion disk profile.

5.7.3 Is it a caustic crossing event?

For a long time there has been discussion on the nature of the image C event in year 1999 (e.g., Wyithe et al. 2000b; Yonehara 2001; Shalyapin et al. 2002; Kochanek 2004). Using different methods, it was found that this event was likely produced by the source passing near a cusp. In order to investigate this for the tracks in our library, we compute the location of the caustics for each of the magnification patterns using the analytical method by Witt (1990, 1991) (combination of both ray shooting simulations and analytical caustics are shown in Wambsganss et al. 1992).

For each track we determine whether either the center, the center$\pm\sigma_{g'}$ or the center$\pm\sigma_{r'}$ of the source touches a caustic at any time. Our analysis agrees with the previous results when we use the OGLE light curve to fit for this event. However, to reproduce our APO color

Table 5.4: *Probabilities of high magnification event seen in image C of Q 2237+0305 being produced by the source crossing a caustic and of the g' and r'-band region touching a caustic. The table shows the obtained values for the probability both using and not using the Gil-Merino et al. (2005) velocity prior.*

No Prior			With G-M05 Prior		
cross	g'	r'	cross	g'	r'
0.75	0.92	0.97	0.72	0.89	0.94

dataset, tracks that cross a caustic are favored (see Table 5.4). We find that a source with a radius as big as $\sigma_{r'}$ touched a caustic with 97 percent and 94 percent of confidence without and with the G-M05 prior, respectively. Furthermore, the source, regardless of dimensions, crossed a caustic with a 75 percent and 72 percent of confidence without and with the G-M05 prior, respectively (i.e., the center of the source touched a caustic).

The probabilities of the source touching a caustic at different radii are slightly larger in the case in which we do not use the G-M05 prior as seen in detail in Table 5.4. This is due to the fact that a higher velocity makes a track cover more distance through the pattern and thus is more likely to encounter a caustic.

5.8 Summary and conclusions

We present two band (g' and r') APO data covering the high magnification event seen in image C of the quadruple quasar Q 2237+0305 in the year 1999. We find that the amplitude of the brightness peak is more pronounced in the g'-band than in the r'-band. This is also consistent with the observations by Vakulik et al. (2004) (see also the analysis by Koptelova et al. 2007).

By using this data together with the well known OGLE data (Woźniak et al. 2000; Udalski et al. 2006) and combining it with microlensing simulations, we have been able to obtain limits on the size of regions of the quasar's central engine emitting in these bands: Gaussian width $\sigma_{g'}=4.60^{+3.36}_{-3.40} \times 10^{15}\sqrt{M/0.1M_{\odot}}$ cm and $\sigma_{r'}/\sigma_{g'}=1.25^{+0.45}_{-0.15}$.

Because of the degeneracy between source size and transverse velocity we use a prior on the velocity obtained from the work of Gil-Merino et al. (2005) in order to improve the results: Gaussian width $\sigma_{g'}=1.33^{+0.24}_{-0.73} \times 10^{15}\sqrt{M/0.1M_{\odot}}$ cm and $\sigma_{r'}/\sigma_{g'}=1.45^{+0.90}_{-0.25}$. Both values for the ratio between the source sizes are close to the ratio obtained for a face-on Shakura & Sunyaev (1973) accretion disk (f$\sim$1.5). Recent studies (e.g., Poindexter et al. 2007; Morgan et al. 2007; Pooley et al. 2007) suggest microlensing yields a slightly bigger value for the ratio than that obtained analytically with the thin disk model (see Section 5.5.2), also in agreement with our results.

We also show that this event was probably produced by the source directly interacting with a caustic, as we obtain probabilities of 97 percent and 94 percent that the r'-band emitting region touches a caustic without and with the G-M05 prior, respectively, and of 75 percent and 72 percent that the source center (regardless of size) crossed a caustic without and with the G-M05 prior, respectively.

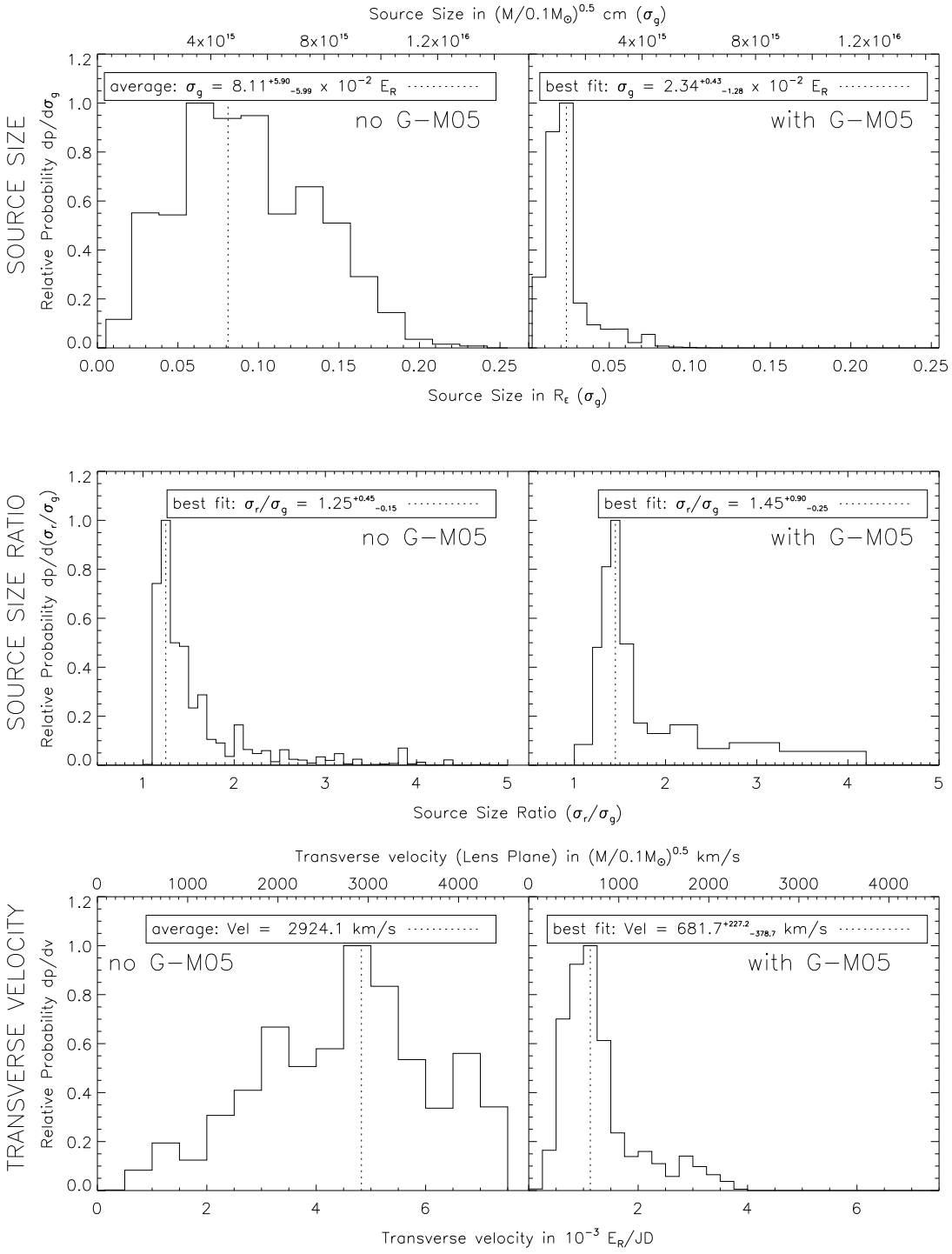

Figure 5.9: *Probability histograms for g' or V source size, r'/g' source size ratio and transverse velocity (projected to the lens plane), respectively. The dotted line shows the best-fitting values (or average of the 68 percent confidence region if no single best-fitting value is found). The uncertainties correspond the 68 percent confidence limits.*

6

Summary and Outlook

This thesis has presented different studies within the context of gravitational lensing, particularly quasar lensing. These have spanned from the confirmation of a strong lens candidate, to the use of the resolution power brought by extragalactic microlensing to probe the inner structure of a lensed quasar. The work presented in this manuscript has been done with a strong interaction between theoretical concepts and high class astronomical observations. Their connection has played a key role in the answering, and also the proposition, of questions concerning the mass distribution of lensing galaxies, the cause of observed flux anomalies and the nature of AGNs.

We have studied in detail COSMOS 5921+0638, a candidate strong lensing system located in the COSMOS field. This system shows an early type galaxy and four point-like images that lie on top of a faint ring surrounding the galaxy. Using spectroscopic data we have measured the redshift of 10 galaxies in the field of the system, including the main lensing galaxy at z_l=0.551±0.001. Coupling photometric criteria with the measurement of a single emission line, we have measured the redshift of the point-like images around the lensing galaxy at z_s=3.14±0.05. Our conclusion on the nature of the system is that it is composed of an AGN (point-like images) being lensed by a foreground elliptical galaxy. The ring around the lensing galaxy is formed by the distortion and magnification of the AGN's host galaxy.

Possible lensing contributions from the environment around COSMOS 5921+0638, using the zCOSMOS optical group catalog (Knobel et al. 2009, submitted), were studied. We find that the mass and tidal perturbations produced by these galaxy groups would not significantly affect the lensing potential of the system. Using PSF fitting techniques we have obtained the brightness and accurate positions of the lensing galaxy and the point-like images. The obtained astrometry was used to constrain mass models for the lensing system. Both non-parametric and parametric models agree in the requirement of a small external shear in order to reproduce the lensed AGN images' configuration. The small external shear could be due to individual galaxies in the line-of-sight to the system, or substructure in the lens potential (also hinted in the non-parametric mass profile reconstruction). The lens modeling allowed the determination of the mass of the lensing galaxy within its Einstein ring (4.5 kpc): $M{\approx}1.2{\times}10^{11}M_{\odot}$ and an estimate of the mass-to-light ratio: $log(M/L){\approx}0.92{\pm}0.12$. The lensing induced magnification revealed the faint nature of the background AGN. Low

Luminosity AGNs (LLAGNs) are expected to be common at high redshifts, but difficult to detect without this natural magnification. Strong lensing of LLAGNs is thus one of the most powerful tools to probe the AGN luminosity function at high redshift.

Flux anomalies are observed between the different quasar images when compared to theoretical expectations, likely due to microlensing. However, with the current temporal information it is not possible to confirm if these anomalies are a static or a dynamic phenomenon. In the immediate future, we plan to obtain new space-based observations of the system to understand the nature of these anomalies. If the new observations reveal no variation of the anomalies, then substructure in the lensing galaxy would likely be the cause of these anomalies. If brightness variations are observed the anomalous flux ratios, then microlensing could be confirmed as the cause for the anomalies, turning this system into an ideal candidate for microlensing monitoring to probe the inner structure of the background LLAGN. In any case, these new observations will allow to further constrain the mass model of the lens and obtain a more accurate description of the mass distribution of the lensing galaxy, as well as the properties of the background AGN and its host galaxy.

Deepening into the analysis of the observed flux of lensed quasars, we have used integral field spectroscopy at the VLT to study the emission of four gravitationally lensed quasars: HE 0230-2130, RX J0911+0551, H 1413+117 and B 1359+154, as well as objects around their line-of-sight. In the field of HE 0230-2130 we have re-obtained the redshifts of the lensing galaxies at z_1=0.521 and z_2=0.523, as well as newly identified a galaxy at z=0.518 at a distance of $\Delta\theta\sim17''$ from the center of the system, thus, likely to be gravitationally related to the main lensing galaxies. In the field of RX J0911+0551 we have confirmed the redshift of one of the member galaxies of the cluster at redshift z=0.78 and we have newly identified a galaxy, at a distance $\Delta\theta\sim12''$ from the lensed quasar images, at a redshift z=0.484, unrelated to the known galaxy cluster and the main lensing galaxy. In the field of H 1413+117 the two absorption systems at z$\sim$1.44 and z$\sim$1.66 are re-obtained with high accuracy, but no new objects are observed.

The spectra of three of these systems (HE 0230-2130, RX J0911+0551 and H 1413+117) revealed anomalies when compared among different images of the same system. Our analysis suggests that microlensing is the most likely cause for these flux anomalies. Under this interpretation, in image D of HE 0230-2130 we have observed a microlensing magnification of the continuum emission, and in images A1 and/or A3 of RX J0911+0551 we see a microlensing de-magnification of the continuum emission. In H 1413+117, comparison with previous datasets reveals that image D has shown a history of microlensing induced variations, in the case of our VIMOS observations, continuum magnification. Furthermore, this system shows anomalies that could be consistent with Broad Line Region microlensing. As microlensing is a dynamic phenomenon, this spectroscopic dataset can be used coupled to existing and future observations of the systems. The study of the dynamic fluctuations of the microlensing affected spectra would allow to study the structure of the accretion disks and Broad Line Regions of the background quasars.

A dynamic microlensing study of the multiple quasar Q 2237+0305 is also shown. We have used the V band OGLE light curves and g' and r' APO light curves covering a magnification event seen in the year 1999. By comparison between them and source plane microlensing simulations, using a fitting algorithm and a statistical interpretation of the results, we have obtained constraints on the structure of the accretion disk of the background quasar. We have taken advantage of the chromatic information available from the APO observations, not only as further constraints on the fitting, but also to obtain the accretion disk size in different

bands. Two sets of results are obtained: those without any prior and those obtained using a velocity prior on the relative transverse velocity between the microlenses and the background quasar (obtained from the work by Gil-Merino et al. 2005). Without the use of the prior, we obtain an accretion disk size with a Gaussian width $\sigma_{V,g'}=4.60^{+3.36}_{-3.40} \times 10^{15}\sqrt{M/0.1M_{\odot}}$ cm and a size ratio $\sigma_{r'}/\sigma_{g'}=1.25^{+0.45}_{-0.15}$. These values change to $\sigma_{g'}=1.33^{+0.24}_{-0.73} \times 10^{15}\sqrt{M/0.1M_{\odot}}$ cm and $\sigma_{r'}/\sigma_{g'}=1.45^{+0.90}_{-0.25}$ when the velocity prior is applied. In both cases, the ratio between the two bands ($\sigma_{r'}/\sigma_{g'}$) is in agreement with the predictions of a thermally emitting accretion disk model (Shakura & Sunyaev 1973). The high chromaticity seen in the event allowed to determine the nature of the magnification event, showing that it was produced by the source crossing a caustic with >72% confidence.

The method used for the analysis of the microlensing event on Q 2237+0305, can be applied to other systems as well. Quasar monitoring projects are currently obtaining light curves for different gravitationally lensed quasars in multiple bands. In time, these light curves are becoming longer and are showing multiple microlensing events, which in turn, will provide additional constraints. Furthermore, from the use of these light curves, time-delay measurements are being obtained. Using these time-delays to shift the image light curves allows to eliminate the intrinsic variability "noise" and extend this kind of analysis to other systems. With this in mind, quasar microlensing sets the ground for the most direct observationally motivated description of the inner structure of high redshift AGNs.

Quasar lensing is far from being a depleted source of astrophysical questions and answers. Large scale cosmological surveys, long time scale monitoring of these variable sources and the advent of more precise astronomical instrumentation, are continuously pushing the frontiers of this subject and its uses. The topics discussed and the open questions presented in this dissertation will certainly benefit from these trends.

A
Influence of the Environment

To study the influence of mass in the line of sight between an observer and a source, we need to study the lensing parameters (convergence κ and shear γ) induced by the body at the position of the lens. As shown in Equation 2.29, κ and γ are defined as:

$$\kappa = \frac{1}{2}(\partial_{xx}\psi + \partial_{yy}\psi) \tag{A.1}$$

$$\gamma_1 = \frac{1}{2}(\partial_{xx}\psi - \partial_{yy}\psi) \tag{A.2}$$

$$\gamma_2 = \partial_{xy}\psi = \partial_{yx}\psi \tag{A.3}$$

where ψ denotes the lens potential of the pertuber. As the shear is defined as a vector, its total magnitude is given by:

$$|\gamma| = \sqrt{\gamma_1^2 + \gamma_2^2} \tag{A.4}$$

and its direction θ_γ as:

$$\theta_\gamma = \frac{1}{2}\arctan\left(\frac{\gamma_1}{\gamma_2}\right). \tag{A.5}$$

In the following, we study the convergence and shear induced by spherically symmetric lenses.

A.1 Point mass

A point mass lens has a potential:

$$\psi = \theta_E^2 \; ln(r) \tag{A.6}$$

which implies a convergence and shear

$$\kappa = 0 \tag{A.7}$$

$$\gamma = \left(\frac{\theta_E}{r}\right)^2. \tag{A.8}$$

A.2 Singular Isothermal Sphere

An isothermal sphere (see Section 2.3.2) has a radial density profile $\rho \propto 1/r^2$ which implies:

$$\kappa = \gamma = \frac{\theta_{E,SIS}}{2}\frac{1}{r^2} \tag{A.9}$$

where

$$\theta_{E,SIS} = \frac{4\pi}{G}\left(\frac{\sigma}{c}\right)^2 \frac{D_{LS}}{D_{OS}} \tag{A.10}$$

is the angular Einstein radius of a Singular Isothermal Sphere, which depends on the 1-D velocity dispersion σ of the lens.

A.3 Truncated isothermal sphere

The isothermal profile decribed above is, in general, an acceptable approximation for the potential of a galaxy. It delivers a good estimate for the shear and convergence when the position of interest is not located very close or very far from the center of the lens potential ($\sim\theta_{E,SIS}$). On the center, the radial density distribution as well as the surface density (convergence κ) diverges to an infinite value. On the other hand, the relatively shallow slope makes that the total mass of the profile (i.e., $\int \rho(r)$) does not converge. Thus, the effect of the perturber is overestimated when it is at a large projected distance (larger than its Einstein radius).

A solution for these issues is to introduce a core radius s and a cut radius a. The core radius eliminates the singularity in the center of the profile, and the cut or effective tidal radius, truncates the profile. This profile has a 3-dimensional density distribution:

$$\rho \propto \frac{1}{r^2+s^2}\frac{1}{r^2+a^2} \tag{A.11}$$

which implies a finite total mass $M = \pi\Sigma_{crit}\tilde{\theta_E}(a-s)$ (see Equation 2.32 for the definition of Σ_{crit}.) The quantity $\tilde{\theta_E}$ is defined in terms of the Einstein radius $\theta_{E,SIS}$ as:

$$\frac{\theta_{E,SIS}}{\tilde{\theta_E}} = 1 + \frac{a}{b} - \sqrt{1+\left(\frac{a}{b}\right)^2}. \tag{A.12}$$

The convergence or surface mass density κ and the shear γ induced by this profile have the form

$$\kappa = \frac{\tilde{b}}{2}\left(\frac{1}{\sqrt{s^2+r^2}} - \frac{1}{\sqrt{a^2+r^2}}\right) \tag{A.13}$$

$$\gamma = \frac{\tilde{b}}{2}\left[\frac{1}{\sqrt{s^2+r^2}} + \frac{1}{\sqrt{a^2+r^2}} - \frac{2a}{s^2+r^2}\left(\frac{\sqrt{a^2+r^2}}{a} - 1\right)\right]. \tag{A.14}$$

In the limit in which $s \to 0$ and $a \to \infty$, the quantities reduce to the Singular Isothermal Sphere parameters: $\tilde{\theta_E} \to \theta_{E,SIS}$ and $\kappa, \gamma \to \kappa_{SIS}, \gamma_{SIS}$.

A.4 Effective convergence and shear

The convergence and shear values defined previously, describe their influence on a redshift plane identical to that of the perturber. As we want to study the effect of groups in the line-of-sight towards a lensed source, these values need to be scaled to an effective convergence $\kappa_{\rm eff}$ and $\gamma_{\rm eff}$ (Keeton 2003):

$$\kappa_{\rm eff} = \frac{(1-B)[\kappa - B(\kappa^2 - \gamma^2)]}{(1-B\kappa)^2 - (B\gamma)^2} \tag{A.15}$$

$$\gamma_{\rm eff} = \frac{(1-B)\gamma}{(1-B\kappa)^2 - (B\gamma)^2}. \tag{A.16}$$

The factor B encodes the redshift difference between the perturber P and the redshift plane where the perturbation needs to be measured, which in the general case, is the redshift of the lens L. B has the form:

$$B = \frac{D_{PL}D_{OS}}{D_{OL}D_{PS}} \quad \text{or} \quad \frac{D_{LP}D_{OS}}{D_{OP}D_{LS}} \tag{A.17}$$

when the pertuber P is located between the observer O and the lens L or when the perturber is located between the lens L and the source S, respectively.

If many perturbers are present in the line of sight towards a lensing system, the contributions from each one of them can be summed as:

$$\kappa_{tot} = \sum_i \kappa_{{\rm eff},i} \tag{A.18}$$

$$\gamma_{1,tot} = \sum_i \gamma_{{\rm eff},i} cos(2\theta_{\gamma,i}) \tag{A.19}$$

$$\gamma_{2,tot} = \sum_i \gamma_{{\rm eff},i} sin(2\theta_{\gamma,i}) \tag{A.20}$$

which amounts to a total external shear of

$$|\gamma_{tot}| = \sqrt{\gamma_{1,tot}^2 + \gamma_{2,tot}^2} \tag{A.21}$$

and its direction θ_γ as:

$$\theta_{\gamma,tot} = \frac{1}{2}\arctan\left(\frac{\gamma_{1,tot}}{\gamma_{2,tot}}\right). \tag{A.22}$$

B

Uncertainty estimation with GALFIT

GALFIT (Peng et al. 2002) is a parameterized two dimensional Levenberg-Marquardt (downhill) fitting algorithm. It fits commonly used 2-D light profiles directly to images. It allows the fitting of multiple profiles per frame convolving with a PSF provided by the user.

GALFIT delivers error estimates on fitted parameters. This error is analytically estimated assuming that surfaces of constant $\Delta\chi^2$ can be approximated by ellipses. This implies that, as a function of n free parameters, the region around the minimum χ^2 is described by a n-dimensional ellipsoid. With this approximation, the uncertainties are obtained from the covariance matrix resulting from the χ^2 minimization. If the fitted parameters are not correlated, an exact analytical description of the parameter uncertainty is obtained. When the parameters are correlated, the uncertainty delivered by GALFIT is an approximate value (see Peng et al. 2002).

This approach however does not account for systematic errors and it is ill-defined when the χ^2 surface is not smooth (e.g., when parameters are forced to be linked between each other) or there are too many correlated parameters. Additionally, it only works on the basis that the reduced χ^2 obtained with the fit is $\chi^2_\nu \sim 1$.

In order to quantify the errors on fitted parameters for a general case, we work out a different approach using a numerical Monte Carlo iterative algorithm. The philosophy of a Monte Carlo algorithm is to create a large number of realizations of the original dataset and obtain independent results from each of them. The distribution of the results, would then provide the uncertainties. In practice, we follow a three step procedure.

The first step is to create a "sigma image". This "sigma image" contains all the image uncertainty information. As described in Peng et al. (2002) it is calculated as:

$$\sigma = \frac{\sqrt{smooth(im \times GAIN \times N) + RD^2 \times N)}}{GAIN} \tag{B.1}$$

where:

- im: the original image in ADUs (Analog-to-Digital Units) or counts.
- $GAIN$: the scale factor of the CCD between the number of electrons and ADUs per pixel.

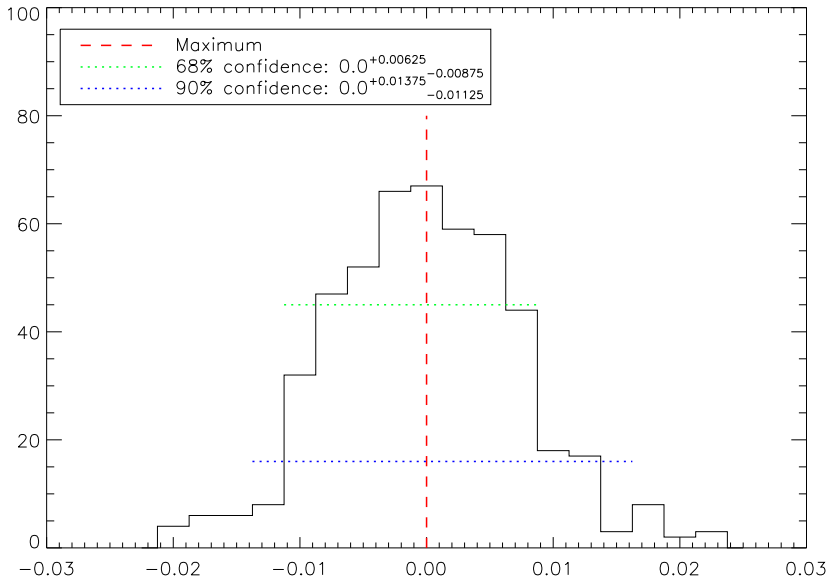

Figure B.1: *Scatter of* GALFIT *results. The figure shows the distribution obtained for a single parameter using a 500 iteration Monte Carlo fitting procedure. The red line shows the most likely value (scaled to zero), the blue line shows the 90% confidence level and the green line shows the 68% confidence level. The legend of the figure displays the associated error bars for each confidence interval.*

- N: the number of images averaged to create the final frame im.
- $smooth$: function that smooths (median filter) the image (in electron counts).
- RD: the electronic read-out noise of the CCD.

From Equation B.1 we can see that the sigma image accounts for the Poisson deviates produced by the electron counts re-scaled to ADUs via the $GAIN$, in order to be used in comparison with the original image (im).

The next step in our iterative procedure is to create a statistical sample of input images to feed the fitting algorithm, with deviations based on the sigma image. Thus, we add Gaussian noise with the appropriate uncertainties to the pixel counts in the original image (i.e., $im_k(i,j)$=$im(i,j)$+$random_k(i,j)\times\sigma(i,j)$). Then, we run a GALFIT minimization over each realization k of the original image. Finally from the scatter of the results obtained with each fit, we obtain our confidence intervals. This is done by integrating the distribution, as shown in Figure B.1.

The method accounts for systematic uncertainties and allows to study the shape of the error distribution. This permits, for example, to assign asymmetric error bars if the most likely value does not coincide with the center of the distribution (asymmetric distribution).

Publication List

- **"The multiple quasar Q2237+0305 under a microlensing caustic"**

  T. Anguita, R.W. Schmidt, E.L Turner, J. Wambsganss, R.L. Webster, K.A. Loomis, D. Long and R. McMillan
  ASTRONOMY & ASTROPHYSICS **480**, 327-334 (2008)

- **"Integral field spectroscopy of four lensed quasars: analysis of their neighborhood and evidence for microlensing"**

  T. Anguita, C. Faure, A. Yonehara, J. Wambsganss, J.P. Kneib, G. Covone and D. Alloin
  ASTRONOMY & ASTROPHYSICS **481**, 615-627 (2008)

- **"Microlensing variability in the gravitationally lensed quasar QSO 2237+0305 ≡ the Einstein Cross"**

  A. Eigenbrod, F. Courbin, G. Meylan, E. Agol, **T. Anguita**, R. W. Schmidt, and J. Wambsganss
  ASTRONOMY & ASTROPHYSICS **490**, 933-943 (2008)

- **"Redshifts and lens profile for the double quasar QJ 0158-4325"**

  C. Faure, **T. Anguita**, A. Eigenbrod, J.-P. Kneib, V. Chantry, D. Alloin, N. Morgan and G. Covone
  ASTRONOMY & ASTROPHYSICS: accepted. arXiv:0812.1308 (2008)

- **"A systematic fitting scheme for caustic-crossing microlensing events"**

  N. Kains, A. Cassan, K. Horne, M.D. Albrow, S. Dieters, P. Fouque, J. Greenhill, A. Udalski, M. Zub, D.P. Bennett, M. Dominik, J. Donatowicz, D. Kubas, Y. Tsapras, **T. Anguita**, V. Batista, J.-P. Beaulieu, S. Brillant, M. Bode, D.M. Bramich, M. Burgdorf, J.A.R. Caldwell, K.H. Cook, Ch. Coutures, D. Dominis Prester, U.G. Jorgensen, S. Kane, J.B. Marquette, R. Martin, J. Menzies, K.R. Pollard, N. Rattenbury, K.C. Sahu, C. Snodgrass, I. Steele, C. Vinter, J. Wambsganss, A. Williams, M. Kubiak, G. Pietrzynski, I. Soszynski, O. Szewczyk, M.K. Szymanski, K. Ulaczyk, L. Wyrzykowski
  MONTHLY NOTICES OF THE ROYAL ASTRONOMICAL SOCIETY: submitted. arXiv:0901.1285 (2009)

- **"High-precision photometry by telescope defocussing. I. The transiting planetary system WASP-5"**

  J. Southworth, T. C. Hinse, U. G. Jørgensen, M. Dominik, D. Ricci, M. J. Burgdorf, A. Hornstrup, P. J. Wheatley, **T. Anguita**, V. Bozza, S. Calchi Novati, K. Harpsøe, C. Liebig, L. Mancini, G. Masi, S. Rahvar, G. Scarpetta, C. Snodgrass, J. Surdej, J. Teuber, C. C. Thöne, M. Zub
  MONTHLY NOTICES OF THE ROYAL ASTRONOMICAL SOCIETY: submitted. (2009)

- **"COSMOS 5921+0638: Characterization and analysis of a new strong gravitational lensing system"**

  T. Anguita, C. Faure, J.P. Kneib, J. Wambsganss, C. Knobel and A. Koekemoer
  ASTRONOMY & ASTROPHYSICS: to be submitted. (2009)

- **"A quasar under a microlensing caustic"**

  T. Anguita and R.W. Schmidt
  PROCEEDINGS OF SCIENCE GMC8-013(2008)

Bibliography

Abajas, C., Mediavilla, E., Muñoz, J. A., Popović, L. Č., & Oscoz, A. 2002, ApJ, 576, 640 4.6.1

Abdelsalam, H. M., Saha, P., & Williams, L. L. R. 1998, AJ, 116, 1541 2.3.5

Alard, C. & Lupton, R. H. 1998, ApJ, 503, 325 5.2.2

Alcalde, D., Mediavilla, E., Moreau, O., et al. 2002, ApJ, 572, 729 5.1

Alcock, C., Allsman, R. A., Alves, D. R., et al. 2000, ApJ, 542, 281 2.3.4

Angonin, M.-C., Vanderriest, C., Remy, M., & Surdej, J. 1990, A&A, 233, L5 4.2, 4.6.3

Anguita, T., Faure, C., Yonehara, A., et al. 2008a, A&A, 481, 615 4

Anguita, T., Schmidt, R. W., Turner, E. L., et al. 2008b, A&A, 480, 327 2.3.4, 5

Antonucci, R. 1993, ARAA, 31, 473 2.1.3

Bade, N., Fink, H. H., Engels, D., et al. 1995, A&AS, 110, 469 4.2.2

Bade, N., Siebert, J., Lopez, S., Voges, W., & Reimers, D. 1997, A&A, 317, L13 4.2, 4.2.2, 4.5.2

Baltz, E. A. & Gondolo, P. 2001, ApJ, 559, 41 2.3.4

Bartelmann, M. & Schneider, P. 2001, Phys. R., 340, 291 2.3.3

Beaulieu, J.-P., Bennett, D. P., Fouqué, P., et al. 2006, Nature, 439, 437 2.3.4

Beckwith, S. V. W., Rix, H.-W., Peng, C., et al. 2002, in Bulletin of the American Astronomical Society, Vol. 34, Bulletin of the American Astronomical Society, 1154–+ 3.1

Beckwith, S. V. W., Stiavelli, M., Koekemoer, A. M., et al. 2006, AJ, 132, 1729 3.1

Blandford, R. & Narayan, R. 1986, ApJ, 310, 568 4.6.2

Blandford, R. D. & Kochanek, C. S. 1987, ApJ, 321, 658 4.6.2

Blanton, M., Turner, E. L., & Wambsganss, J. 1998, MNRAS, 298, 1223 5.2.2

Bohlin, R. C., Savage, B. D., & Drake, J. F. 1978, ApJ, 224, 132 4.6.1

Bond, I. A., Abe, F., Dodd, R. J., et al. 2001, MNRAS, 327, 868 2.3.4

Borgeest, U. & Schramm, K. J. 1993, in The Need for a Dedicated Optical Quasar Monitoring Telescope, ed. U. Borgeest, K. J. Schramm, & J. von Linde, 105–+ 2.3.4

Bower, G. A., Wilson, A. S., Heckman, T. M., & Richstone, D. O. 1996, AJ, 111, 1901 3.6.2

Boyle, B. J., Fong, R., Shanks, T., & Peterson, B. A. 1987, MNRAS, 227, 717 2.1.2

Burud, I., Courbin, F., Lidman, C., et al. 1998, ApJL, 501, L5+ 4.2.2

Cabanac, R. A., Alard, C., Dantel-Fort, M., et al. 2007, A&A, 461, 813 3.2.1

Capak, P., Aussel, H., Ajiki, M., et al. 2007, ApJS, 172, 99 3.2.1, 3.1, 3.4.2

Cardelli, J. A., Clayton, G. C., & Mathis, J. S. 1989, ApJ, 345, 245 4.6.1

Chae, K.-H. & Turnshek, D. A. 1999, ApJ, 514, 587 4.6.3

Chang, K. & Refsdal, S. 1979, Nature, 282, 561 1

Chartas, G., Dai, X., Gallagher, S. C., et al. 2001, ApJ, 558, 119 4.5.2

Chartas, G., Kochanek, C. S., Dai, X., Morgan, N., & Garmire, G. P. 2006, in Bulletin of the American Astronomical Society, Vol. 38, Bulletin of the American Astronomical Society, 987–+ 2.3.4

Chiu, H. 1964, Physics Today, 17, 21 2.1.1

Cid Fernandes, R., González Delgado, R. M., Schmitt, H., et al. 2004, ApJ, 605, 105 3.6.2

Claeskens, J.-F. & Surdej, J. 2002, A&A R., 10, 263 2.3.3

Corrigan, R. T., Irwin, M. J., Arnaud, J., et al. 1991, AJ, 102, 34 2.3.4, 5.1, 5.1

Covone, G., Kneib, J.-P., Soucail, G., et al. 2006, A&A, 456, 409 4.4

Dalal, N. & Kochanek, C. S. 2002, ApJ, 572, 25 2.3.3

de Vaucouleurs, G. 1948, Annales d'Astrophysique, 11, 247 2.3.5, 3.4.2, 5.2.2

Dickinson, M., Giavalisco, M., & The Goods Team. 2003, in The Mass of Galaxies at Low and High Redshift, ed. R. Bender & A. Renzini, 324–+ 3.1

Diego, J. M., Sandvik, H. B., Protopapas, P., et al. 2005, MNRAS, 362, 1247 2.3.5

Eigenbrod, A., Courbin, F., Meylan, G., et al. 2008, A&A, 490, 933 2.3.4

Eigenbrod, A., Courbin, F., Meylan, G., Vuissoz, C., & Magain, P. 2006, A&A, 451, 759 4.2.1, 4.5.1

Elíasdóttir, Á., Hjorth, J., Toft, S., Burud, I., & Paraficz, D. 2006, ApJS, 166, 443 2.3.3

Falco, E. E., Gorenstein, M. V., & Shapiro, I. I. 1985, ApJL, 289, L1 3.6.1

Faure, C., Alloin, D., Kneib, J. P., & Courbin, F. 2004, A&A, 428, 741 4.2.1, 4.2.3

Faure, C., Kneib, J.-P., Covone, G., et al. 2008, ApJS, 176, 19 3.1, 3.2.1, 3.2.2, 3.4.2, 3.8

Fukugita, M., Shimasaku, K., & Ichikawa, T. 1995, PASP, 107, 945 3.6.3

Garilli, B., Scodeggio, M., Franzetti, P., & Zanichelli, A. 2007, VIPGI - The VIMOS Interactive Pipeline and Graphical Interface Cookbook 4.4

Gaskell, C. M., Koratkar, A. P., Kwon, T.-Y., et al. 1987, in Bulletin of the American Astronomical Society, Vol. 19, Bulletin of the American Astronomical Society, 1074–+ 2.1.2

Giavalisco, M. 1998, in The Hubble Deep Field, ed. M. Livio, S. M. Fall, & P. Madau, 121–+ 3.3.1

Gil-Merino, R., Wambsganss, J., Goicoechea, L. J., & Lewis, G. F. 2005, A&A, 432, 83 2.3.4, 5.6, 5.6, 5.4, 5.8, 6

Golse, G., Kneib, J.-P., & Soucail, G. 2002, A&A, 387, 788 2.3.3

Gordon, K. D., Clayton, G. C., Misselt, K. A., Landolt, A. U., & Wolff, M. J. 2003, ApJ, 594, 279 4.6.1

Gould, A. 2008, ArXiv e-prints 2.3.4

Gould, A. & Loeb, A. 1992, ApJ, 396, 104 2.3.4

Hewitt, J. N., Turner, E. L., Lawrence, C. R., Schneider, D. P., & Brody, J. P. 1992, AJ, 104, 968 3.3.1

Heyrovský, D. 2003, ApJ, 594, 464 2.3.4

Hogg, D. W. 1999, ArXiv Astrophysics e-prints 2.2, 2.2.2

Huchra, J., Gorenstein, M., Kent, S., et al. 1985, AJ, 90, 691 2.3.4, 5.1

Hutsemekers, D. 1993, A&A, 280, 435 4.6.3

Hutsemekers, D., Surdej, J., & van Drom, E. 1994, Ap&SS, 216, 361 4.6.3

Impey, C. D., Falco, E. E., Kochanek, C. S., et al. 1998, ApJ, 509, 551 3.1

Irwin, M. J., Webster, R. L., Hewett, P. C., Corrigan, R. T., & Jedrzejewski, R. I. 1989, AJ, 98, 1989 1, 5.1

Jackson, N. 2008, MNRAS, 389, 1311 3.1

Jean, C. & Surdej, J. 1998, A&A, 339, 729 4.6.1

Jullo, E., Kneib, J.-P., Limousin, M., et al. 2007, New Journal of Physics, 9, 447 2.3.5, 3.6.2

Kaspi, S., Smith, P. S., Netzer, H., et al. 2000, ApJ, 533, 631 4.6.1

Kassiola, A. & Kovner, I. 1993, ApJ, 417, 450 2.3.5

Kayser, R. & Refsdal, S. 1989, Nature, 338, 745 5.1

Kayser, R., Refsdal, S., & Stabell, R. 1986, A&A, 166, 36 5.1, 5.5.2, 5.5.2

Kayser, R., Surdej, J., Condon, J. J., et al. 1990, ApJ, 364, 15 4.6.3

Keeton, C. R. 2001a, ArXiv Astrophysics e-prints 2.3.5

Keeton, C. R. 2001b, ArXiv Astrophysics e-prints 2.3.5

Keeton, C. R. 2003, ApJ, 584, 664 A.4

Keeton, C. R., Kochanek, C. S., & Falco, E. E. 1998, ApJ, 509, 561 3.6.3

Keeton, C. R., Kochanek, C. S., & Seljak, U. 1997, ApJ, 482, 604 3.6.1

Kerins, E., Darnley, M. J., Duke, J. P., et al. 2006, MNRAS, 365, 1099 2.3.4

Kinney, A. L., Calzetti, D., Bohlin, R. C., et al. 1996, ApJ, 467, 38 3.3.2, 4.5

Kneib, J.-P. 1993, Ph. D. thesis, Université Paul Sabatier, Toulouse 2.3.5, 3.6.2

Kneib, J.-P., Alloin, D., & Pello, R. 1998, A&A, 339, L65 4.2.3

Kneib, J.-P., Cohen, J. G., & Hjorth, J. 2000, ApJL, 544, L35 4.2.2, 4.5.2

Knop, R. A., Aldering, G., Amanullah, R., et al. 2003, ApJ, 598, 102 2.2.1

Kochanek, C. S. 1991, ApJ, 373, 354 2.3.5

Kochanek, C. S. 2004, ApJ, 605, 58 2.3.4, 5.1, 5.6, 5.7.1, 5.7.2, 5.7.3

Kochanek, C. S., Dai, X., Morgan, C., et al. 2006, ArXiv Astrophysics e-prints 5.5.3

Kochanek, C. S. & Dalal, N. 2004, ApJ, 610, 69 3.7

Koekemoer, A. M., Aussel, H., Calzetti, D., et al. 2007, ApJS, 172, 196 3.2.1, 3.1

Komatsu, E., Dunkley, J., Nolta, M. R., et al. 2008, ArXiv e-prints 2.2.2

Koptelova, E., Shimanovskaya, E., Artamonov, B., et al. 2005, MNRAS, 356, 323 5.1

Koptelova, E., Shimanovskaya, E., Artamonov, B., & Yagola, A. 2007, MNRAS, 381, 1655 5.8

Krolik, J. H. & Lepp, S. 1989, ApJ, 347, 179 2.1.3

Kundic, T. & Wambsganss, J. 1993, ApJ, 404, 455 5.5.2

Laor, A. 2004, in Astronomical Society of the Pacific Conference Series, Vol. 311, AGN Physics with the Sloan Digital Sky Survey, ed. G. T. Richards & P. B. Hall, 169–+ 2.1.3

Lewis, G. F. & Belle, K. E. 1998, MNRAS, 297, 69 4.6.3

Lewis, G. F. & Irwin, M. J. 1996, MNRAS, 283, 225 5.3, 5.6

Lilly, S. & Zcosmos Team. 2008, The Messenger, 134, 35 3.2.2

Lilly, S. J., Le Fèvre, O., Renzini, A., et al. 2007, ApJS, 172, 70 3.2.2

Magain, P., Surdej, J., Swings, J.-P., Borgeest, U., & Kayser, R. 1988, Nature, 334, 325 4.2.3, 4.5.3

Melia, F. & Falcke, H. 2001, ARAA, 39, 309 2.1.2

Moré, J. J., Garbow, B. S., & Hillstrom, K. E. 1980, User Guide for MINPACK-1, Report ANL-80-74 5.4.1

Morgan, C. W., Kochanek, C. S., Morgan, N. D., & Falco, E. E. 2007, ArXiv e-prints, 707 5.8

Morgan, N. D., Caldwell, J. A. R., Schechter, P. L., et al. 2004, AJ, 127, 2617 3.3.1

Mortonson, M. J., Schechter, P. L., & Wambsganss, J. 2005, ApJ, 628, 594 5.3

Muñoz, J. A., Falco, E. E., Kochanek, C. S., et al. 1998, Ap&SS, 263, 51 4.1, 5.1

Myers, S. T., Rusin, D., Fassnacht, C. D., et al. 1999, AJ, 117, 2565 4.2.4

Narayan, R. & Bartelmann, M. 1996, ArXiv Astrophysics e-prints 2.3, 2.6

Navarro, J. F., Frenk, C. S., & White, S. D. M. 1997, ApJ, 490, 493 2.3.5

Newton, I. 1704, Opticks 1

Ostensen, R., Refsdal, S., Stabell, R., et al. 1996, A&A, 309, 59 5.1

Ostensen, R., Remy, M., Lindblad, P. O., et al. 1997, A&AS, 126, 393 4.6.3

Paczynski, B. 1986, ApJ, 304, 1 2.3.4

Park, B.-G., Jeon, Y.-B., Lee, C.-U., & Han, C. 2006, ApJ, 643, 1233 2.3.4

Peebles, P. J. E. 1994, Physical Cosmology (Princeton, NJ: Princeton University Press) 2.2, 2.2.1, 2.2.2

Pen, U.-L., Howard, A., Huang, X., et al. 1993, in Liege International Astrophysical Colloquia, Vol. 31, Liege International Astrophysical Colloquia, ed. J. Surdej, D. Fraipont-Caro, E. Gosset, S. Refsdal, & M. Remy, 111–+ 5.1

Peng, C. Y., Ho, L. C., Impey, C. D., & Rix, H.-W. 2002, AJ, 124, 266 3.4, 5.2.2, B

Peterson, B. M., Ferrarese, L., Gilbert, K. M., et al. 2004, ApJ, 613, 682 2.1.3

Peterson, B. M., Wanders, I., Bertram, R., et al. 1998, ApJ, 501, 82 4.6.1

Poindexter, S., Morgan, N., & Kochanek, C. S. 2007, ArXiv e-prints, 707 5.8

Pooley, D., Blackburne, J. A., Rappaport, S., & Schechter, P. L. 2007, ApJ, 661, 19 5.8

Rees, M. J. 1984, ARAA, 22, 471 2.1.2

Refsdal, S. 1964a, MNRAS, 128, 307 2.3.3

Refsdal, S. 1964b, MNRAS, 128, 295 2.3.1

Reichard, T. A., Richards, G. T., Hall, P. B., et al. 2003, AJ, 126, 2594 4.5.2

Rhodes, J. D., Massey, R., Albert, J., et al. 2006, in The 2005 HST Calibration Workshop: Hubble After the Transition to Two-Gyro Mode, ed. A. M. Koekemoer, P. Goudfrooij, & L. L. Dressel, 21–+ 3.4.1

Rhodes, J. D., Massey, R. J., Albert, J., et al. 2007, ApJS, 172, 203 3.4.1

Richards, G. T., Strauss, M. A., Fan, X., et al. 2006, AJ, 131, 2766 2.1.2, 2.1

Rix, H.-W., Schneider, D. P., & Bahcall, J. N. 1992, AJ, 104, 959 5.1

Rusin, D., Kochanek, C. S., Norbury, M., et al. 2001, ApJ, 557, 594 4.2.4

Saha, P. 2000, AJ, 120, 1654 2.3.5

Saha, P. & Williams, L. L. R. 1997, MNRAS, 292, 148 2.3.5

Saha, P. & Williams, L. L. R. 2004, AJ, 127, 2604 2.3.5, 3.6.1, 3.6.1

Sambridge, M. 1999, Geophys. J Int., 138, 727 5.6

Schechter, P. L., Bailyn, C. D., Barr, R., et al. 1997, ApJL, 475, L85+ 3.3.1

Schechter, P. L. & Wambsganss, J. 2002, ApJ, 580, 685 4.6.2

Schmidt, M. 1963, Nature, 197, 1040 2.1.1

Schmidt, R. & Wambsganss, J. 1998, A&A, 335, 379 5.6

Schmidt, R., Webster, R. L., & Lewis, G. F. 1998, MNRAS, 295, 488 5.2, 5.3

Schmidt, R. W. 1996, Master's thesis, University of Melbourne 5.2.2

Schmidt, R. W., Kundić, T., Pen, U.-L., et al. 2002, A&A, 392, 773 5.1

Schneider, D. P., Turner, E. L., Gunn, J. E., et al. 1988, AJ, 96, 1755 5.1

Schneider, P., Ehlers, J., & Falco, E. 1992, Gravitational Lenses, Astronomy and Astrophysics Library (Berlin, Germany; New York, U.S.A.: Springer) 2.2, 2.3, 4.6.1

Schneider, P., Kochanek, C., & Wambsganss, J. 2006, Gravitational Lensing: Strong, Weak and Micro (Swiss Society for Astrophysics and Astronomy) 2.3

Schneider, P. & Wambsganss, J. 1990, A&A, 237, 42 4.6.1

Scodeggio, M., Franzetti, P., Garilli, B., et al. 2005, PASP, 117, 1284 4.4, 4.4.3

Scoville, N., Aussel, H., Brusa, M., et al. 2007, ApJS, 172, 1 3.1, 3.2.1

Shakura, N. I. & Sunyaev, R. A. 1973, A&A, 24, 337 2.1.3, 4.6.1, 5.1, 5.3, 5.5.3, 5.7.1, 5.8, 6

Shalyapin, V. N., Goicoechea, L. J., Alcalde, D., et al. 2002, ApJ, 579, 127 5.1, 5.1, 5.7.3

Shapiro, I. I. 1964, Physical Review Letters, 13, 789 2.3.1

Sluse, D., Surdej, J., Claeskens, J.-F., et al. 2003, A&A, 406, L43 3.1

Storchi-Bergmann, T., Eracleous, M., Livio, M., et al. 1995, ApJ, 443, 617 3.6.2

Sumi, T., Woźniak, P. R., Udalski, A., et al. 2006, ApJ, 636, 240 2.3.4

Tisserand, P., Le Guillou, L., Afonso, C., et al. 2007, A&A, 469, 387 2.3.4

Trott, C. M. & Webster, R. L. 2002, MNRAS, 334, 621 5.2.2

Trotter, C. S., Winn, J. N., & Hewitt, J. N. 2000, ApJ, 535, 671 2.3.5

Turnshek, D. 1994, in HST Proposal, 5621–+ 4.1

Turnshek, D. A., Lupie, O. L., Rao, S. M., Espey, B. R., & Sirola, C. J. 1997, ApJ, 485, 100 4.6.3

Udalski, A. 2003, Acta Astronomica, 53, 291 2.3.4

Udalski, A., Szymanski, M. K., Kubiak, M., et al. 2006, Acta Astronomica, 56, 293 2.3.4, 5.1, 5.2, 5.2, 5.4.1, 5.8

Vakulik, V. G., Dudinov, V. N., Zheleznyak, A. P., et al. 1997, Astronomische Nachrichten, 318, 73 5.1

Vakulik, V. G., Schild, R. E., Dudinov, V. N., et al. 2004, A&A, 420, 447 5.1, 5.8

Vanden Berk, D. E., Richards, G. T., Bauer, A., et al. 2001, AJ, 122, 549 2.1.3

Wagner, S., Sanchez-Pons, F., Quirrenbach, A., & Witzel, A. 1990, A&A, 235, L1 2.1.2, 3.7

Walsh, D., Carswell, R. F., & Weymann, R. J. 1979, Nature, 279, 381 1

Wambsganss, J. 1990, PhD Thesis, Ludwig-Maximilians-Universität München, 432 5.3

Wambsganss, J. 1997, MNRAS, 284, 172 2.3.4

Wambsganss, J. 1999, Journal of Computational and Applied Mathematics, 109, 353 5.3

Wambsganss, J. & Kundic, T. 1995, ApJ, 450, 19 5.5.2

Wambsganss, J. & Paczynski, B. 1991, AJ, 102, 864 4.6.1, 5.1

Wambsganss, J. & Paczynski, B. 1994, AJ, 108, 1156 5.1

Wambsganss, J., Paczynski, B., & Schneider, P. 1990, ApJL, 358, L33 2.3.4, 5.1

Wambsganss, J., Schmidt, R. W., Colley, W., Kundić, T., & Turner, E. L. 2000, A&A, 362, L37 2.3.4, 5.6

Wambsganss, J., Witt, H. J., & Schneider, P. 1992, A&A, 258, 591 5.7.3

Webster, R. L. & Hewett, P. C. 1990, in Lecture Notes in Physics, Berlin Springer Verlag, Vol. 360, Gravitational Lensing, ed. Y. Mellier, B. Fort, & G. Soucail, 73–82 2.1.2

Wisotzki, L., Christlieb, N., Liu, M. C., et al. 1999, A&A, 348, L41 4.2.1, 4.5.1

Wisotzki, L., Koehler, T., Groote, D., & Reimers, D. 1996, A&AS, 115, 227 4.2.1

Witt, H. J. 1990, A&A, 236, 311 5.7.3

Witt, H.-J. 1991, PhD Thesis, Universität Hamburg, 432 5.7.3

Witt, H. J. & Mao, S. 1994, ApJ, 429, 66 5.4.1, 5.5.2

Woźniak, P. R., Udalski, A., Szymański, M., et al. 2000, ApJL, 540, L65 2.3.4, 5.1, 5.2, 5.2, 5.2.2, 5.4.1, 5.8

Wyithe, J. S. B., Webster, R. L., & Turner, E. L. 2000a, MNRAS, 318, 762 5.1

Wyithe, J. S. B., Webster, R. L., & Turner, E. L. 2000b, MNRAS, 318, 1120 5.1, 5.1, 5.7.3

Wyithe, J. S. B., Webster, R. L., & Turner, E. L. 2000c, MNRAS, 312, 843 5.6

Wyithe, J. S. B., Webster, R. L., & Turner, E. L. 2000d, MNRAS, 315, 337 5.1

Wyithe, J. S. B., Webster, R. L., Turner, E. L., & Agol, E. 2000e, MNRAS, 318, 1105 5.1

Wyithe, J. S. B., Webster, R. L., Turner, E. L., & Mortlock, D. J. 2000f, MNRAS, 315, 62 5.1

Yonehara, A. 2001, ApJL, 548, L127 5.1, 5.1, 5.6, 5.7.1, 5.7.3

Yonehara, A., Mineshige, S., Manmoto, T., et al. 1998, ApJL, 501, L41+ 4.6.1

Zanichelli, A., Garilli, B., Scodeggio, M., et al. 2005, PASP, 117, 1271 4.3.1, 4.2, 4.4, 4.3

Zebrun, K., Soszynski, I., Wozniak, P. R., et al. 2001, Acta Astronomica, 51, 317 2.3.4

List of Figures

List of Tables

Acknowledgments

During the course of my PhD, many different people have supported me in one way or another and, here, I have the opportunity to acknowledge them. First of all, I would like to thank my supervisor Prof. Joachim Wambsganss for providing me the opportunity to come to Heidelberg to do my PhD and the financial support when it was needed. I appreciate the confidence he always presented towards my work and his accurate advice.

My PhD could not have been possible without the financial and scientific support provided by the European Community's Sixth Framework Marie Curie Research Training Network Programme, Contract No. MRTN-CT-2004-505183 "ANGLES" and the "International Max Planck Research School for Astronomy and Cosmic Physics at the University of Heidelberg" (IMPRS-HD).

I would like to thank Prof. Stefan Wagner, Prof. Eva Grebel and Prof. Ulrich Uwer for kindly agreeing to form part of my examination committee.

I have been very lucky to be part of our lensing group at ARI, where I have met many people that helped me during my PhD. I am very grateful to Cécile Faure for her constant guidance, friendship and understanding. She has been an important support in many levels during my doctoral studies. I would also like to thank Robert Schmidt for his priceless help and advice in both scientific and practical issues. He has always been available to patiently answer the many (MANY) questions I have had during these years. I am also grateful to Atsunori Yonehara and Dominique Sluse for interesting discussions and opinions, Marta Zub, Janine Fohlmeister, Arnaud Cassan, Christine Liebig, Nick Bate, Jonathan Duke, Gabriele Maier and Fabian Zimmer for the conversations, drinks, and, most importantly, laughs.

Besides collaborating with people inside ARI, I have had the opportunity to collaborate with people outside the institute. Many thanks go to them, specially: Jean-Paul Kneib, Danielle Alloin, Eric Jullo and Giovanni Covone for their help, comments and suggestions.

Dominique Sluse, Cécile Faure, Janine Fohlmeister, Paola Caprile, Robert Schmidt and Gabriele Maier have been very helpful in providing fast comments, corrections and suggestions to this manuscript (and even the abstract translation!). For that, I am very thankful.

My holidays, weekends, special events and everyday life situations in Germany were generally shared with my friends: Manuel Aravena, Paula Jofré and Matías Carrasco, to whom I am also very grateful. They have played an important role during this period of my life.

Even though physically far, my family (both blood-related and life-acquired) and old friends have been of vital importance during these years. I am sincerely grateful for their love and support. A special acknowledgement must go to my parents Timoleon Anguita and Maria Isabel Avaria: all of the accomplishments in my life have been possible through the world of possibilities, love and understanding they have constantly provided for the last 28 years.

Last but certainly not least, I would like to thank Paola for being the most ideal companion I could have ever dreamt of. She is the engine pushing me towards my most important goals. I am immensely thankful for our beautiful life together.